Studying Quantum-state Resolved Molecule Surface Collisions

Alexander Burden

Submitted to Swansea University in fulfilment of the requirements for the Degree of Master of Science by Research in Chemistry

Swansea University

2023

Abstract

The interaction between molecular hydrogen and a surface is of vital importance to many areas of scientific research. Thus, understanding this interaction and being able to model it is very beneficial. The goal of this master's thesis is to characterise the interaction of hydrogen scattering from a hydrogen passivated chromium(110) surface. The thesis will describe the surface scattering measurements as well as the techniques previously developed to allow for these measurements. The quantum mechanical state of the molecular hydrogen is coherently controlled both before and after the scattering with the surface to theoretically allow for extraction of the scattering matrix from this data, which completely describes the interaction. Scattering both under specular and diffraction channel conditions were described, with the scattering at specular conditions demonstrating that the surface appears as a mirror to the hydrogen under these conditions. However, due to the noise encountered when measuring the signal when scattered into the (0,1) diffraction channel, the results for the scattering matrix for this this measurement are not entirely conclusive. This thesis will demonstrate that the measured signals are still able to provide a benchmark for theoreticians modelling the interaction. We then explore the various possible results for the scattering matrix and the conclusions we can draw from these, such as the high probability that hydrogen molecules rotating as helicopters relative to the surface ($m_J = \pm 1$) are more likely to scatter into the (0,1) diffraction channel than those rotating as cartwheels ($m_J = 0$). A possible resolution to these variety of results is just examining the best fit result to the experimental data; this thesis will describe this result and also explore the extent to which this result can be regarded over other possible solutions. Finally various data treatment options such as frequency filtering will be investigated in attempt to clarify the results from our experimental data.

Acknowledgements

First, I would like to thank my supervisors Prof. Gil Alexandrowicz and Dr. Helen Chadwick for their continual guidance, teaching and above all patience throughout my MSc. Furthermore, I would like to thank all those in the Surface Science group during my time here, Tom, Paul, Morgan, Aisling and Dagmar for their support, discussion and levity making my time at Swansea University much more enjoyable.

The research work was funded by an ERC consolidator grant (Horizon 2020 Research and Innovation Programme grant 772228)

Declarations

This work has not previously been accepted in substance for any degree and is not being concurrently submitted in candidature for any degree.

Signed..[redacted]..

Date...19/05/23..

This thesis is the result of my own investigations, except where otherwise stated. Other sources are acknowledged by footnotes giving explicit references. A bibliography is appended.

Signed...[redacted]..

Date...19/05/23..

I hereby give consent for my thesis, if accepted, to be available for electronic sharing

Signed..[redacted]..

Date...19/05/23..

The University’s ethical procedures have been followed and, where appropriate, that ethical approval has been granted.

Signed...[redacted]..

Date...19/05/23..

Contents

1. Introduction and Background

The gas surface interaction is of vital importance for a wide variety of topic in chemistry, from atmospheric chemistry[1] to catalysis[2]. Thus, accurately modelling these interactions to gain a predictive understanding can offer valuable insights. However, there exists a large degree of difficulty in modelling surface interactions with even the simplest molecule, H_2[3]. Modelling these systems involves modelling of the molecule and surface degrees of freedom, which introduces a high degree of complexity. Therefore, approximations must be made using some technique, often density functional theory (DFT) in combination with other approximations such as the Born-Oppenheimer approximation. In order to test the validity and accuracy of these approximations, benchmarks from experimental surface science studies can be crucial in developing accurate models. The most stringent of these benchmarks have been provided by quantum-state controlled and resolved gas molecule-surface experiments, where the effect of the different internal degrees of freedom of the molecules on the interaction can be observed[4-7]. An even more stringent test for theoretical calculations can be provided by the coherent control of the quantum state of the molecule before and after interacting with the surface. This was previously demonstrated by Alkoby et al[8], using a magnetic molecular interferometer (MMI), which is the same apparatus that will be used in this study. These state-to-state measurements, following the coherent propagation of the nuclear spin and rotational angular momentum projection states, allow for the experimental determination of the scattering matrix, which characterise how the wavefunction of the molecules changes when they scatter from the surface. In this study these same state-to-state measurement capabilities will be leveraged to investigate the effect of the molecular rotation orientation as well as the orientation of the nuclear spin when scattering H_2 molecules from a hydrogen covered chromium(110) surface (H-Cr(110)).

1.1. Stereodynamic Gas Surface Studies

One of the most commonly controlled molecular degrees of freedom is the alignment of the rotational angular momentum, $\boldsymbol{J}$, i.e., how much the molecule has a preferred plane of rotation. The effect of this rotational alignment in gas molecule-surface interactions is often investigated in one of two ways, molecular beam experiments involving careful preparation of the quantum state of the molecule before the interaction or precise measurement of the state after desorbing from a surface. Examining the first case, in general quantum state preparation techniques fall into one of two categories[9]:

1. Photo-excitation schemes using narrow bandwidth light to alter the quantum sate populations by selective excitation of an internal quantum state.
2. Electrostatic filtering of molecules with electric/magnetic dipole moments using inhomogeneous fields which will exert state-dependent forces, deflecting desired/undesired states.

Yoder et al. [10] employed linearly polarised infrared radiation to prepare CD_3H in a single excited rovibrational state, where the rotational angular momentum and vibrational transition dipole moment would be aligned parallel to the polarisation of the radiation by aligning the C−H bond. By depositing methane with a molecular beam on Ni(100) in two different experiments, once with the polarisation parallel and the other with it perpendicular to the surface, they found an increase in reactivity when the laser polarisation was aligned parallel to the surface which was determined by measuring the amount of carbon on the surface.

A novel technique developed by Schäfer et al.[11] irradiates molecules with a high resolution laser in a region free of electric fields. The molecules are excited selectively into one of two states with zero-field splitting. They then pass through a static electric field within which the two states mix leading to the molecule adiabatically evolving into a bond−oriented state within the field. This technique was used to orient NO molecules before scattering with an Au(111) surface[12], leading to either an N-end or O-end collision. The rovibrational states populated by the collision are measured by resonance-enhanced multiphoton ionisation (REMPI) spectroscopy. From this, enhanced vibrational relaxation is observed for N-atom first collisions.

Kurahashi et al.[13] used a hexapole lens to select a single O_2 spin rotational state, $(J, m_J) = (2,2)$, where J is the rotational angular momentum quantum number, and m_J is the projection of J on a specified axis, by taking advantage of the paramagnetic properties of O_2. A spin orienting and molecular aligning field followed the hexapole lens, as the spins would align with the field with the molecular axis preferentially perpendicular to the field. By changing the direction of this orienting field with respect to the surface, the sticking probability of O_2 on a magnetised Ni(111) surface was observed to be higher for molecules rotating as helicopters relative to the surface, implying a preference for side-on collisions. The same technique was applied further by the group to study O_2 adsorption on Si(100) and Al(111) surfaces[14], where they again found that molecules rotating like helicopters are more likely to stick than cartwheels. The technique was also extended to a scattering experiment[15]. The alignment of O_2 molecules before scattering from highly oriented pyrolytic graphite and LiF(001) surfaces was demonstrated to impact the angular distribution of the scattered molecules as well as the trapping probability and energy dissipation efficiency. Further examples of state selection experiments can be found in the reviews [7, 9, 16] and the references within.

Recombinative desorption studies observe the state of a molecule after desorbing from a surface, and then use the principle of detailed balance to argue that observed preferences in alignment must also apply when adsorbing to the surface. One example of such an experiment is that performed by Hou et al.[17] where the recombinative desorption of D_2 on Cu(111) was studied. Here one side of a thin Cu single crystal was exposed to D_2, which adsorbed to it before the D atoms diffused through the crystal to the other side. The D atoms would then undergo recombinative desorption and enter the gas phase as

D_2 molecules. A REMPI scheme was used with linearly polarised light to ionise a specific rovibrational state with the molecular bond axis parallel to the electric field component of the light. By changing the polarisation of the light between parallel and perpendicular to the surface in combination with time-of-flight measurements, the degree of alignment of the D_2 as a function of velocity was found. When relating this to the adsorption of D_2 onto the surface, they determined that there is a strong preference for broad side (helicopter) over end-on (cartwheel) collisions in the dissociative adsorption. Further recombinative desorption studies can be found in references[18, 19] and in the review article[20].

1.2. Hydrogen Scattering Studies

Rotational projection state-to-state hydrogen scattering measurements have not been performed outside of those using the same experimental apparatus as will be employed for this study[8, 21, 22], however hydrogen scattering studies have previously been used to characterise the hydrogen-surface interaction[23, 24]. In molecular beam studies of the interaction between molecular hydrogen and a surface, provided the temperature is high enough to neglect physisorption, there are two pathways available to the molecule. The hydrogen molecule can either undergo dissociative chemisorption or scatter back into the gas phase. When scattering back into the gas phase they can diffractively scatter, and, given the energies involved in these studies, the diffraction can be elastic or involve rotational transitions, called rotationally inelastic diffraction (RID). As will be explained in section 2.5, the locations of the elastic diffraction channels will be given by Bragg's law, and then the locations of the RID channels will be given by using Bragg's law in combination with the conservation of energy. The probability of scattering into a given diffraction channel, whether elastic or rotationally inelastic, will be characteristic of the potential energy surface (PES) of the system. Thus studies measuring the intensity of the scattering of different diffraction channels at different energies can offer tests for theoretically calculated PESs[24].

The first of the studies to calculate theoretical scattering intensities was performed by Gross and Scheffler[25]. They calculated the intensity of different elastic and RID channels of H_2 scattering from Pd(100) and their dependence on molecule incident energy. This was achieved through six-dimensional quantum dynamics calculations using a PES calculated from DFT. They predicted significant out-of-plane and RID scattering intensities that had not been observed experimentally before then. These out-of-plane scattering intensities were also predicted for H_2 scattering from Pt(111)[26, 27]. Experimentally this was observed later in scattering of H_2 from Pt(111) and Pd(111)[28, 29]. However, calculated PESs do not always describe the experiment as closely as in the above studies. For example, PESs for H_2 scattering from Ru(0001) using two different functionals were unable to match experiments over the whole incident energy range[30].

The study described in this thesis will study hydrogen scattering from a chromium surface. Instead of comparing the relative intensity of different diffraction peaks, we will focus on two scattering channels, specular scattering and scattering into the (0,1) diffraction peak. For each of these channels the scattering intensity will be measured using the MMI technique, which will be explained in chapter 2, giving rise to an interference pattern which will then be analysed. The measured interference pattern is related to the scattering matrix, a concept which will explained in more detail in the next chapter which expresses the probability of different rotational and nuclear spin projection states scattering into the channel of interest as well as the changes in phase of the molecular superposition quantum state. Extracting the scattering matrix provides a more stringent test of theoretical calculations than comparing relative changes in the intensities of the diffraction peaks, which are insensitive to the phases of the scattering matrix, as it is much more difficult to achieve fortuitous agreement of calculated and measured interference signals.

1.3. Nuclear Spin Conversion and Flips in Hydrogen

The conversion of ortho- to parahydrogen is an important area of research technologically relevant to storing of hydrogen as a fuel source[31]. Liquid hydrogen provides a high-density storage method for this efficient fuel source. The nuclear spin conversion (NSC) of ortho- to parahydrogen involves both a change of rotational and nuclear spin state. Therefore, 40% of the stored liquid hydrogen can be lost to evaporation within 100 hours due the conversion of ortho- to parahydrogen releasing energy due to rotational state relaxation[32]. Hence, it can prove to be beneficial to increase the amount of parahydrogen before liquefication. This NSC process is very slow under normal conditions, but can be promoted through collision with a solid surface[33]. For NSC in hydrogen, the change in nuclear spin state is necessarily accompanied by a change of rotational state, and therefore studies typically detect the different nuclear spin states through rotational spectroscopy of molecules adsorbed to surfaces, for example using electron energy loss spectroscopy[34-36] or desorbing hydrogen molecules and then detecting them with REMPI schemes[37-39]. Our study, contrastingly, will allow for the investigation of the nuclear spin projection state, to see if this change can occur in single collisions, while keeping the rotational state constant. This could provide useful context for NSC studies. Moreover, theoretically, a rotational orientational preference has been proposed for ortho- to para-hydrogen conversion[40] however no experiments have been performed to validate this. By finding the scattering matrix, we would be able to validate if these proposed rotational orientational preferences also exist for changes in nuclear spin projection state.

1.4. Previous Studies with the Magnetic Molecular Interferometer setup

The restriction with some of the stereodynamic measurements explored above is that they rely on paramagnetic molecules, such as O_2, for magnetic manipulation or excited molecules where very specific excitation schemes can be used to perform stereodynamic control. Moreover, there is often quick mixing between the internal states of the molecules[41, 42], meaning they are limited as to which molecule-surface interactions can be studied, unless this mixing is controlled and accounted for as in this study.

The MMI experimental setup we will use provides a more general approach by allowing the alignment manipulation of a variety of ground-state molecules, including closed-shell molecules[43]. Moreover, as will be explained in section 2.2.3, due to the coherent propagation of the molecule throughout the apparatus the effect of mixing is known and incorporated into the propagation and analysis. The specifics of the setup will be explored in the following chapter, but generally the MMI is a modified He-spin-echo spectrometer[44] using magnetic manipulation of the rotational and nuclear spin magnetic moments to control and resolve the rotational orientation and nuclear spin projection states of molecules.

With this setup, the rotationally inelastic scattering of D_2 from Cu(111) has been studied[22] as well as the elastic scattering of H_2 from LiF(100)[8] in order to experimentally determine the scattering matrix. This latter study provided a stringent benchmark for theoreticians and discovered a dependency of the molecule-surface interaction on the rotational orientation of the molecule before the collision, while also revealing high probabilities of flipping this orientation during the scattering event. It was assumed that no change in the orientation of the nuclear spins upon interaction occurred as the surface is non-magnetic. Scattering matrices obtained when fitting to the experimental data under this assumption offered good agreement with the experiment. The study reported in this thesis will also provide insight into the validity of this assumption, by examining if using an antiferromagnetic surface, chromium, instead of a non-magnetic surfaces, copper and lithium fluoride, will result in a different observation to the change in orientation of the nuclear spin of hydrogen.

1.5. Thesis Outline

Section 2 will detail the various components of the experimental apparatus and explore the theoretical background to understand the role of the individual components, how they are used in concert to give us our experimental signal and how the signal can be used to find the scattering matrix of the molecule-surface interaction. Section 3 outlines the experimental procedures involved in preparing and aligning the surface to be able to complete our measurements. The experimental parameters for these measurements will then be given. Section 4 will present the results given by the measurements, different data treatments employed, the conclusions we are able to draw and the reliability of these conclusions. Finally, the last chapter will provide a summary as well as an outlook for future experiments.

2. Principles of the Experiment

2.1. Ground State Hydrogen

A hydrogen molecule consists of two hydrogen atoms covalently bonded together. Hydrogen atoms possess a spin-½ nuclear spin, and therefore when looking at a hydrogen molecule these nuclear spins can either be parallel (orthohydrogen, total spin I=1) or anti-parallel (parahydrogen, total spin I=0). When looking at the molecular wavefunction (ψ) of the hydrogen molecule, under the Born-Oppenheimer approximation, it can be split into a product of different component wavefunctions:

$$\psi = \psi_{elec}\psi_{vib}\psi_{rot}\psi_{nuc} \tag{2.1}$$

Under the Pauli exclusion principle, the total molecular wavefunction must be antisymmetric with respect to the exchange of fermions. The ground state electronic (ψ_{elec}) and vibrational (ψ_{vib}) wavefunctions are symmetric with respect to the exchange of the protons, and for orthohydrogen the nuclear wavefunction (ψ_{nuc}) is symmetric with respect to this exchange. Therefore, the rotational wavefunction must be antisymmetric, meaning the rotational quantum number (J) must be odd and correspondingly $J = 1$ for the rotational ground state of orthohydrogen. Conversely, the nuclear wavefunction is antisymmetric for parahydrogen leading to even values of J and a ground state of $J = 0$. Since ground state parahydrogen possesses no rotational angular momentum and its total nuclear spin (I) is zero, it does not have a magnetic moment. Therefore, parahydrogen cannot be magnetically manipulated and will thus form a constant background for our experiment. On the other hand, the ground state of orthohydrogen possesses rotational angular momentum $J = 1$ and total nuclear spin $I = 1$, so can be magnetically manipulated in our experiment and will be the focus of this study.

With a total nuclear spin of 1, orthohydrogen has three nuclear spin projection states onto a given quantisation axis, $m_I = 0, \pm 1$. Likewise, with rotational quantum number $J = 1$, this gives rise to three rotational projections $m_J = 0, \pm 1$ onto a quantisation axis. Examining the case where we select our quantisation axis to be along the surface normal, we describe $m_J = 0$ as rotating as a cartwheel and we describe $m_J = \pm 1$ as rotating as a clockwise/anti-clockwise helicopter when approaching the surface.

2.2. The Magnetic Molecular Interferometer Apparatus

A schematic overview of the Magnetic Molecular Interferometer (MMI) apparatus can be seen in Figure 2.1. The first component of the machine is the atomic/molecular beam source which produces a collimated beam of, in this study hydrogen, molecules. The beam then passes through a permanent hexapole magnetic field which acts as a magnetic lens to focus/defocus different m_I, m_J states, depending on their magnetic moment. At the end of the hexapole there is a hexapole-dipole transition element. This transition element adiabatically rotates the magnetic moments from the various magnetic field orientations in a hexapole field toward a single quantisation axis in the laboratory frame, which will be defined as the Z direction. Following this transition, the next component of the machine is the first solenoid, which produces a field aligned in the $-X$ direction, when using a positive current, which is employed to coherently manipulate the state of the hydrogen molecules as they travel through the field. The hydrogen molecules then enter the scattering chamber, interacting with the surface and scatter into a multitude of different directions. The surface can be aligned so that one of the diffraction channels points towards the second arm of the beam line, where this is controlled by a 6-axis manipulator upon which the surface is mounted. The temperature of the surface is controlled through the combination of radiative heating from a filament and cooling from a closed-cycle liquid Helium system and monitored using a T-type thermocouple spotwelded to the sample holder. Initial sample preparation and characterisation was performed as detailed in chapter 3, using a leak valve to cover the surface in hydrogen, an argon ion sputter gun to clean the surface and a low-energy electron diffraction (LEED) instrument to characterise the surface structure, all of which are attached to the ultrahigh vacuum scattering chamber.

The second arm follows the same design sequence as the first but in reverse order – consisting of a second solenoid B_2 followed by a dipole-hexapole transmission element oriented along the Z' axis before a second hexapole. At the end of the beam path is an ultra-high efficiency particle detector which functions as a very sensitive mass spectrometer[45].

Both solenoids in the machine are tuneable electromagnets controlled by high stability power supplies to produce the desired magnetic field. The MMI beam line is enclosed by multiple layers of μ-metal shielding so that any magnetic fields originating from outside of the machine are reduced to negligible levels.

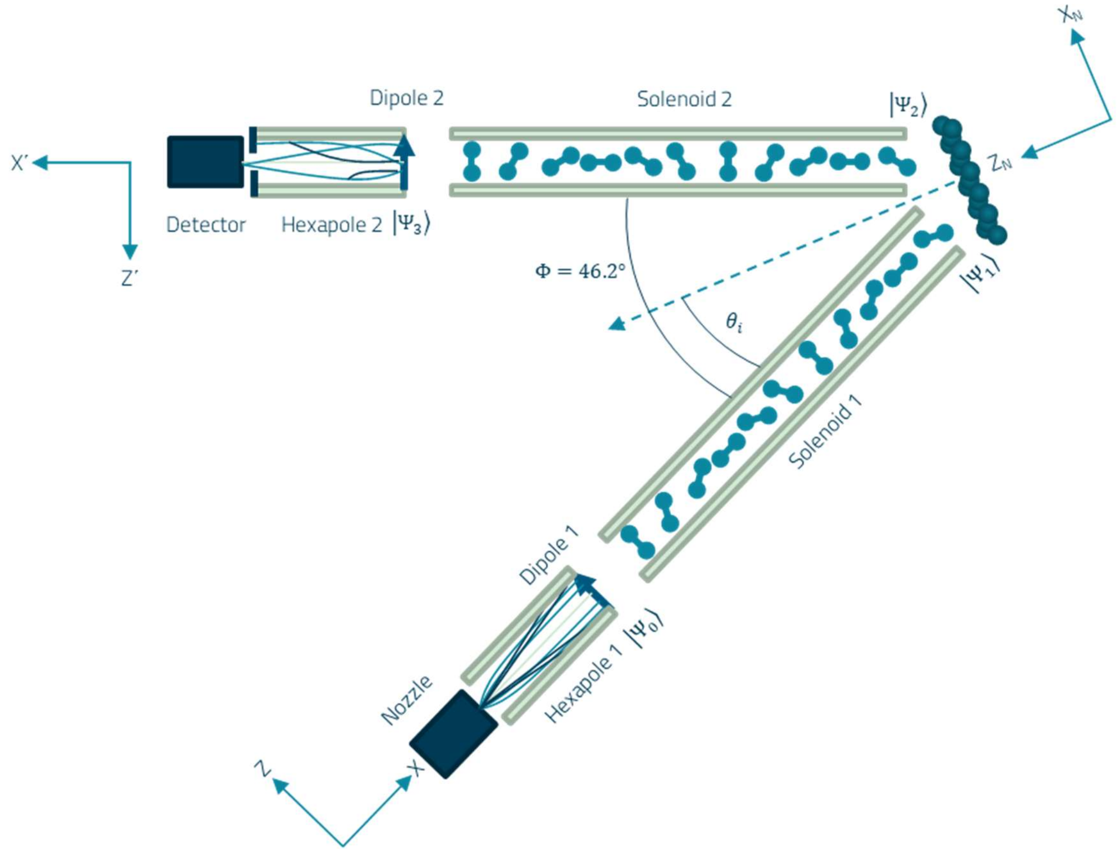

Figure 2.1: Set up schematic with various components labelled. The state vector of a hydrogen molecule at various points in propagation through the machine is noted by subscript notation for future reference in section 2.3 where the propagation is further explained. Φ *here is total angle and* θ_i *is the incidence angle further explained in section 2.4.*

The following subsections will describe in more detail the principles and processes behind some of these components.

2.2.1. Atomic and Molecular Beams

The first component of the apparatus forms the molecular beam of hydrogen which will eventually interact with the surface. The beam is created through a supersonic expansion through a nozzle held at 100K using a closed-cycle helium cryocooler. The centre of the beam is then selected by a skimmer placed after the nozzle. Assuming an ideal supersonic expansion, and neglecting significant population in excited rotational states, i.e. treating the beam as an atomic beam, the H_2 molecules should have a kinetic energy given by[46]:

$$\frac{1}{2}mv^2 = \frac{5}{2}k_B T \,, \tag{2.2}$$

where m is the mass of the molecule, v is its velocity, k_B is the Boltzmann constant and T is the nozzle temperature. More realistically, in the case of hydrogen, the velocity of the individual molecules composing the beam will be distributed around this central velocity as given in the equation above with a non-zero distribution width. For simplicity we will assume a gaussian shape for the distribution function. In this study a nozzle temperature of 100K was used giving a mean velocity of 1442ms^{-1} with a full width half maximum of about 5% this velocity. This beam will contain mixture of ortho and parahydrogen, in a 3:1 ratio, both in their rotational ground states.

2.2.2. State Selection

After exiting the skimmer as a collimated beam, and passing through two differential pumping stages, the beam then enters a hexapole magnet. The combination of three nuclear spin projection states and three rotational angular momentum projection states leads to nine pure $|m_I, m_J\rangle$ states in which the rotational ground state orthohydrogen can exist. The beam enters the hexapole as an equal population in each of these nine states. The force experienced by a magnetic dipole in a hexapole field is given by[47]:

$$\boldsymbol{F} = \pm\mu\nabla|\boldsymbol{B}_{HEX}|\,, \tag{2.3}$$

with the hexapole field given by[47]:

$$\boldsymbol{B}_{HEX} = 3C_3\big(cos(3\theta)\hat{\boldsymbol{r}} + sin(3\theta)\hat{\boldsymbol{\theta}}\big) \tag{2.4}$$

Therefore, the molecules will experience a simple harmonic restoring or deflecting force leading to focussing or defocussing depending on the molecule's m_I, m_J state. The effect of m_J on the overall magnetic moment is relatively small with respect to that of m_I[48]. Consequently, in the case of orthohydrogen, $m_I = +1$ molecules will be defocussed, whilst $m_I = -1$ will be focussed, leaving $m_I = 0$ less affected by the field, as the deflection is due to the weaker rotational magnetic moment. After exiting the hexapole the probability of a molecule being in one of the nine states has now shifted from an equal to an unequal distribution. However, the quantisation axis defining the state selection of the individual molecules is dependent on the path they took through the hexapole, meaning they are not oriented with respect to a common direction. Therefore, after the hexapole there is a hexapole-dipole field transmission element. This changes the direction of the magnetic field which the spins of the molecules follow adiabatically to rotate their quantisation axis as defined by the hexapole to a common direction, defined by the direction of the dipole, Z. Following this the beam now contains an unequal distribution of the nine pure states quantised in the laboratory Z frame. The state-dependent transfer probabilities after passing through the hexapole lens can be calculated using an adapted semi-classical trajectory code from previous calculations of water and methane molecules focussing in a hexapole magnetic field[49].

2.2.3. Coherent Magnetic Manipulation

To build an image of how we manipulate the state of a hydrogen molecule we can first start from a classical description of the dynamics of a single magnetic moment. If we apply a magnetic field with a constant strength, B, for a time, t, to a magnetic moment which is not initially pointing along the same direction of the magnetic field,, it will precess within the plane perpendicular to the field direction, and the phase within that plane, ϕ, will be given by[50]:

$$\phi = \gamma B t \tag{2.5}$$

where γ is the gyromagnetic ratio. We are considering the molecules to have only a single gyromagnetic ratio, neglecting the more complex nature of the Hamiltonian of H_2 for now. In our case, however, rather than a static magnetic moment with a field applied to it, we have a magnetic moment travelling through a magnetic field, which are the fields generated by the solenoid. If the field is aligned along the same direction throughout the field region and the rate of change of the field at the boundaries of the field region are much larger than the local Larmor frequencies, then we can say that the total precession phase is:

$$\phi = \gamma \int_{t_1}^{t_2} B(t) dt \tag{2.6}$$

where t_1 and t_2 are the times when the magnetic moment enters and exits the field region, respectively. The time spent in the field is also dependent on the velocity of the magnetic moment. Thus, we can rewrite equation 2.6 for a magnetic moment travelling at a single constant velocity, v, along the x axis:

$$\phi = \frac{\gamma}{v} \int_{x_1}^{x_2} B(x) dx \tag{2.7}$$

where x_1 and x_2 are the locations where the magnetic moment enters and exits the field region, respectively. In our experiments the magnetic field used to cause this precession is generated by solenoids, and the strength of magnetic field generated is linearly proportional to the current in the solenoid. Therefore, if we assume that all magnetic moments pass through the same field integral, it is convenient to define a constant effective field, B_{eff}, which describes the relationship between field integral and current:

$$B_{eff} = \int_{x_1}^{x_2} \frac{B(x)}{I} dx \tag{2.8}$$

We can then rewrite equation 2.7 as:

$$\phi = \frac{\gamma}{v} B_{eff} I \tag{2.9}$$

The projection of a magnetic moment onto a defined axis will be a function of the amount it has precessed, and therefore a function of the current passed through the solenoid. This is analogous to the signal we measure, so defining signal as a function of current:

$$signal(I) = \cos\left(\frac{\gamma}{v} B_{eff} I\right) \tag{2.10}$$

In our case the molecules comprising our beam cannot be represented as a single classical magnetic moment precessing in a magnetic field, as is the case for helium-3 atoms. For a (closed-shell) homonuclear diatomic molecule in a magnetic field this can be described by the Ramsey Hamiltonian as defined in [48]. For an orthohydrogen molecule in its rotational ground state this becomes:

$$\frac{\widehat{H}_R(B)}{h} = -a\frac{\boldsymbol{I}\cdot\boldsymbol{B}}{B} - b\frac{\boldsymbol{J}\cdot\boldsymbol{B}}{B} - c\,\boldsymbol{I}\cdot\boldsymbol{J} + d\left(3\,(\boldsymbol{I}\cdot\boldsymbol{J})^2 + \frac{3}{2}\,\boldsymbol{I}\cdot\boldsymbol{J} - \boldsymbol{I}^2\boldsymbol{J}^2\right), \tag{2.11}$$

Where $\boldsymbol{I}$ is the nuclear spin vector, $\boldsymbol{J}$ is the rotational angular momentum vector and $\boldsymbol{B}$ is the magnetic field vector. The first two terms a and b are proportional to the magnetic field strength, both being proportional to field strength, describing the interaction of the different magnetic moments with the field. On the other hand, the second two terms c and d are field independent, the first describing the spin-rotation interaction, whilst the second describes the spin-spin interaction between the two nuclei[48]. The values for these terms are given in Table 2.1. This leads to the energy splitting of the nine different states in a magnetic field, as seen in Figure 2.2. We can see that the $m_I = 0, m_J = 0$ state is still affected by the field due to the field independent terms in the Ramsey Hamiltonian.

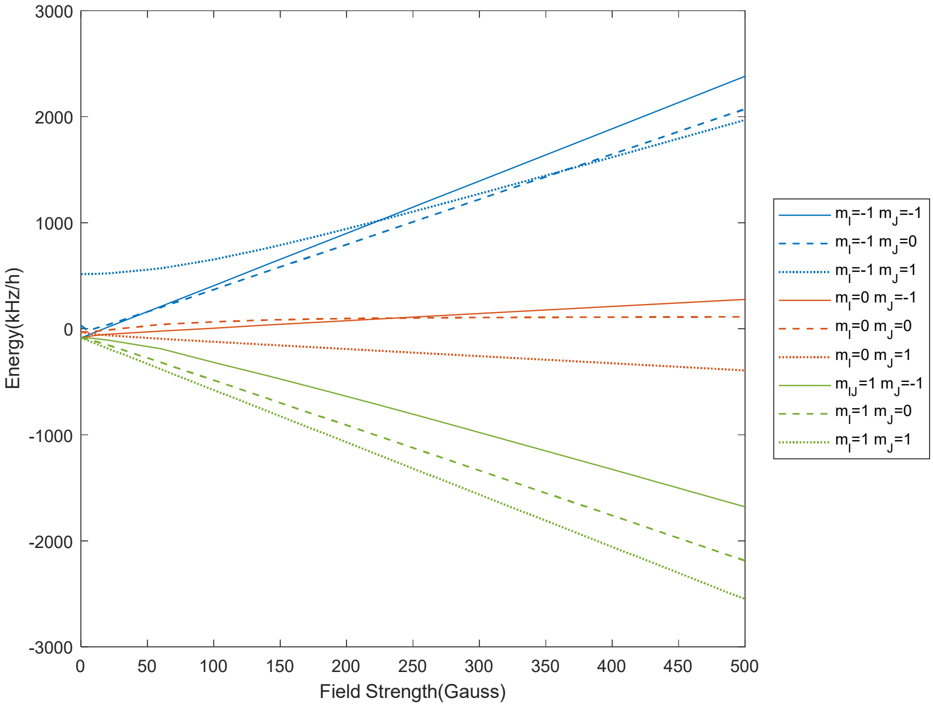

Figure 2.2: Graph showing energy vs magnetic field strength for the 9 states – blue is $m_I = -1$*, orange* $m_I = 0$ *and green* $m_I = 1$*, solid is* $m_J = -1$*, dashed* $m_J = 0$ *and dotted* $m_J = 1$*, using values calculated in [48].*

Term	a (kHz/gauss)	b (kHz/gauss)	c (kHz)	d (kHz)
Value	4.258	0.6717	113.8	57.68

Table 2.1: Values for the terms in equation 2.11 from [48].

Due to the non-linear and mixing terms in the second two components of the Hamiltonian, the calculation of energy levels can be quite complicated. However, under strong fields, such as in the dipole transmission element, we can apply an approximation to the Ramsey Hamiltonian where only the interaction terms with the magnetic field dominate:

$$\frac{\hat{H}_R(B)}{h} = -a\frac{\boldsymbol{I}\cdot\boldsymbol{B}}{B} - b\frac{\boldsymbol{J}\cdot\boldsymbol{B}}{B}, \tag{2.12}$$

Under this approximation we can demonstrate how pure states aligned with the field will be maintained. For example, if we have an initial pure state in the Z basis in a field aligned in the Z direction, our Hamiltonian becomes:

$$\frac{\hat{H}_R(B)}{h} = -am_I - bm_J, \tag{2.13}$$

where m_I and m_J are the projection quantum numbers onto the Z direction. Therefore, the time evolution operator for our hydrogen molecule in the strong field will be, in the quantisation axis of the field:

$$\hat{U}(t,B) = e^{-\frac{i\hat{H}t}{\hbar}} = \sum_{m_I,m_J} \left|m_I,m_J\right\rangle e^{i2\pi a m_I t} e^{i2\pi b m_J t} \left\langle m_I,m_J\right| \tag{2.14}$$

From this we can calculate the probability of finding an initial pure state in one of the nine $\left|m_I,m_J\right\rangle$ states along the field axis in any $\left|m_I,m_J\right\rangle$ state after time t within a strong magnetic field:

$$\begin{aligned} P_{m_I'',m_J'',m_I',m_J'} &= \left|\left\langle \Psi^{final}\middle|\Psi(t)\right\rangle\right|^2 = \left|\left\langle m_I'',m_J''\middle|\hat{U}(t,B)\middle|m_I',m_J'\right\rangle\right|^2 \\ &= \left|\left\langle m_I'',m_J''\right| \textstyle\sum_{m_I,m_J}\left|m_I,m_J\right\rangle e^{i2\pi a m_I t} e^{i2\pi b m_J t}\left\langle m_I,m_J\right| \left|m_I',m_J'\right\rangle\right|^2 \\ &= \left|e^{i2\pi a m_I' t} e^{i2\pi b m_J' t}\delta_{m_I'',m_I'}\delta_{m_J'',m_J'}\right|^2 = \left|\delta_{m_I'',m_I'}\delta_{m_J'',m_J'}\right|^2 \end{aligned} \tag{2.15}$$

Where δ_{ij} is the Kronecker delta. Equation 2.15 demonstrates how an initially pure $\left|m_I,m_J\right\rangle$ state quantised along the field axis will maintain its state along this axis when in a strong field. However, in our system, the field inside the solenoid is not aligned with the quantisation axis Z, but instead along X. Therefore, we must apply a rotation operator corresponding to a $-\pi/2$ rotation around the Y axis to change the basis from Z to X. In the X basis an eigenstate in Z will exist as a superposition state:

$$|\Psi(t=0)\rangle_Z = \left|m_I, m_J\right\rangle_Z = \hat{R}\left(-\frac{\pi}{2}\right)\left|m_I, m_J\right\rangle_X = \sum_{m_I, m_J} A_{m_I, m_J}\left|m_I, m_J\right\rangle_X \tag{2.16}$$

Where A_{m_I,m_J} are complex constants, with:

$$P_{m_I,m_J} = \left|A_{m_I,m_J}\right|^2 \tag{2.17}$$

$$\sum_{m_I,m_J} A_{m_I,m_J} = 1 \tag{2.18}$$

P_{m_I,m_J} gives the probability of measuring the state in $\left|m_I, m_J\right\rangle$ along the X axis. Thus, starting in an initially pure $\left|m_I, m_J\right\rangle_Z$ along the Z axis, the probability of finding the molecule in the same $\left|m_I, m_J\right\rangle_Z$ after time t is given by:

$$\begin{aligned}
P_{m_I,m_J,m_I,m_J} &= \left|\langle\Psi(t=0)|_Z|\Psi(t)\rangle_Z\right|^2 = \left|\langle\Psi(t=0)|_Z\hat{U}_Z(t,B)|\Psi(t=0)\rangle_Z\right|^2 \\
&= \left|\langle\Psi(t=0)|_Z\hat{R}^\dagger\left(\frac{\pi}{2}\right)\hat{U}_X(t,B)\hat{R}\left(\frac{\pi}{2}\right)|\Psi(t=0)\rangle_Z\right|^2 \\
&= \left|\sum_{m_I'',m_J'',m_I',m_J',m_I,m_J} A^*_{m_I'',m_J''}A_{m_I',m_J'}\left\langle m_I'', m_J''\right|_X\left|m_I, m_J\right\rangle_X e^{i2\pi a m_I t}e^{i2\pi b m_J t}\left\langle m_I, m_J\right|_X\left|m_I', m_J'\right\rangle_X\right|^2 \\
&= \left|\sum_{m_I,m_J}\left|A_{m_I,m_J}\right|^2 e^{i2\pi a m_I t}e^{i2\pi b m_J t}\right|^2 \\
&= \left|\sum_{m_I,m_J}\left|A_{m_I,m_J}\right|^2\left(\cos(2\pi a' m_I B t) + i\sin(2\pi a' m_I B t)\right)\left(\cos\left(2\pi b' m_J B t\right) + i\sin\left(2\pi b' m_J B t\right)\right)\right|^2
\end{aligned} \tag{2.19}$$

Where $a' = a/B$ and $b' = b/B$. As can be seen from the form of equation 2.19 the probability of finding the molecule in the same $\left|m_I, m_J\right\rangle_Z$ along the Z axis will oscillate in time. For hydrogen in the high field limit, this oscillation will be a combination of eight different frequencies corresponding to the nine possible combinations of $e^{i2\pi(am_I+bm_J)t}$, however $m_I = 0$, $m_J = 0$ will not oscillate, weighted by the initial superposition of the state along the X axis. The probability of finding the molecule in any of the other $\left|m_I, m_J\right\rangle_Z$ states will also oscillate as the molecule undergoes Rabi oscillations between the nine states.

However, the example worked through above is different from our measurement in two significant ways. The first is that the field employed is not a strong field, and as such the strong field approximation cannot be applied. Therefore, the various nuclear spin and rotational angular momentum field-independent coupling terms will be non-negligible, meaning that m_I and m_J will not be eigenstates of the system. This means that for any given field, the evolution matrix must be diagonalised and a similarity transform is required between the m_I, m_J basis and the eigenbasis. The second difference is that as the hydrogen molecule travels through the machine, it does not experience the idealised magnetic field profile considered above, i.e., a dipole field along Z and then a solenoid field along X. Instead, the field profile has additional components, including small residual fields. These residual fields have been characterised for the entire machine, starting from when the field from the first dipole becomes weak enough for states to start mixing, and ending at the equivalent point in the second arm. The residual field can also act in X, Y and Z, further emphasising the previous point for the requirement of diagonalisation and the use of similarity transformations.

This all affects how the propagation of the hydrogen through the machine is modelled. In our modelling this is treated semi-classically, although a fully quantum description gives the same results for fields of $< 10^4$ gauss metre[51]. This means we treat the movement of the molecule classically, and then the state of the molecule quantum mechanically under the Ramsey Hamiltonian using equation 2.12. This is achieved for an individual arm by splitting the length from where the strong field assumption ceases to hold until the position of the surface in the scattering chamber into sections of varying lengths. The number of sections in any given length of the machine depends on how much the field changes as a function of distance, with larger changes requiring a higher number of smaller sections. Time evolution operators for each of these sections can be calculated analytically. The average field is calculated in three dimensions using the field, residual plus solenoid field if it is there, at the start and end of a given section, giving $\boldsymbol{B}$. The time spent in the field, t, is calculated using the length of the section and the speed of the hydrogen molecule. Replacing time with displacement from the end of the transmission element field, x, and velocity, v, under:

$$t = \frac{x}{v}$$

the unitary evolution operator for a given section is then:

$$\hat{U}(t_1, t_2, \boldsymbol{B}) = \hat{U}(x_1, x_2, v, \boldsymbol{B}) = \hat{R}^{\dagger}(\theta)\hat{M}^{-1}(\boldsymbol{B})\hat{D}(x_1, x_2, v, \boldsymbol{B})\hat{M}(\boldsymbol{B})\hat{R}(\theta) \tag{2.20}$$

where θ is the angle between $\boldsymbol{B}$ and Z in the first arm and Z′ in the second arm. Practically this is achieved by a rotation around Z into the XZ plane and then a rotation around Y into the Z direction. The diagonal matrix is:

$$\hat{D}(x_1, x_2, v, \boldsymbol{B}) = \sum_{m_I, m_J} |m_I, m_J\rangle e^{iE_n \frac{x_1 - x_2}{v}} \langle m_I, m_J| \tag{2.21}$$

And $\hat{M}(\boldsymbol{B})$ is a matrix of eigenvectors $\boldsymbol{\mu}_n$ corresponding to the above eigenenergies E_n as a solution to the eigenvalue equation:

$$\hat{H}_R(\boldsymbol{B}) \cdot \boldsymbol{\mu}_n = E_n \boldsymbol{\mu}_n \tag{2.22}$$

Therefore, if an individual arm is split into a sections, the overall evolution operator for propagation through this arm of the machine will be:

$$\hat{U}(x_l, v) = \hat{U}(x_{a-1}, x_a, v, \boldsymbol{B})\hat{U}(x_{a-2}, x_{a-1}, v, \boldsymbol{B}) \cdots \hat{U}(x_1, x_2, v, \boldsymbol{B})\hat{U}(0, x_1, v, \boldsymbol{B}) \tag{2.23}$$

2.3. Scattering and Signal Calculation

The signal received at the detector for any given field first and second solenoid field values, B1 and B2 respectively, can be described as a weighted sum across all the velocities in the velocity distribution of the probabilities of a hydrogen molecule being found at the detector in one of the nine m_I, m_J states, given an initial m_I, m_J state, summed across all initial and final states. The explanation of the signal below will follow that outlined by Alkoby et al. [8]. For clarity the different state vectors have been labelled on Figure 2.1. The signal can be written much more concisely as:

$$Signal = \sum_{\mathrm{v}} P_{\mathrm{v}} \sum_{f=1}^{9} \sum_{n=1}^{9} \langle \psi_{f,n} | \psi_{f,n} \rangle \tag{2.24}$$

where v is velocity and n and f are integers representing one of the nine pure states $|m_I, m_J\rangle = |n\rangle$. $|\psi_{f,n}\rangle$ can be calculated by propagating a hydrogen molecule through the whole system – from the end of the strong field of the dipole transition element after the first hexapole to the start of the strong field of the dipole transition element before the second solenoid. The state vector for a given velocity and initial state at the beginning of our propagation, at the end of the first dipole is:

$$|\psi_{0n}^{Z}\rangle = \sqrt{p_{hex1}(n)}|n\rangle \tag{2.25}$$

Here $p_{hex1}(n)$ is the probability of state $|n\rangle$ passing through the hexapole, given the m_I and m_J values of the state. These probabilities have been calculated for each of the nine m_I, m_J states. As described above a unitary evolution matrix describing the evolution of a hydrogen molecule through the first arm of the machine can be calculated for a given field strength B1, $\hat{U}(B1)$, meaning the state vector at the end of the first arm immediately before the surface becomes:

$$|\psi_{1n}^{Z}\rangle = \hat{U}(B1)\sqrt{p_{hex1}(n)}|n\rangle \tag{2.26}$$

The interaction of the hydrogen molecule with the H-Cr(110) is characterised by the scattering matrix $\hat{S}$. In this study $\hat{S}$ is a 9-by-9 matrix with matrix elements:

$$S_{fn} = \langle f|\hat{S}|n\rangle \tag{2.27}$$

The scattering matrix describes the evolution of a molecule when it interacts with a surface, i.e., the change in magnitude and phase of the components of the molecular quantum state. However, the quantisation axes of scattering matrices are conventionally taken as the surface normal[52], therefore before applying the scattering matrix operator, we must rotate the state vector so that it is quantised along the surface normal, labelled Z_N in Figure 2.1:

$$\left|\psi_{1n}^{Z_N}\right\rangle = \hat{R}(\theta_1)\left|\psi_{1n}^{Z}\right\rangle = \hat{R}(\theta_1)\hat{U}(B1)\sqrt{p_{hex1}(n)}|n\rangle \tag{2.28}$$

where θ_1 is the angle between the laboratory first arm Z axis and the surface normal, given by $90 - \theta_i$, where θ_i is the incidence angle as shown in Figure 2.1. From this the state after interaction with the surface is simply given by applying the scattering matrix:

$$\left|\psi_{2n}^{Z_N}\right\rangle = \hat{S}\left|\psi_{1n}^{Z_N}\right\rangle = \hat{S}\hat{R}(\theta_1)\hat{U}(B1)\sqrt{p_{hex}\ (n)}|n\rangle \tag{2.29}$$

As for before the surface, to propagate the beam down the second arm, the quantisation axes must be rotated to the quantisation axis of the second arm, Z':

$$\left|\psi_{2n}^{Z'}\right\rangle = \hat{R}(\theta_2)\left|\psi_{2n}^{Z_N}\right\rangle = \hat{R}(\theta_2)\hat{S}\hat{R}(\theta_1)\hat{U}(B1)\sqrt{p_{hex}\ (n)}|n\rangle \tag{2.30}$$

Where θ_2 is the angle between the Z' in the second arm and the surface normal, which would be given by $90 - (\Phi - \theta_i)$, where Φ is the total angle between the two arms of the machine, as shown labelled in Figure 2.1. Then, with the same method as before, an evolution operator representing the effect of moving through the second solenoid field, $\hat{U}(B2)$, can be calculated and applied to give the state of the beam after the solenoid:

$$\left|\psi_{2n}^{Z'}\right\rangle = \hat{U}(B2)\left|\psi_{2n}^{Z_N}\right\rangle = \hat{U}(B2)\hat{R}(\theta_2)\hat{S}\hat{R}(\theta_1)\hat{U}(B1)\sqrt{p_{hex}\ (n)}|n\rangle \tag{2.31}$$

Finally, once again each of the nine states has a known probability for making it through the hexapole, calculated using semi-classical trajectory modelling. Therefore, for a given final state, $|f\rangle$, the state vector becomes:

$$\left|\psi_{fn}^{Z'}\right\rangle = \sqrt{p_{hex}\ (f)}\left|\psi_{2n}^{Z'}\right\rangle = \sqrt{p_{hex}\ (f)}\hat{U}(B2)\hat{R}(\theta_2)\hat{S}\hat{R}(\theta_1)\hat{U}(B1)\sqrt{p_{hex1}(n)}|n\rangle \tag{2.32}$$

Referring to equation 2.24, as we know the velocity distribution of our hydrogen beam, the only unknown left is the scattering matrix, $\hat{S}$. Therefore, we determine the scattering matrix by fitting to our signal with the elements of the scattering matrix as the fitting parameter.

In the measurements presented below we kept B2 constant, while scanning through values of B1. Looking at equation 2.32, the only term dependent on B1 is $\widehat{U}(B1)$, and as such our experimental signal will oscillate with frequencies determined by the solutions to the Ramsey Hamiltonian. However, referring to equation 2.20, $\widehat{U}(B1)$, is also dependent on the time spent in the field and therefore the velocity of the molecules in the beam and so the frequency of the oscillation of our signal is also dependent on velocity. This can be thought of more intuitively when referring back to the image of a single magnetic moment and equations 2.5 to 2.10. A moment with a higher velocity will precess by a smaller amount than one moving slower as it will spend less time in the fixed length field, and this difference will be more pronounced at higher magnetic fields. The difference in the magnetic field dependent evolution due to different velocities will not exist when there is no field, however this difference will increase at larger fields and the oscillations will become out of phase. The resulting signal will therefore dampen until it no longer oscillates, as demonstrated in Figure 2.3. Here the dashed lines represent single velocities in an overall velocity distribution centred on 1442ms^{-1} with a FWHM of 5% mean velocity. As we can see the single velocities will continue to oscillate at any current and therefore field values. However, the oscillation amplitude of the weighted distribution is reduced further way from 0A. The rate at which the oscillation dampens is dependent on how spread out the velocities in our beam are, which is quantified by the full width maximum of the velocity distribution. Therefore, it is advantageous to have a narrower velocity distribution.

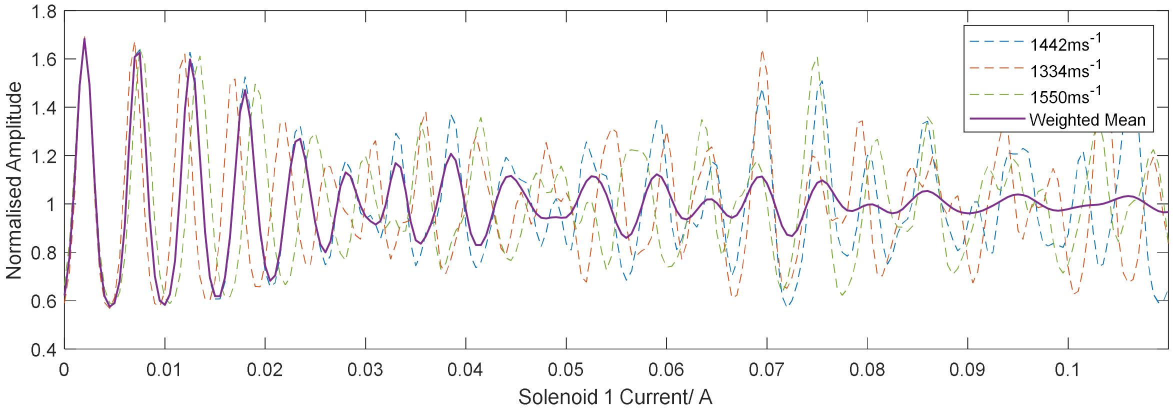

Figure 2.3: Comparison of simulated signal for identity scattering matrix on specular with the weighted mean (gaussian distribution centred on 1442ms^{-1} with a FWHM of 5%).

2.4. Signal Fitting

The fitting algorithm works by simulating signals for two measurements, corresponding to scans of the B1 field for two fixed values of B2, using a given scattering matrix and the equations outlined in section 2.3. Then the differences between each experimental signal and their corresponding simulated signals are minimised simultaneously using the downhill simplex method of Nelder and Mead[53] along with simulated annealing which helps to avoid local minima and reach the global minimum in parameter space. When fitting to the signal we take the individual scattering matrix elements as fitting parameters, along with a parameter for representing background. The background is the same for both signals and is given by:

$$background = mean(calculated\ signal) \times fraction \tag{2.33}$$

The total calculated signal for one of the values of B2 which is compared to the experimental signal measured at the same value of B2 is then found as:

$$total\ signal = calculated\ signal + background \tag{2.34}$$

An important note to make here is that our detector does not give an indication of absolute counts, only the relative counts in a measurement. Due to this, it is convenient to normalise our signal such that the signal mean is 1. Therefore, adding the background has the effect reducing the oscillation amplitude once we renormalise the signal given by equation 2.34. This effect is seen illustrated in Figure 2.4.

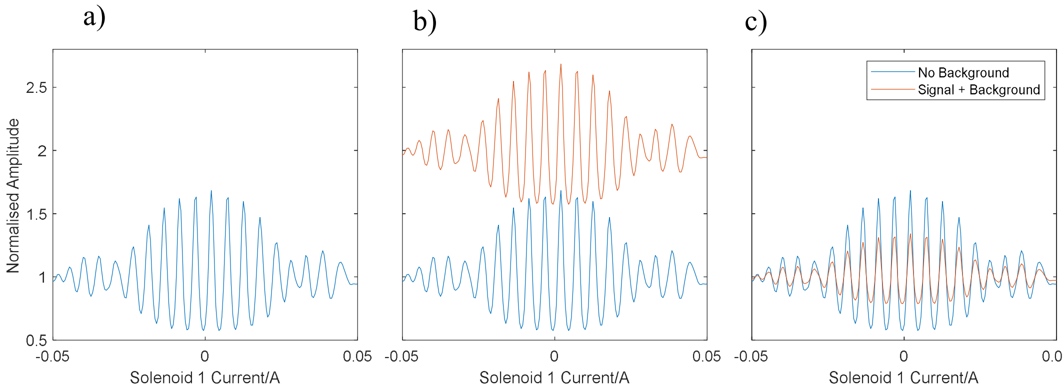

Figure 2.4: a) Simulated signal calculated using an identity scattering matrix with velocity distribution centred on 1442ms^{-1} b) Simulated signal with no background, blue, and background added, orange, as given by Equation 2.33 with fraction = 1 c) Previous two signals presented in panel b after normalisation of the signals with background

Using the same background parameter for both signals, is the reason that two measurements are required to fit the signal. With only one measurement, fit results with different random initial variables would not converge on a common unique scattering matrix. This is because, due to the stretching of the magnitudes when renormalising outlined above and in Figure 2.4, different scattering matrices giving similar oscillation patterns with different magnitudes can both be seen as fit results with different backgrounds. However only one, theoretically, will fit both the first and second measurements when using the same scattering matrix and fraction parameter.

The individual complex scattering elements are split into magnitudes and phases under Euler's formula, giving, or our 9-by-9 scattering matrix, 81 magnitudes, s_{fn}, and 81 phases, k_{fn}. Despite the magnetic properties to be outlined in section 2.6, it will be shown in section 4.1, that the nuclear spin projection state is a spectator. As such the scattering matrix in the m_I subspace is an identity matrix, allowing us to reduce the scattering matrix to:

$$\hat{S}_{m_I' m_J', m_I m_J} = \hat{I}_{m_I} \otimes \hat{S}_{m_J', m_J} = \begin{pmatrix} 1 & 0 & 0 \\ 0 & 1 & 0 \\ 0 & 0 & 1 \end{pmatrix} \otimes \begin{pmatrix} s_{11}e^{ik_{11}} & s_{10}e^{ik_{10}} & s_{1-1}e^{ik_{1-1}} \\ s_{01}e^{ik_{01}} & s_{11}e^{ik_{00}} & s_{0-1}e^{ik_{0-1}} \\ s_{-1}\ e^{ik_{-1}} & s_{-10}e^{ik_{-10}} & s_{-1-1}e^{ik_{-1-1}} \end{pmatrix} \tag{2.35}$$

Where we have separated the scattering matrix elements in m_J space into magnitudes, s_{m_J', m_J}, and phases, k_{m_J', m_J}, and prime denotes the state after scattering.

When molecules scatter from a surface with reflection symmetry, it prevents the surface from distinguishing between both $m_J = \pm 1$ states, and as such the relative populations of the two helicopter states scattering into the diffraction channel and after scattering should be equal to each other. Therefore, we do not expect any difference in the scattering whether the molecule approaches the surface rotating as a helicopter in the clockwise or anticlockwise direction, so we treat them as equivalent. Applying these constraints to our scattering matrix, gives the equalities:

$$s_{11} = s_{-1-1} \tag{2.36}$$

$$s_{10} = s_{-10} \tag{2.37}$$

$$s_{1-1} = s_{-1} \tag{2.38}$$

$$s_{01} = s_{0-1} \tag{2.39}$$

The symmetry restrictions also extend to the phases, for a full explanation please refer to the supplementary information found in reference [22]. The constraints on the phases in our scattering matrix are:

$$k_{11} = k_{-1-1} \tag{2.40}$$

$$k_{10} = k_{-1}\ \ - \pi \tag{2.41}$$

$$k_{1-1} = k_{-11} \tag{2.42}$$

$$k_{01} = k_{0-1} - \pi \tag{2.43}$$

In combination with the earlier assumption, which we will later show to be valid, about the role of nuclear spin as a spectator to scattering, this gives the scattering matrix we will fit to:

$$\hat{S}_{m_I' m_J', m_I m_J} = \hat{I}_{m_I} \otimes \hat{S}_{m_J', m_J} = \begin{pmatrix} 1 & 0 & 0 \\ 0 & 1 & 0 \\ 0 & 0 & 1 \end{pmatrix} \otimes \begin{pmatrix} s_{11}e^{ik_{11}} & s_{10}e^{ik_{10}} & s_{1-1}e^{ik_{1-1}} \\ s_{01}e^{ik_{01}} & s_{00}e^{ik_{00}} & s_{01}e^{ik_{01}+\pi} \\ s_{1-1}e^{ik_{1-1}} & s_{10}e^{ik_{10}+\pi} & s_{11}e^{ik_{11}} \end{pmatrix} \tag{2.44}$$

2.5. Diffraction Channels

As stated in section 2.2.1. the velocity distribution from our beam source is modelled by a gaussian distribution with a 5% full width half maximum of the mean velocity. Then as described in section 2.3 the velocity distribution impacts how quickly the signal in our measurement decays as a function of solenoid current. When measuring specular scattering, the velocity distribution of the hydrogen molecules in our beam reaching the detector will be the same as described for the beam source. This leads to a quicker decay in oscillation of our signal, and thus, when fitting, makes it more difficult to determine the scattering matrix parameters, given equal signal to noise for specular and diffractive scattering. We can narrow the velocity distribution observed at the detector by scattering into a diffraction channel of our surface. To see why this is the case we need to explain what occurs when scattering into a diffraction channel.

The Laue condition for scattering from a lattice is[54]:

$$\boldsymbol{G} = \boldsymbol{k}_f - \boldsymbol{k}_i \tag{2.45}$$

Where $\boldsymbol{k}_i$ and $\boldsymbol{k}_f$ are the initial and final wavevectors of the particle respectively and $\boldsymbol{G}$ is a reciprocal lattice vector. This states that when scattering occurs the change in wavevector for a scattered particle must be equal to a reciprocal lattice vector. This can be reduced to two dimensions when working with surfaces:

$$\boldsymbol{G}_{mn} = \boldsymbol{K}_f - \boldsymbol{K}_i \tag{2.46}$$

where $\boldsymbol{G}_{mn}$ is now a reciprocal vector of the surface mesh, with the integer indices m and n describing the multiples of the principle reciprocal lattice vectors that form $\boldsymbol{G}_{mn}$ as discussed further below (see equation 2.50 onwards), and $\boldsymbol{K}_i$ and $\boldsymbol{K}_f$ are the components of the wavevector in the surface plane, defined as the x and y components, and related to the total wavevector by:

$$\boldsymbol{k} = (\boldsymbol{K}_i, \boldsymbol{k}_{iz}) \tag{2.47}$$

We are able to do this because there is no Laue condition for the z component[55], the only requirement being that $\boldsymbol{k}_{iz}$ is real. In our system the beam paths that $\boldsymbol{K}_i$ and $\boldsymbol{K}_f$ must follow if $\boldsymbol{K}_f$ is to reach the detector is fixed and so they lie in the same plane. In our measurement $\boldsymbol{G}_{mn}$ is then brought to be coplanar with $\boldsymbol{K}_i$ and$\boldsymbol{K}_f$. Therefore, in the case of elastic scattering, $|\boldsymbol{k}_i| = |\boldsymbol{k}_f|$, the scattering condition is reduced to one dimension and becomes:

$$|\boldsymbol{k}_i| \left(\sin(\theta_f) - \sin(\theta_i)\right) = |\boldsymbol{G}_{mn}| \tag{2.48}$$

where θ_f and θ_i are the angle between the scattered and incident beam and the surface normal respectively. The total angle between $\boldsymbol{K}_i$ and $\boldsymbol{K}_f$, $(\theta_f + \theta_i)$, is fixed to an angle $\Phi = 46.2°$, giving the final equation:

$$|\boldsymbol{k}_i|\big(\sin(\Phi - \theta_i) - \sin(\theta_i)\big) = |\boldsymbol{G}_{mn}| \tag{2.49}$$

Therefore, in our experiments, if we know which diffraction channel we want to scatter into, we can estimate the incidence angle where this channel will be found using equation 2.49 since all other values are known.

When scattering into a diffraction channel, equation 2.49 also demonstrates how this can reduce the spread of the velocity distribution of the molecules reaching the detector. For example, specular corresponds to the (0,0) diffraction channel and so $|\boldsymbol{G}_{mn}| = 0$. As the molecules need momentum, $\theta_i = \theta_f = \Phi/2$, any $|\boldsymbol{k}_i|$ can scatter into the channel. Conversely when scattering into any other given diffraction channel the different $|\boldsymbol{k}_i|$ will be scattered to different θ_f, and a much smaller set of velocities will meet the criteria to reach the end of the second arm, $\theta_f + \theta_i = \Phi = 46.2°$. Therefore, due to the narrow angular selectivity (0.04°) of the apparatus, the difference in scattering angles for different velocities when scattering into a non-specular diffraction channel acts as a velocity filter. Correspondingly, when simulating scattered signals for a diffraction peak the full width at half maximum of the gaussian velocity distribution used is reduced to 0.5%.

As stated above, $\boldsymbol{G}_{mn}$ is the reciprocal lattice vector which can be calculated from the primitive reciprocal lattice vectors $\boldsymbol{b}_1$ and $\boldsymbol{b}_2$ using:

$$\boldsymbol{G}_{mn} = n\boldsymbol{b}_1 + m\boldsymbol{b}_2 \tag{2.50}$$

These reciprocal lattice vectors are related to the vectors in real space that define the unit cell of the crystal lattice, $\boldsymbol{a}_1$ and $\boldsymbol{a}_2$ using[56]

$$\boldsymbol{b}_1 = 2\pi \frac{\boldsymbol{a}_2 \times \boldsymbol{n}}{\boldsymbol{a}_1 \cdot \boldsymbol{a}_2 \times \boldsymbol{n}} \tag{2.51}$$

$$\boldsymbol{b}_1 = 2\pi \frac{\boldsymbol{n} \times \boldsymbol{a}_1}{\boldsymbol{a}_1 \cdot \boldsymbol{a}_2 \times \boldsymbol{n}} \tag{2.52}$$

where $\boldsymbol{n}$ is a unit vector normal to the surface, in our case this will be the unit vector $\boldsymbol{z}$ in the z-direction.

The chromium crystal lattice has a body centred cubic structure with a basis of one chromium atom with a lattice constant d of 2.91Å. Truncating the crystal with a (110) plane gives the surface mesh seen in Figure 2.5. The primitive unit vectors which describe the unit cell of the surface mesh can be seen overlayed as yellow and purple arrows on Figure 2.5, labelled $\boldsymbol{a}_1$ and $\boldsymbol{a}_2$ respectively. With $\boldsymbol{x}$ and $\boldsymbol{y}$

representing unit vectors in the surface plane as seen in Figure 2.5, the primitive unit vectors are described by:

$$\boldsymbol{a}_1 = \frac{1}{\sqrt{2}} d\boldsymbol{x} + \frac{1}{2} d\boldsymbol{y} \tag{2.53}$$

$$\boldsymbol{a}_2 = \frac{1}{\sqrt{2}} d\boldsymbol{x} - \frac{1}{2} d\boldsymbol{y} \tag{2.54}$$

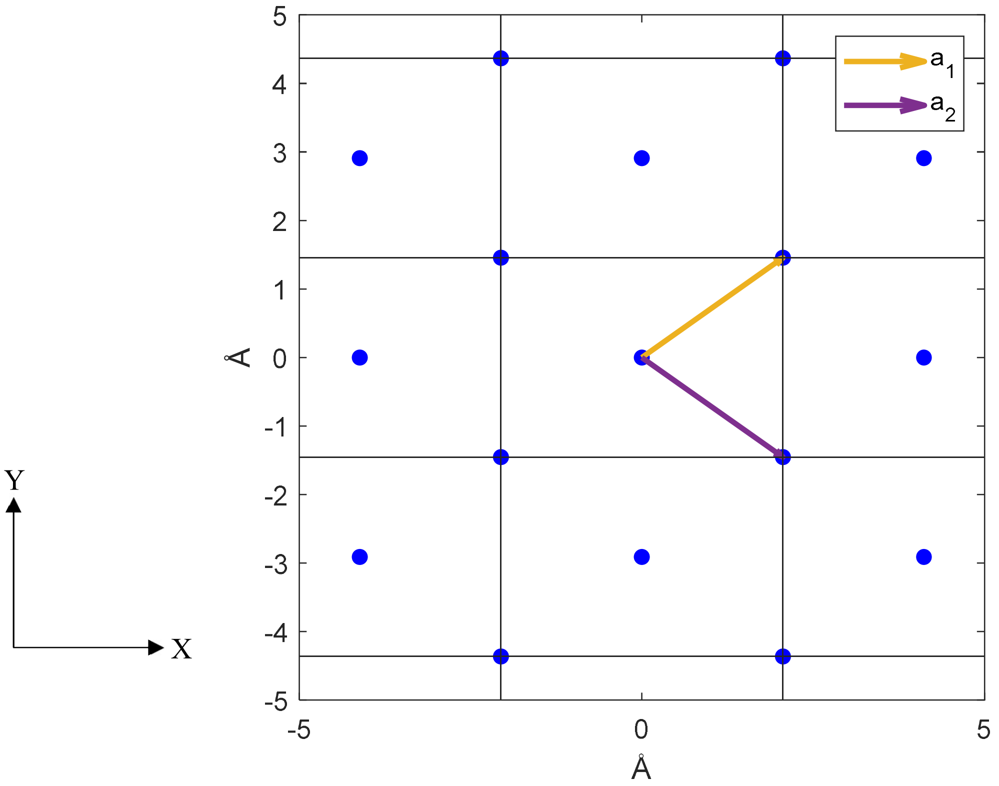

Figure 2.5: Surface mesh of Cr(110) where the blue dots represent chromium atoms and the yellow and purple arrows the primitive unit vectors $\boldsymbol{a}_1$ *and* $\boldsymbol{a}_2$ *as written in equations 2.53 and 2.54, respectively. The* $\boldsymbol{x}$ *and* $\boldsymbol{y}$ *unit vectors are also shown in the bottom left.*

Using these vectors and equations 2.53 and 2.54 gives

$$\boldsymbol{b}_1 = \frac{2\sqrt{2}\pi}{d} \left(\frac{1}{2} \boldsymbol{x} + \frac{1}{\sqrt{2}} \boldsymbol{y} \right) \tag{2.55}$$

$$\boldsymbol{b}_2 = \frac{2\sqrt{2}\pi}{d} \left(\frac{1}{2} \boldsymbol{x} - \frac{1}{\sqrt{2}} \boldsymbol{y} \right) \tag{2.56}$$

Figure 2.6 shows the reciprocal lattice of the Cr(110) surface, along with the reciprocal lattice vectors $\boldsymbol{b}_1$ and $\boldsymbol{b}_2$ as yellow and purple arrows respectively. The different reciprocal lattice vector points, and thus diffraction channels, are also labelled. As can been from the form of the vectors given in equations 2.53 to 2.56, and by comparing Figures 2.5 and 2.6, the reciprocal net is simply a stretch in $\boldsymbol{x}$ and $\boldsymbol{y}$ of the real space surface mesh. In our measurements we will scatter into the (0,1) diffraction channel, i.e., $m = 0$ and $n = 1$.

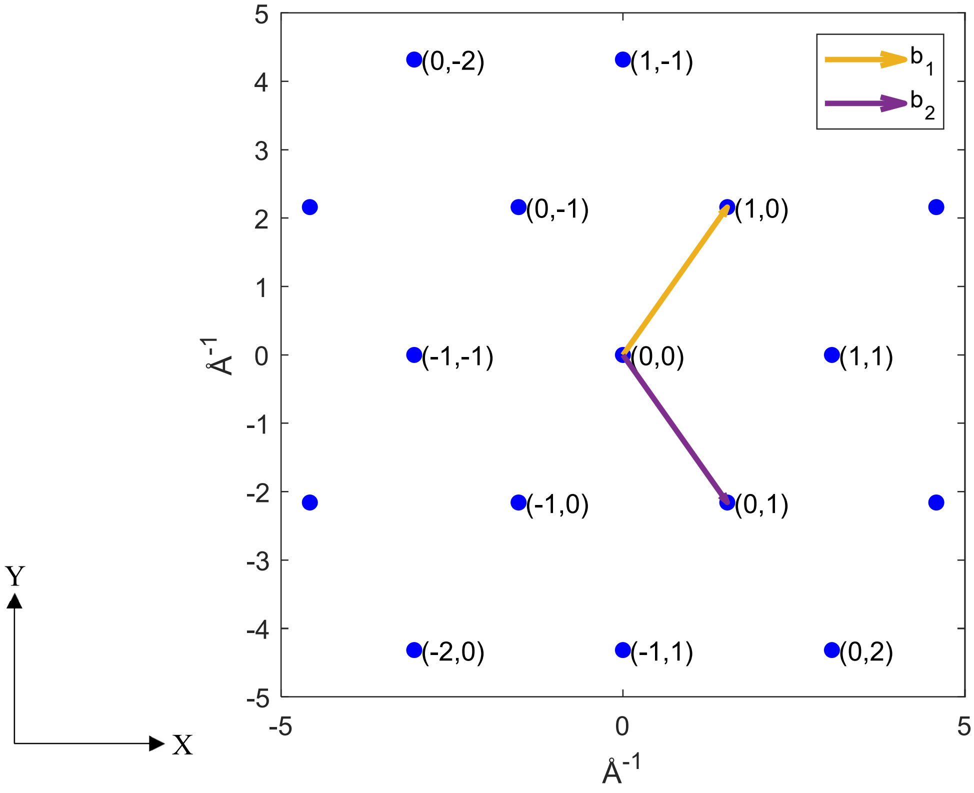

Figure 2.6. Reciprocal lattice of Cr(110) where the blue dots represent the reciprocal lattice points and the yellow and purple arrows the reciprocal lattice vectors $\boldsymbol{b}_1$ *and* $\boldsymbol{b}_2$ *as written in equations 2.55 and 2.56, respectively. The* $\boldsymbol{x}$ *and* $\boldsymbol{y}$ *unit vectors are also shown in the bottom left.*

2.6. Magnetic Properties of H-Cr(110)

Although above in section 2.4 we make the assumption that despite the antiferromagnetic nature of chromium we still find the nuclear spin projection state to be a spectator to scattering, these properties still provide important context for our measurements. The magnetic properties of chromium have long been an object of scientific interest[57, 58]. Below the Neel temperature of 311K, above which chromium is paramagnetic, bulk chromium exhibits itinerant static spin-density waves (SDWs) incommensurate with the lattice, characterised by the nesting properties of the Fermi surface of the lattice. Itinerant means that the magnetic moments and fluctuations are localised in reciprocal space rather than real space[59]. Spin density waves modulate the density of electronic spins within the crystal lattice along the direction of the SDW. The SDW means that Cr is antiferromagnetic. If the SDW were commensurate, meaning its wavelength is a rational fraction or multiple of the lattice constant, and if the wavelength is twice the unit cell length, then the local magnetic moments on neighbouring Cr atoms have opposite directions, as seen in Figure 2.7a. However, the SDW for pure chromium is incommensurate, resulting in electronic spin modulation as seen in Figure 2.7b. The polarisation of the SDW, i.e. longitudinal or transverse, and the wavelength are both temperature dependent[60]. The SDW can run in any of the $\langle 100 \rangle$ directions, and as such can run in the plane of the (110) surface or along two different out-of-plane directions, as seen in Figure 2.8. When covered in hydrogen, as it will be in this study, the SDW of chromium becomes commensurate[61], demonstrating an interesting possibility of the control of the SDW in chromium based films[62].

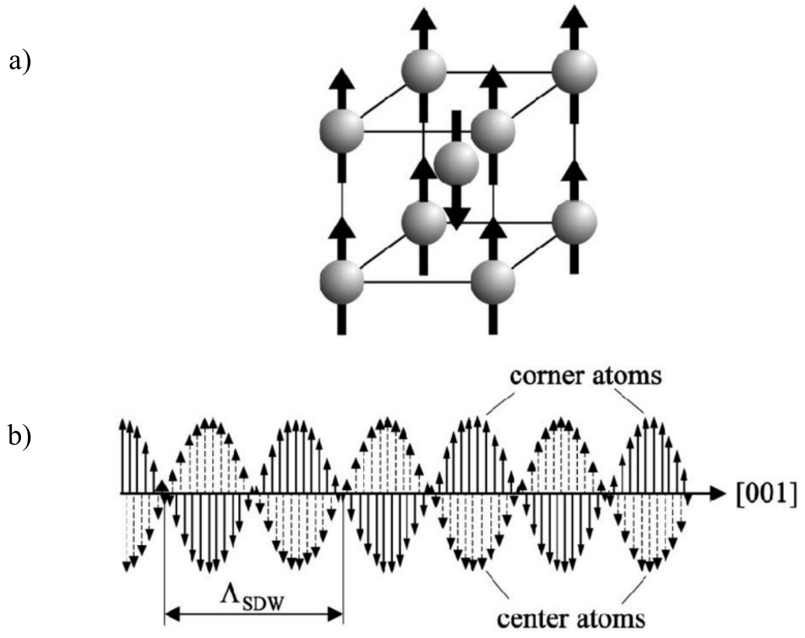

Figure 2.7:a) Commensurate antiferromagnetic spin density wave structure of bcc Cr b) Incommensurate spin density wave structure of bcc Cr along the $\langle 001 \rangle$ *lattice direction with wavelength, corner and centre atoms labelled. Taken from [58].*

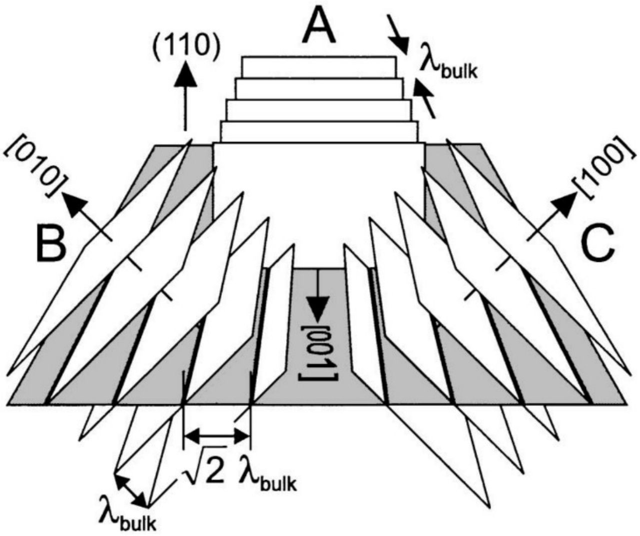

Figure 2.8: Schematic of the wavefronts of the three possible directions of the Cr SDW relative to the (110) plane, with the SDW wavelength in the bulk labelled. Taken from [60].

3. Experimental Methods

3.1. Surface Preparation

The first step of surface preparation was cleaning the chromium surface of any other adsorbed atoms or molecules before passivating it with a monolayer of hydrogen. Previous studies have demonstrated the effective removal of surface contaminants with multiple cycles of argon ion bombardment and subsequent annealing[63-65]. Following this, in our experiment the cleaning was achieved through argon ion bombardment using a sputter gun attached to the scattering chamber which contained the surface heated to ~600K, after which the surface was annealed by heating to ~800K and then cooling it back down. This process was repeated for several rounds, with the final round being performed at a lower temperature of ~300K with annealing performed at ~500K. The argon ion bombardment removes atoms from the surface, with the intention of revealing a rough pure chromium surface below, with the annealing then aiming to reorder the surface as a lower energy defect free (110) surface.

The first step in checking the cleanliness of the surface was using low-energy electron diffraction (LEED). LEED scatters a beam of electrons into diffraction channels as defined by the Laue condition explained in section 2.5, and therefore by detecting the locations of the scattered electrons where they constructively interfere, we informed about the long-range order of our surface. A surface with an ordered overlayer of another atom and a clean chromium surface would both give a LEED pattern, a clean sputtered but not annealed surface, however, would not. Therefore, after sputtering and annealing, observing a clean LEED pattern representative of the expected reciprocal net should be indicative of a clean surface. Example images obtained for the Cr(110) surface are shown in Figure 3.1, which can be compared with that determined by the expected structure of the Cr(110) surface, as demonstrated in section 3.2. A more in depth explanation of LEED and its uses in surface structure determination can be found in[56, 66].

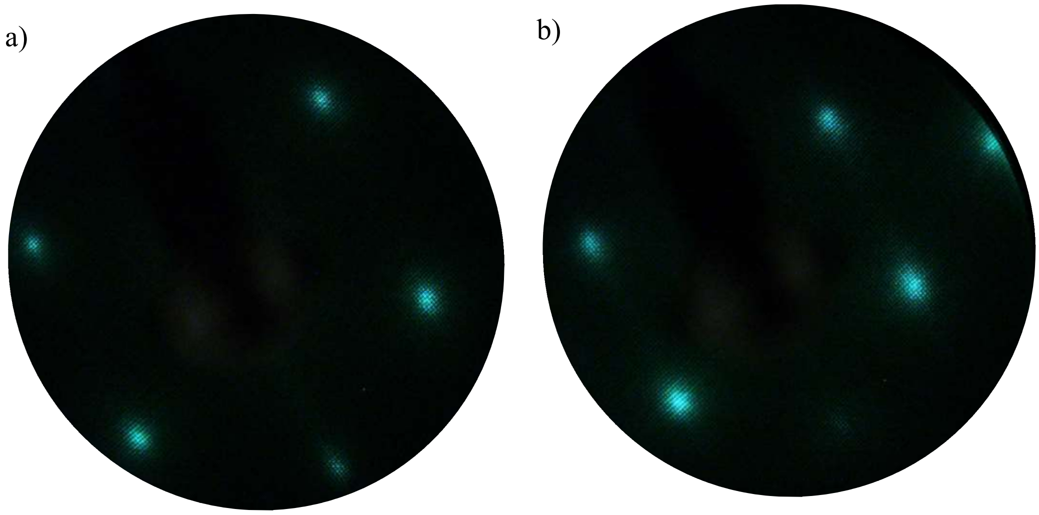

Figure 3.1 a) LEED image of the surface at an electron energy of 120eV and focus of 144V b) LEED image of the surface at an electron energy 175eV and focus of 210V.

Once the surface was deemed sufficiently clean by looking at LEED images, hydrogen was then deposited onto the surface in order to passivate it. The deposition of the hydrogen could be monitored by aligning the surface to the specular position before the deposition and observing the change in the amount of scattered hydrogen reaching the end of the second arm over time throughout the deposition. The surface was considered as completely covered when the intensity of scattered hydrogen no longer changed.

3.2. Alignment and Optimisation Measurements

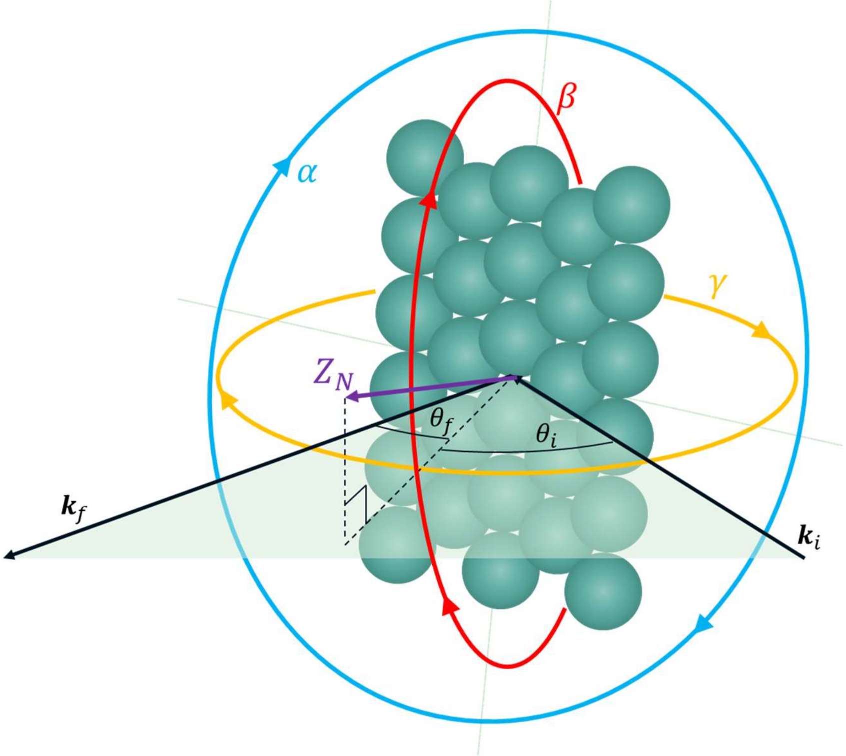

Figure 3.2: Illustration of the different angles that the crystal can be rotated through along with how incidence angle is measured and a visual of the scattering plane (X-Z in Figure 2.1) in translucent green.

Experimentally helium atom scattering is used for structural analysis by observing the locations and intensities of the various diffractions channels[66]. In our study we employ it to aid with assessing the cleanliness of the surface and aligning of the crystal azimuth. However, because our apparatus is limited to the in-plane scattering used to simplify the Laue condition in equation 2.48, the surface must be rotated so that any scattering performed into the diffraction channel with reciprocal lattice vector, $\boldsymbol{G}_{mn}$, is coplanar with incoming and outgoing wavevector components within the surface plane, $\boldsymbol{K}_i$and $\boldsymbol{K}_f$, in order for the incident angle in, θ_i, in equation 2.48 to be the same as the θ_i we measure as shown in Figures 3.2 and 2.1. Practically this means rotating the crystal so that in reciprocal space the desired $\boldsymbol{G}_{mn}$ lies within the X-Z plane in Figure 2.1, which lies horizontally in our laboratory. We are able to rotate the surface in three angles, illustrated in Figure 3.2, designated alpha (α), beta (β) and gamma (γ). Alpha denotes the rotation of the crystal azimuth around the surface normal, beta denotes the tilt of the surface, i.e., the angle between the surface normal and the scattering plane and gamma denotes a rotation of the surface normal within the scattering plane.

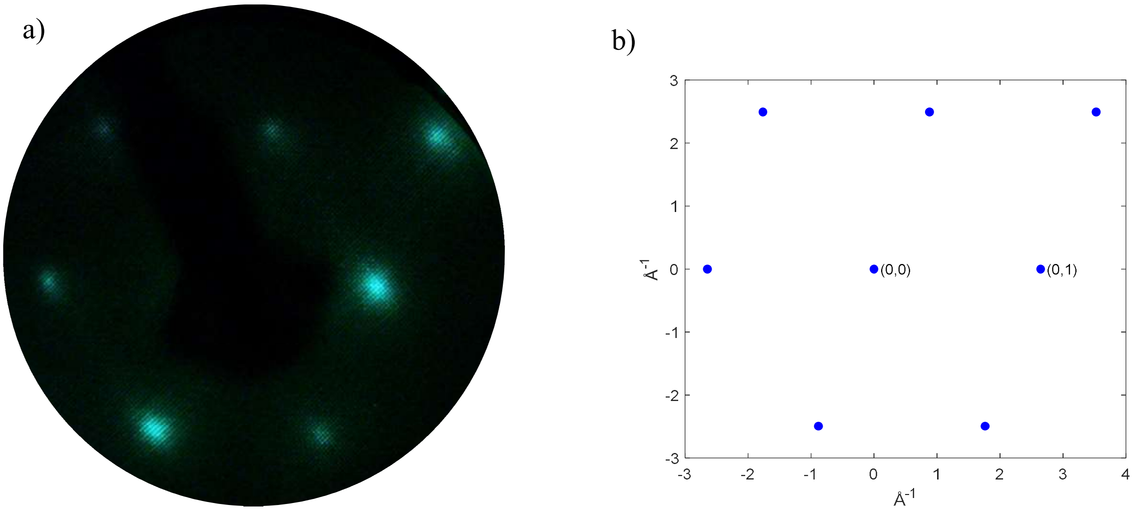

Figure 3.3:a) LEED image of the Cr(110) surface after rotation of alpha at an electron energy of 175eV and focus of 210eV. b) Reciprocal lattice with same orientation as the LEED image in panel a).

In order to determine the required alpha rotation, the previous LEED images in Figure 3.1 were used by observing how much rotation was required to bring the (0, 1) channel into the scattering plane. To achieve scattering of our molecular beam along the $\langle\bar{1}12\rangle$ crystal azimuth the crystal would need to appear to be oriented to produce the reciprocal lattice as in Figure 2.6, with the purple arrow in Figure 2.6, being horizontal in the image. This appears to have brought the crystal into the correct alignment by the comparison displayed in Figure 3.3. However, this is further checked by finding the locations of both the (0, 1) and $(0, -1)$ diffraction channels in a helium scattering experiment. First, we calculate the reciprocal lattice vector magnitude, using a lattice constant of 2.91Å this gives $|\boldsymbol{G}_{11}| = |\boldsymbol{G}_{1-1}| = 2.64\text{Å}^{-1}$. For simplicity we will define $\gamma = 0$ at specular scattering conditions, i.e., where $\theta_i = \theta_f = \Phi/2$. Then using equation 2.49, along with equation 2.2 for a nozzle temperature of 100K, gives an incident angle of $\theta_i = 10.16°$. This means that we expect to find a diffraction peak at $\Phi/2 - 10.16 = 12.94°$ from our specular position. Due to the symmetry of the surface and its reciprocal mesh, we expect the $(0, -1)$ peak at 12.94° in the opposite direction. The first check was to determine if we could find the diffraction peaks at the expected value of γ. Figure 3.4a shows the scan of gamma around the expected position of specular $+12.94°$ demonstrating the found peak at $\gamma = 13.1°$, confirming that the surface is clean as well as aligned in alpha. The precision quoted here arises from the resolution of our scans. We have angular precision of 0.01 degrees on angular positions, however, as can be seen when looking at the scans, the width of the peaks limits the accuracy significantly. When alpha is completely properly aligned so that the $\langle\bar{1}12\rangle$ crystal plane lies in the scattering plane, then the surface normal will also lie in the scattering plane, and as such we can move between the (0, 1) and $(0, -1)$ diffraction channels by only moving through gamma. We confirm this by scanning through beta at the locations of both diffraction channels, the results of these measurements can be seen in Figures 3.4b and 3.4c. Looking at the peaks of both scans gives values of $\beta = 1.3^\circ$, relative to an arbitrary zero, demonstrating that the diffraction channels are found at the same value of tilt in the surface which is thus the value of beta for which the surface normal lies in the scattering plane. As such we confirm that our surface is well aligned and clean.

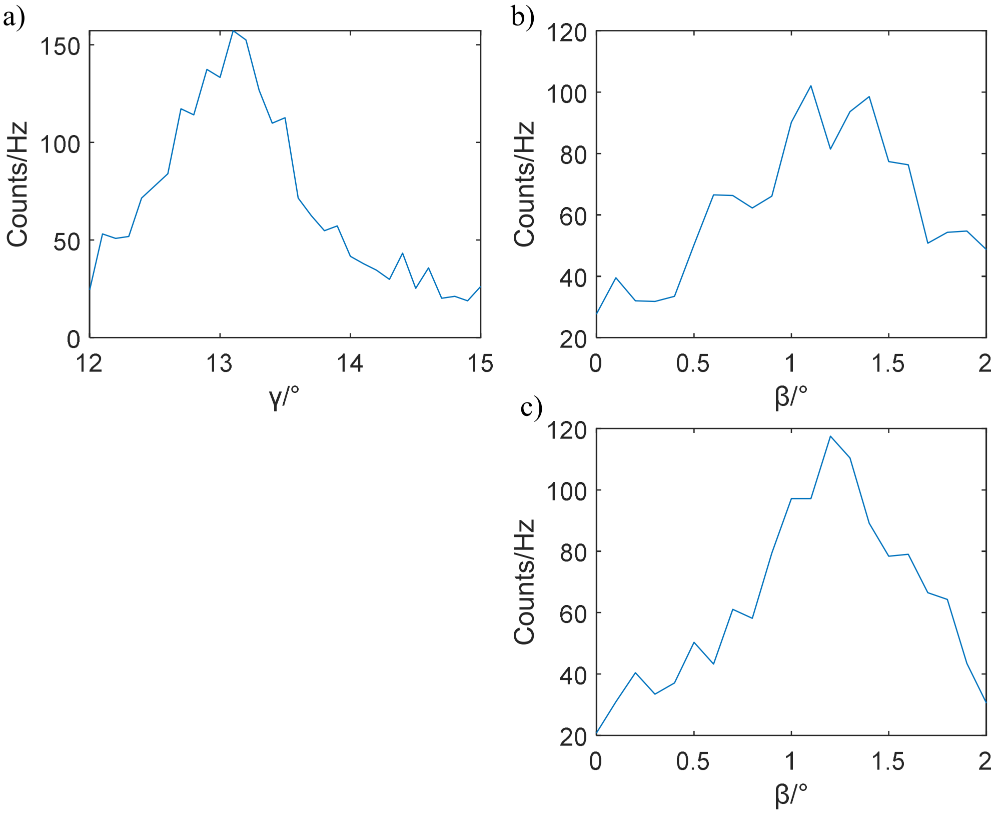

Figure 3.4:a) Gamma scan using helium at first expected diffraction peak b) beta scan at peak of gamma at 13.1° (0, 1) c) beta scan at opposite peak at gamma -13.1° $(0, -1)$

With the surface aligned well in alpha and beta, we then switched from helium scattering to a hydrogen beam. After finding the position of specular again, to help with finding the diffraction channels the surface position within the chamber was optimised. The position of the surface can be manipulated slightly by a translatable stage which can move the surface through the X-Z plane as seen in Figure 2.1. The position is then optimised by monitoring the signal while moving the surface through both directions and iteratively finding the peak of both beta and gamma. Once this is complete the gamma and beta angles for specular are found again. Using equations 2.49 and 2.2, with a nozzle temperature of 100K, $\theta_i = 4.64^\circ$ meaning that we expect to find the diffraction channels $\Phi/2 - 4.64 = 18.46^\circ$ from specular. Figure 3.5 shows a gamma scan indicating the specular and (0,1) diffraction peak, the peak of which was found at 18.52° from specular.

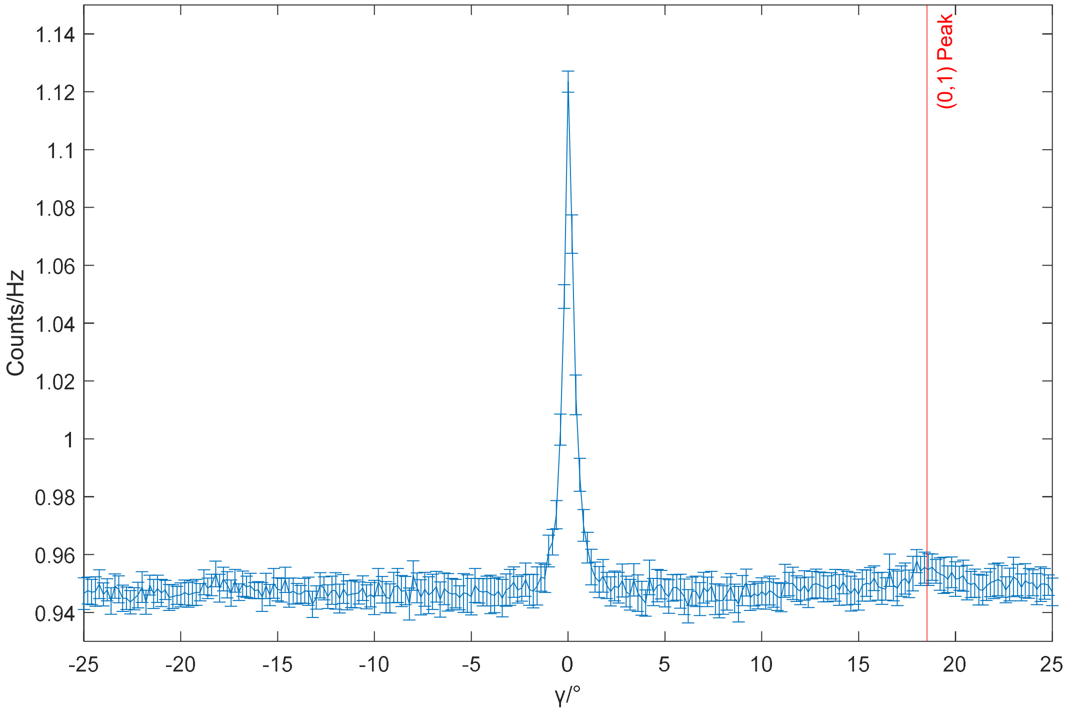

Figure 3.5: Gamma scan, in blue, demonstrating specular and diffraction peak, indicated by the red line, for H_2 scattering from H-Cr(110).

3.3. Measurement Parameters

Once the crystal is aligned so that the hydrogen beam scatters into a channel which leads to the detector at the end of the second arm, we can perform B1 scan measurements, varying the current supplied to the first solenoid, and thus the resulting field, while keeping the current in the second solenoid constant. In this study three different measurements were performed. In all three the surface temperature was maintained at 150K, and the nozzle was at 100K. The first was a measurement scattering from specular, scanning from -0.12A to 0.12A, thus a field integral of -13.42 to 13.42 gauss metre, in the first solenoid, measuring at 481 points, with 0A current in the second solenoid. The measurement was repeated 20 times (loops) to improve the signal to noise ratio. Two measurements were performed while scattering into the (0,1) diffraction channel of the surface, where both scanned the first solenoid current from 0 to 0.15A (field integral of 0 to 16.77 gauss metre) measuring at 301 current values. The current in the second solenoid was 0A for the first diffraction channel measurement with 325 loops performed, and 0.5A (55.90 gauss metre field integral) for the second measurement, repeated for 377 loops.

4. Results & Discussion

4.1. Specular Measurement

This section will present the results of the B1 scan performed at specular scattering conditions on the (110) hydrogen-passivated chromium surface, H-Cr(110). It will explore how the raw data was manipulated and then compared to the signal produced by an identity scattering matrix. Finally, the conclusions we can draw from this result will be discussed.

As explained in section 3.3 each of the scans performed consisted of multiple loops over a range of first solenoid current, I_{B1}, with the second solenoid held at a constant current, I_{B2}. Before averaging the data, both the constant background in our signal and the non-negligible drift in our detector must be accounted for. For the background correction, the background was measured every 100th value of I_{B1}. The background was on average 83.1% of the signal measured at the detector, arising from a combination of H_2 in the UHV and parahydrogen in the beam. To correct for background, we simply subtract the most recent background measurement in the scan from each point in the current scan. To account for the drift in the detector, we first fit a third order polynomial to each individual current scan. By dividing the background corrected counts through by the polynomial fit we get drift corrected data normalised to a mean value of 1. With these sources of error accounted for, we can then average the data to give our final measurement, with the error of the average signal for each I_{B1} value calculated by:

$$err_{I_{B1}} = \frac{\sigma_{I_{B1}}}{\sqrt{n}} \tag{4.1}$$

where $\sigma_{I_{B1}}$ is the standard deviation of all the points measured at I_{B1} after the background and drift correction and n is the number of points (loops). Performing this processing for the measurement on specular, gives us the result for the current scan plotted with the blue markers in Figure 4.1.

As stated in section 2.2.1, using equation 2.2, with a nozzle temperature of 100K, we can estimate the mean velocity in our beam to be 1442ms^{-1}, then model our beam with a gaussian distribution with a 5% full width half maximum of our mean velocity. Taking this velocity distribution and using it along with an identity matrix results in the signal shown by the red line in Figure 4.1. It does seem to be that the experiment and simulation are similar, however more careful inspection reveals over half of the points in fact lie outside of the error bars. Because our calculation of error is as given above in equation 4.1, we would expect a good fit to the data to lie within two-thirds of the error bars. As we show below, this is not because our identity scattering matrix is a bad approximation, rather due to the velocity distribution used. This becomes clearer when looking at the Fourier transform of both our experimental and identity simulated signal, shown in Figure 4.2a.

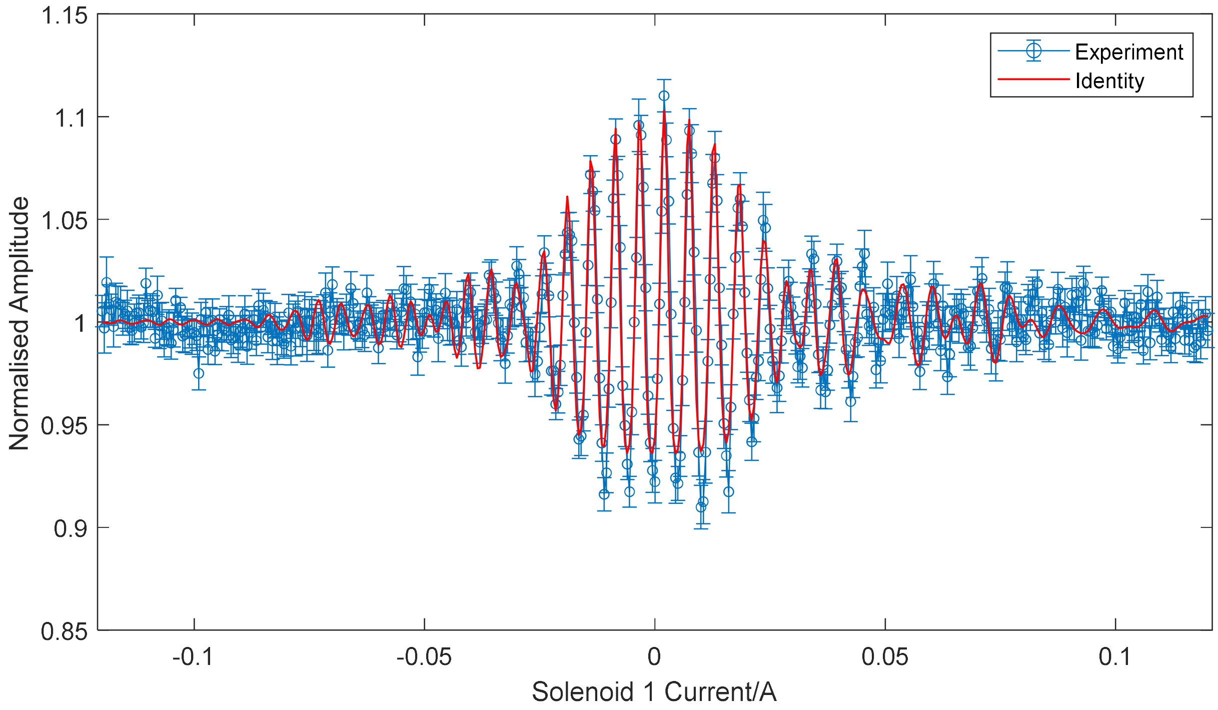

Figure 4.1: Comparison of the experimentally measured specular signal, in blue, and signal calculated using an identity scattering matrix with a mean velocity of 1442ms^{-1}, in red.

In order to understand the Fourier spectra produced through Fourier transformations of our signals, we perform variable substitutions following the methods introduced originally for helium-3 spin echo experiments[67], and later extended to magnetic manipulation of molecules[22, 43, 68]. As demonstrated in section 2.2.3, for a single spin with gyromagnetic γ propagating through the machine, the signal can be given by equation 2.10. However, our system is not so simple in that there are many different frequencies corresponding to transitions between the different states of hydrogen, arising from the Ramsey Hamiltonian in equation 2.11. For simplicity we can look at the signal as if there is just one velocity and a continuous range of gyromagnetic ratios (frequencies). We can then express the signal as an integral over all possible values for γ:

$$signal(I) = \int_{-\infty}^{\infty} P(\gamma)\cos\left(\frac{\gamma}{v}B_{eff}I\right)d\gamma \tag{4.2}$$

Where $P(\gamma)$ is a probability distribution giving the probability of a given γ contributing to the signal, v is the velocity of the molecules, B_{eff} is the effective field as defined in equation 2.8 and I is the solenoid current. To give equation 4.2 a more useful form we make a substitution, κ, defined as:

$$\kappa = \frac{B_{eff}I}{2\pi v} \tag{4.3}$$

Performing this substitution gives us the signal as a function of κ:

$$signal(\kappa) = \int_{-\infty}^{\infty} P(\gamma)\cos(2\pi\kappa\gamma)\, d\gamma = \int_{-\infty}^{\infty} \frac{P(\gamma)}{2}\left(e^{2\pi i\kappa\gamma} + e^{-2\pi i\kappa\gamma}\right) d\gamma \tag{4.4}$$

Looking at the form of equation 4.10 we can see how we may be able to extract the distribution of γ by Fourier transforming the signal. Applying the Fourier transform to the signal, we get the spectrum:

$$\begin{aligned} spectrum(\gamma') &= \int_{\kappa=-\infty}^{\kappa=\infty} signal(\kappa) e^{-2\pi i\kappa\gamma'} d\kappa = \int_{\kappa=-\infty}^{\kappa=\infty} \int_{-\infty}^{\infty} \frac{P(\gamma)}{2}\left(e^{2\pi i\kappa} \quad + e^{-2\pi i\kappa\gamma}\right) e^{-2\pi i\kappa\gamma'} d\gamma d\kappa \\ &= \int_{\kappa=-\infty}^{\kappa=\infty} \int_{\gamma=-\infty}^{\gamma=\infty} \frac{P(\gamma)}{2}\left(e^{2\pi i\kappa(\gamma-\gamma')} + e^{-2\pi i\kappa(\gamma+\gamma')}\right) d\gamma d\kappa \\ &= \int_{\gamma=-\infty}^{\gamma=\infty} \frac{P(\gamma)}{2}[\delta(\gamma-\gamma') + \delta(\gamma+\gamma')]\, d\gamma = \frac{P(\gamma')}{2} + \frac{P(-\gamma')}{2} \end{aligned} \tag{4.5}$$

The result from equation 4.5 demonstrates that applying the Fourier transform to a signal in κ will give us a spectrum consisting of the probability distribution of $P(\gamma)$ and the same distribution mirrored around zero. Here we ignore the $-\gamma$ results because these are not physical so only consider the positive spectrum. Because our experimental data is discrete rather than continuous, we apply the discrete Fourier transform to it. The resulting discrete spectrum will consist of equally spaced gamma values starting at zero with the same number of points as the current scan. The spacing in gamma is given by:

$$\Delta\gamma = \frac{1}{\kappa_{max} - \kappa_{min}} \tag{4.6}$$

Thus, using the definition of κ, we get:

$$\Delta\gamma = \frac{2\pi v}{B_{eff}(I_{max} - I_{min})} \tag{4.7}$$

An important note here is that only the mean velocity is used for equation 4.7 and so does not account for the velocity distribution. Therefore, the spectrum will also contain the effects of the velocity distribution, broadening the peaks in the Fourier spectrum.

By applying the transform as explained above to both the experimental and simulated signals we produce the two Fourier spectrums seen in Figure 4.2a. As is evident in the plot, the primary peaks in the spectrums of the two signals do not match. We can attribute this to our calculation of the mean of our velocity distribution, using equation 2.2, being only an estimation for an ideal monoatomic supersonic beam. Thus, by increasing the mean velocity for our simulated signal, the two peaks in the Fourier spectrums can be brought to be at equal frequencies, as shown in Figure 4.2b. The signal resulting from using an adjusted mean velocity of 1470ms^{-1} can be seen in Figure 4.3 in comparison to the experimental signal, and the calculated signal can be seen to be in better agreement than when a slower velocity is used for the calculation, as seen in Figure 4.1. This difference in velocity would correspond to a 4K difference in nozzle temperature using equation 2.2. This could arise from a nonideal expansion process, the fact that the temperature sensor, that measures the nozzle temperature is not positioned exactly at the tip of the nozzle, the accuracy the sensor, temperature gradients throughout the nozzle or any combination of these factors. The new calculated signal agrees much better with our experimental signal, with the signal lying within 66% of the error bars.

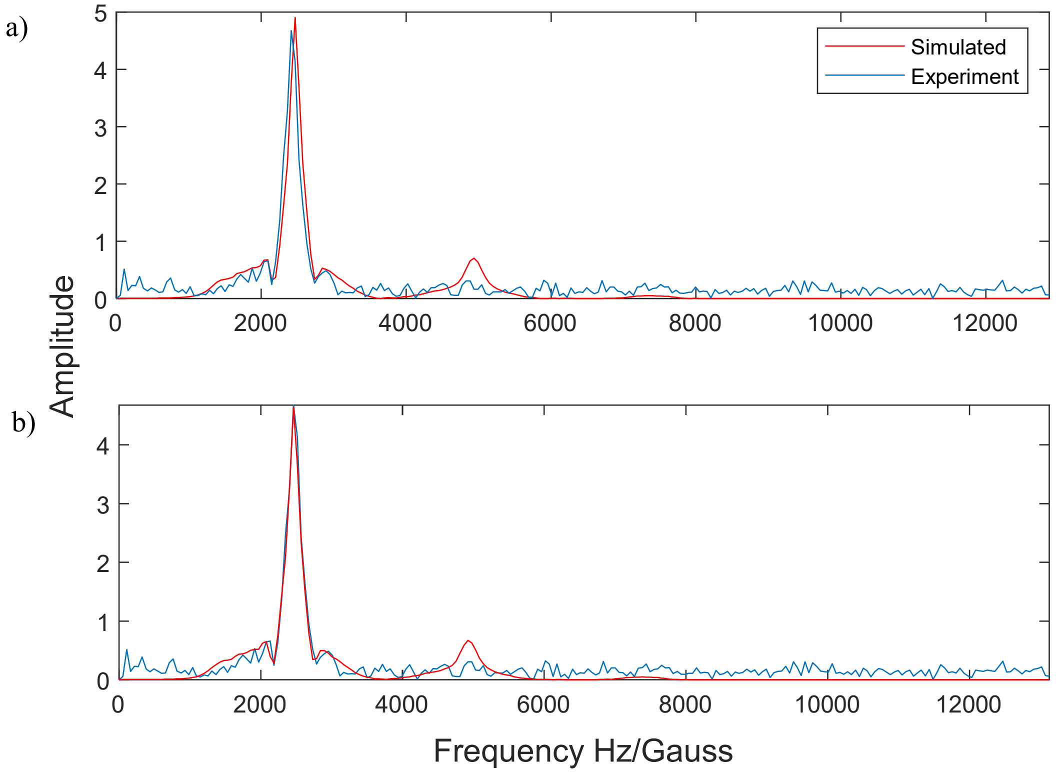

Figure 4.2:a) Comparison of the Fourier transform for the specular measurement, blue, and a simulated signal calculated at a velocity of 1442ms^{-1}*, red b) Comparison of the Fourier transform for the specular measurement, blue, and a simulated signal calculated at a velocity of 1470ms*$^{-1}$*, red.*

The results displayed in Figure 4.3, support the idea that the scattering matrix for hydrogen molecules interacting with H-Cr(110) is an identity matrix, or at least very similar to an identity matrix. This means that the hydrogen sees the surface as a mirror at specular. Therefore, there are no transitions between cartwheel, $m_J = 0$, and helicopter, $m_J = \pm1$, rotational projection states as a result of interacting with the surface. The good fit of the data to an identity scattering matrix also suggests the assumption that the scattering process doesn’t change the nuclear spin projection state, is a good one. As the magnetic properties of the surface will remain the same regardless of whether scattering from specular or a diffraction channel, we can utilise this result when analysing the diffraction channel scattering measurements presented later in this chapter. Therefore, this has provided us with the evidence to make the assumption, as stated in section 2.4, that the scattering matrix will always be identity in the m_I Hilbert space. We can thus reduce the scattering matrix to a 3-by-3 matrix in the m_J space tensor product with our 3-by-3 identity matrix in m_I space, leading us to equation 2.35.

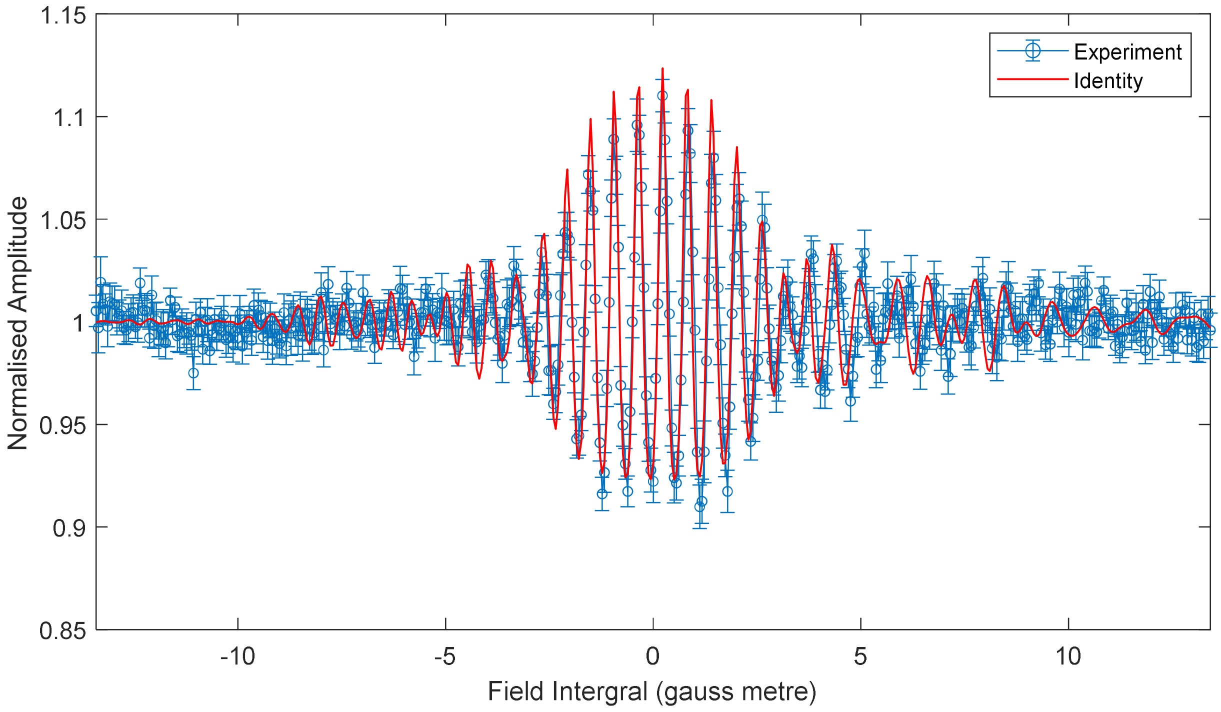

Figure 4.3: Comparison of the experimentally measured specular signal, in blue, and signal calculated using an identity scattering matrix with a mean velocity of 1470ms^{-1}, in red.

4.1.1. Extracting an Identity Matrix from a Specular Measurement

As explained in section 2.4, two measurements at different I_{B2} are required to allow us to fit a measurement and get a scattering matrix. Unfortunately, we didn't perform such a second measurement for specular scattering. Nevertheless, for future studies, it will still be worthwhile to determine if we are able to obtain a scattering matrix by fitting a specular measurement. The difficulty with fitting a scattering matrix from a specular measurement in comparison to a diffraction peak measurement, lies within the quicker decay of the signal in terms of solenoid current than compared with the diffraction channel measurement, which means that there are fewer oscillations in the signal. This occurs, as outlined in more detail section 2.5 due to the larger spread of velocities at specular due to the high angular selectivity of the machine reducing the spread of velocities in a diffraction channel.

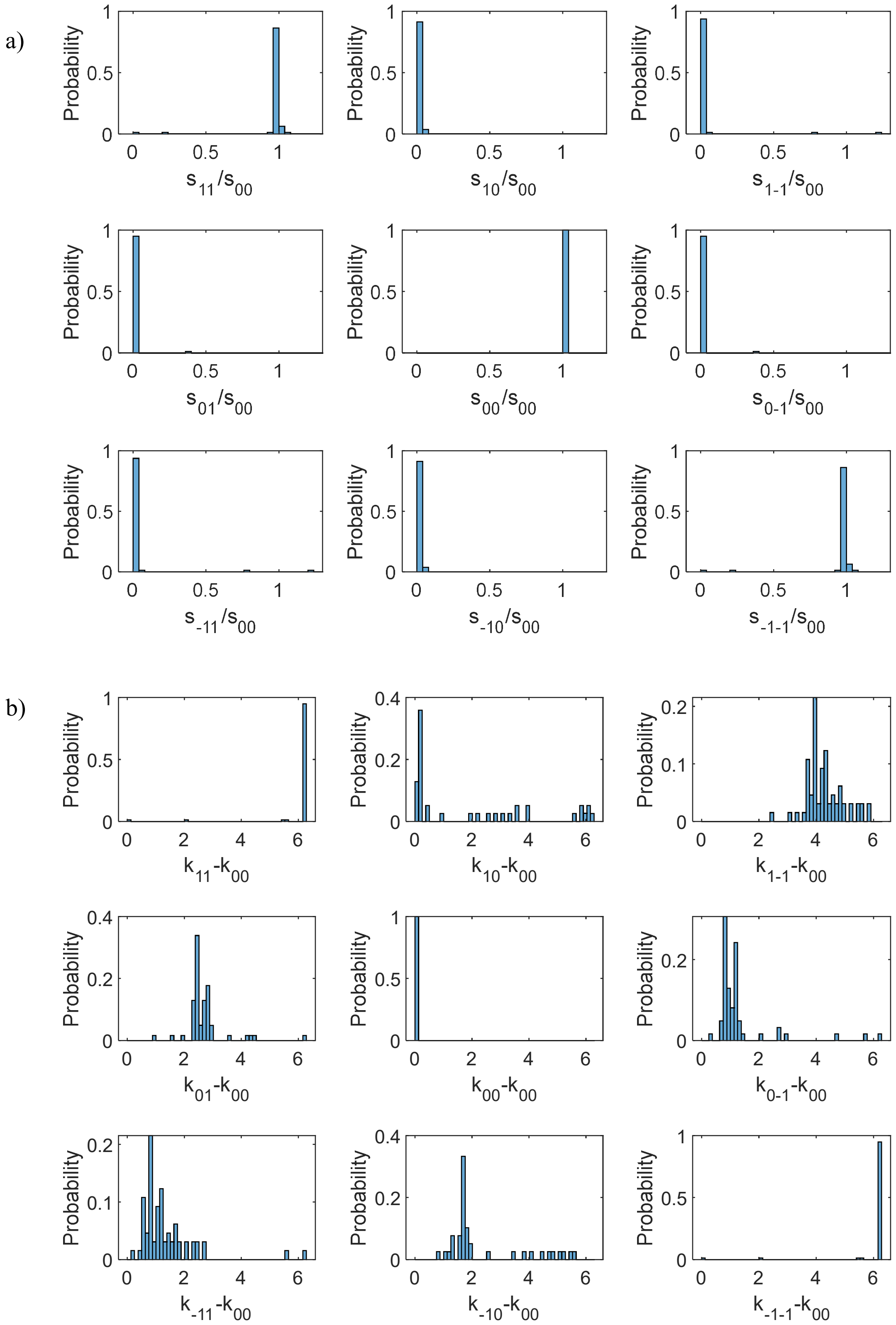

Figure 4.4: a) Histogram plot displaying all fit result values for the nine scattering matrix magnitudes obtained by fitting the specular measurement and a second simulated signal, normalised by dividing by the s_{00} magnitude value b) Histogram plot displaying all fit result values for the nine scattering matrix phases from the same fit results that produced panel a, normalised by subtracting the k_{00} phase value.

In order to test the fitting code's capability in this regard, a simulated signal needed to be produced at a different second solenoid current, I_{B2}, selected to be 0.5A, which produces a field integral of 55.90 gauss metre. Then using the same velocity distribution as the previous section, with a mean velocity of 1470ms^{-1}, and an identity scattering matrix a simulated signal was created at this second current value. To replicate our experimental conditions more accurately, random noise was added to the signal. This was achieved by calculating the average error of each point in our specular measurement and then dividing this through by the amplitude of oscillation (maximum value minus minimum value). Random noise values were then generated in a normal distribution with a standard deviation of our experimental error over oscillation amplitude multiplied by the oscillation amplitude of the simulated signal.

Using the experimental and simulated signal to fit our scattering matrix as described in section 2.4, we are able to get fit results for each of the nine magnitudes and nine phases in our 3-by-3 matrix for each time we run the fitting algorithm for the two measurements. By fitting to the signals multiple times, with a different starting point each time, we can test if the algorithm reaches a similar result each time. As stated in section 2.4, the fitting is not sensitive to absolute values of magnitudes and phases and so they must be normalised relative to a value in the matrix. Throughout this thesis, the magnitudes were normalised by dividing by the largest value in the best fit, and the phases by subtracting the phase corresponding to the largest magnitude value in the best fit. In the case of the specular measurements this was s_{00} and k_{00}. The data was fitted 100 times using the fitting algorithm described earlier, giving 100 results for the scattering matrix. The fitting results to the experimental and simulated signals are displayed in histogram format, in Figure 4.4, with each histogram representing one of the nine magnitudes or one of the nine phases of the scattering matrix.

As is evident from the above fit results, almost all the fits found an identity scattering matrix as the result, with the few that didn't having much larger errors in comparison with the data than those that found an identity matrix. The phases along the diagonal are approximately equal, giving an identity matrix. The off-diagonal elements are largely irrelevant due to the small magnitude values, which means these do not contribute to the scattering matrix or the fit. This is very useful information as it suggests moving forward, finding scattering matrices from measurements on specular is possible and the quicker decay in signal should not be an issue. However, one point to note, is that while the analysis performed above has demonstrated it is possible to fit a scattering matrix from specular measurements, the large range of velocities can impact the meaning of such a fit. Any scattering matrix found by fitting in such a manner is a weighted average for our velocity distribution, and so will be a less stringent benchmark for theoreticians due to their wider velocity distributions.

4.2. Diffraction Channel Measurements

The following section will present the measurements that were performed on the (0,1) diffraction channel of H-Cr(110). These were two B1 scans performed for different B2 values, currents of 0A and

0.5A (field integrals of 0 gauss metre and 55.9 gauss metre). As will be seen the results from these measurements are not as clear as for our specular measurement, due to a significantly lower signal to noise ratio, and correspondingly the results must be handled differently. The conclusions that can be drawn will be discussed before examining how reliable these conclusions are. Finally, methods to improve our results and thus the reliability of conclusions will be explored.

The scattered signal at the detector was much weaker when measuring on the diffraction channel than when measuring on specular, so significantly fewer hydrogen molecules were making it through the machine. This means that the background was a much more significant part of the signal, 99.4% on average. In fact, often during the B1 scans the measured signal for a current value was below the previous measurement of background. This would lead to negative values when subtracting the background, greatly affecting the renormalised signal. Because we were unable to subtract the background from our signal without rendering the measurement meaningless, no background correction was performed and is instead accounted for by the average background parameter in the fitting algorithm as described in section 2.4. On the other hand, drift correction was completed as previously described for the specular measurement in section 4.1. After this processing, the resulting average of our individual I_{B1} scans can be seen in Figure 4.5.

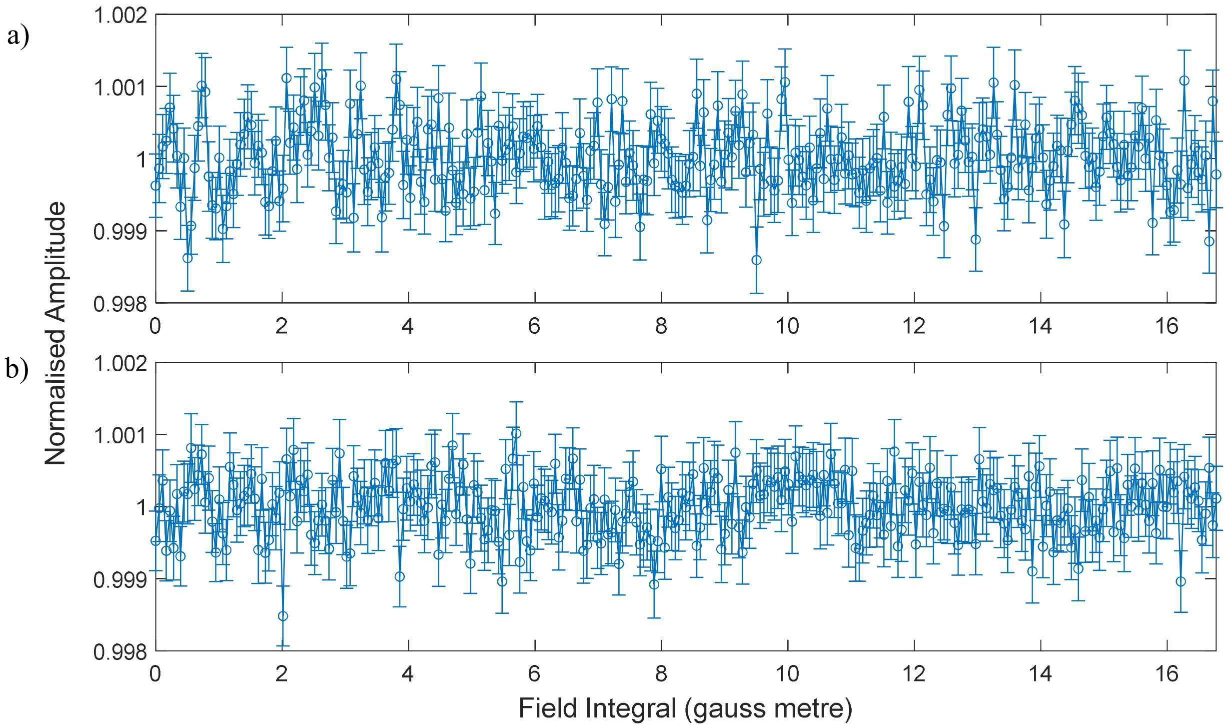

Figure 4.5: Current scans for the measurements described in section 3.3, panel a) shows the $I_{B2} = 0A$ *and panel b) shows the* $I_{B2} = 0.5A$ *measurement. From here on, the experimental measurements will be plotted with the error bars only on every five points for clarity.*

Because scattered hydrogen constitutes a much smaller proportion of the signal at the detector compared to the measurement at specular, the oscillations observed are much smaller. This becomes obvious when comparing Figures 4.3 and 4.5 for specular and diffractive scattering respectively. As a result of the smaller scattered signal, the noise is much more significant, and the measurement is much more sensitive to noise. Therefore, despite completing more individual current scans, 325 and 377 for the diffraction measurements at the two different values of I_{B2} compared to 20 scans for the specular measurement, the relative errors of the averaged value measured in the diffraction measurement are larger than those of the specular measurement. Calculating the errors as when using equation 4.1, the errors relative to the range of the measurements were 17.8% and 4% for the diffraction and specular measurements respectively. Despite this we are still able to see some oscillations in the measurement at I_{B2} = 0A, clearest in the region between 0 and 2 gauss metre in Figure 4.5a. Comparatively the oscillation magnitudes appear to be smaller in the measurement at I_{B2} = 0.5A, leading them to fall beneath the noise level. This becomes clear when we examine the Fourier transforms of the two signals, calculated using the procedure described in section 4.1, presented in Figure 4.6. In Figure 4.6a we are able to see a peak at 2430Hz/gauss which rises above the noise level for the I_{B2}=0A measurement, yet no such peak exists for the I_{B2}=0.5A measurement in Figure 4.6b.

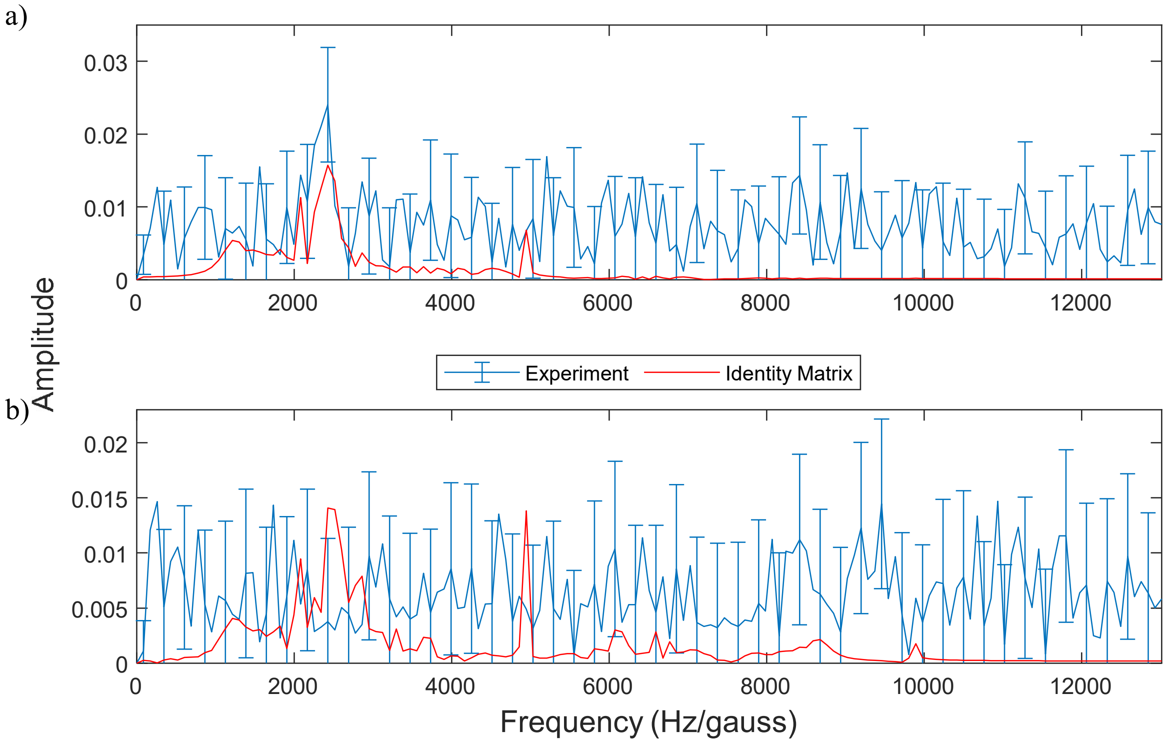

Figure 4.6: Comparison of Fourier spectrum of the experimental measurements, blue, and the simulated signals generated with an identity matrix, red, for a) $I_{B2} = 0A$ b) $I_{B2} = 0.5A$

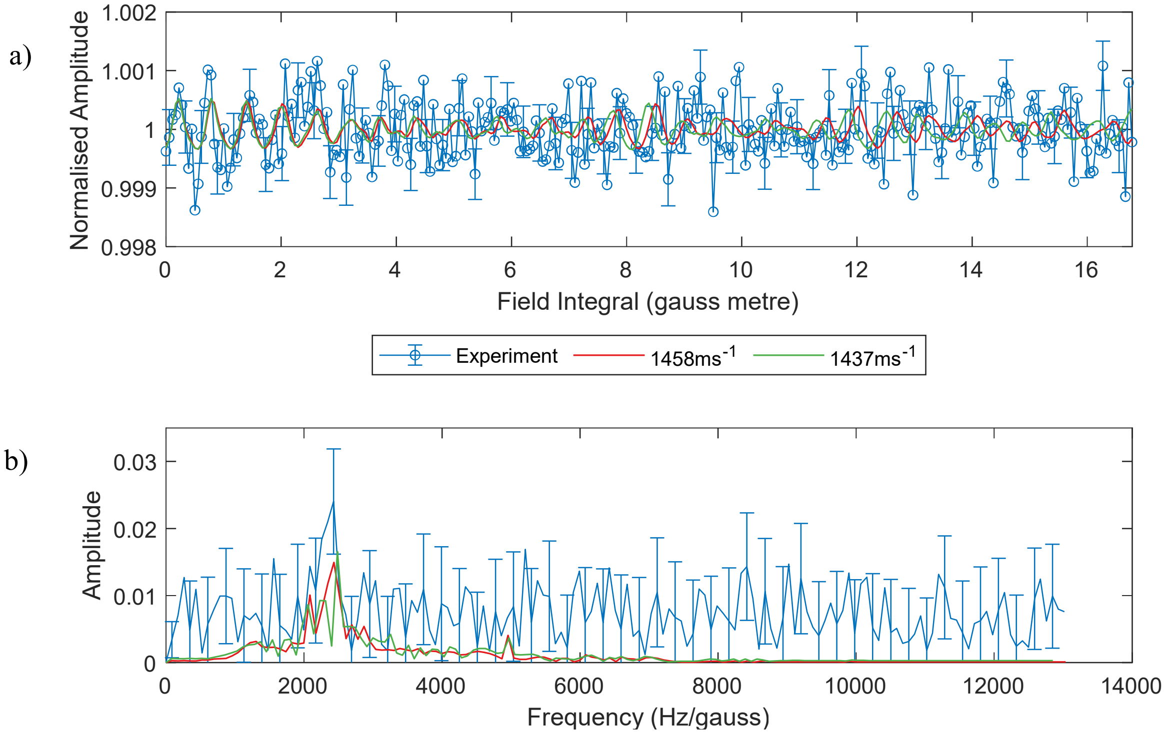

Figure 4.7: Comparison of experimentally measured signals, in blue, and signals calculated with the best fit matrix, as explained later in the text and listed in table 4.2, with a mean velocity of 1458ms^{-1}, in red, and 1437ms^{-1}, in green, in panel a) and the corresponding Fourier transforms in panel b).

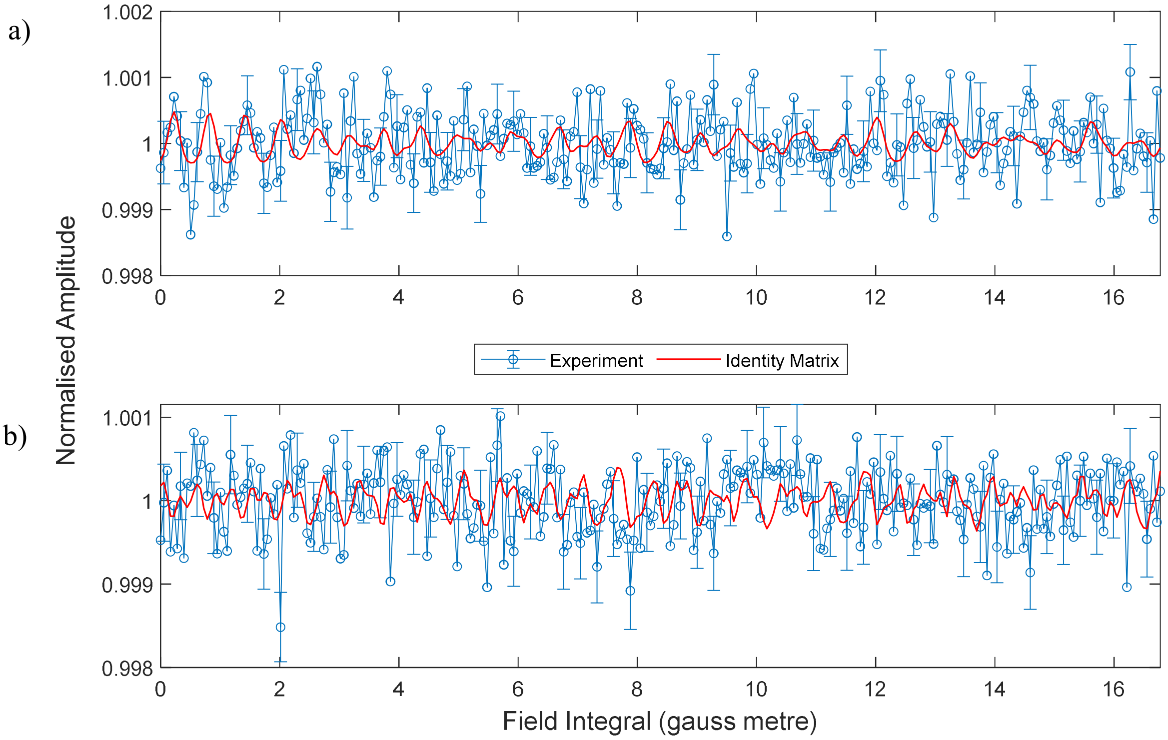

Figure 4.8: Comparison of the experimentally measured signals, in blue, and signals calculated using an identity scattering matrix with a mean velocity of 1458ms^{-1} with background added to scale the signal, in red. Panel a) is a comparison with the second solenoid supplied with a current of 0A. Panel b) is a comparison with the second solenoid supplied with a current of 0.5A

As the identity scattering matrix agreed well with our experimental measurements when scattering from specular, we first want to compare the experimental data to a signal calculated using an identity matrix to see if this remains the case and the surface continues to appear as a mirror in terms of rotational orientation.

To perform any comparisons with the measurements above, a mean velocity must be calculated given the angle of the diffraction channel. The diffraction channel that the measurement was performed at was 18.52° from specular. Given the angle between the two arms of the machine is 46.2°, the angle between the surface normal and the incidence angle of the hydrogen beam was therefore 41.62°. Using the reciprocal lattice vector magnitude calculated in section 3.2 along with equation 2.49 the velocity is calculated to be 1437ms^{-1}. However, after an initial fitting to the experimental signals, comparing the Fourier transforms of the resulting simulated signals, as was done for the specular measurement, the primary peak for the fit did not perfectly align with that of the measurement. Once again adjusting the velocity using the Fourier spectrum, the velocity was found to be 1458ms^{-1}, the comparison showing how the peak in the Fourier spectrum was not at the same point using a velocity of 1437ms^{-1} and how this affected the simulated signals can be seen in Figure 4.7. Although equation 2.49 allows us to approximate the velocity reasonably reliably, it is likely our value for incident angle was slightly off. The reason for this can be seen when looking at a gamma angle scan across specular, as seen in Figure 3.5. We can see here that our specular peak is quite broad and so hard to define accurately. Moreover, the difference in angle that corresponds to the above difference in velocity above, would only be 0.28°.

Using this new velocity estimation, we can simulate the signals for an identity scattering matrix and compare them to the experimental measurements. Figure 4.8 shows this comparison. Figure 4.6 contains a comparison of the Fourier spectrums of the experimental measurements and identity matrix signals. From sight alone we can see similarities between the simulated signal calculated using an identity scattering matrix and the measurement at I_{B2} = 0A. Figure 4.8b shows that when comparing the signals when I_{B2} = 0.5A there is no clear correlation seen between the simulated signal and noisy measurement. Furthermore, when comparing the two Fourier transforms in Figure 4.6b the simulation seems to predict a peak for a frequency between 2430 and 2516 Hz/gauss, which does not appear in the transform of the measurement, possibly because it is buried under the noise the noise level.

To test the level to which the simulated signal agrees with the experimental we can first test the number of simulated signal data points which lie within the error of the corresponding experimentally measured points. When comparing the simulated signals generated using an identity matrix, 67% of the points lie within the error bars for the measurement at I_{B2} = 0A and 68% for measurement at I_{B2} = 0.5A. This suggests that the scattering matrix does indeed agree well with our experimental data and could be a valid solution for the scattering matrix, within the current noise level. To assess the level of similarity, and latter compare it to other simulated signal, we can define the error, err, between two signals, experimental, exp, and simulated, sim, in a way which is proportional to the standard deviation of the difference between the two signals:

$$err = std(exp - sim) \cdot 1000 \qquad 4.8$$

We multiply by 1000 due to technical details required for the fitting algorithm which help it to converge. Calculating these two for our identity matrix signals gives an error of 0.463 for the measurement at I_{B2} = 0A and 0.432 for the measurement at I_{B2} = 0.5A, giving a total error of 0.895. The exact values of this error is not very important but it will be useful, as is done later in this section, for comparing different simulated signals and how well they fit the data.

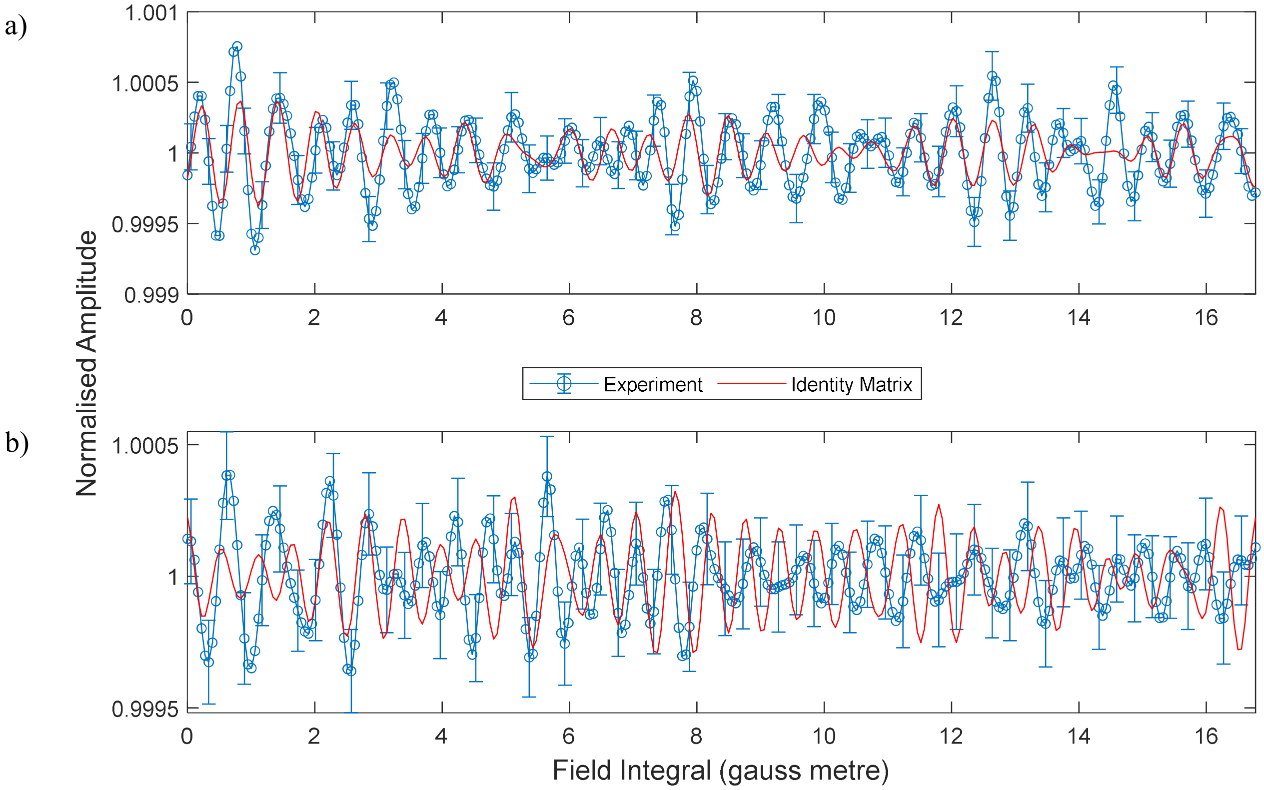

Figure 4.9: Comparison of the experimentally measured signals, in blue, and signals calculated using an identity scattering matrix, in red, with a narrow band pass filter centred on 2430 Hz/gauss with a width of 1820 Hz/gauss applied to both the experimental and simulated signals. Panel a) is a comparison with the second solenoid supplied with a current of 0A. Panel b) is a comparison with the second solenoid supplied with a current of 0.5A

Since the only peak in the experimental Fourier spectra in Figure 4.6 which appears above the noise level is around 2430 Hz/gauss for the I_{B2}=0A measurement, to test the agreement, we applied a narrow top hat band pass filter, centred at that frequency with a width of 1820 Hz/gauss to both the experimental data and simulations. This is achieved by first Fourier transforming the signal from a scan through the magnetic field to a frequency in Hz/gauss, followed by zeroing the transformed signal at all the undesired frequencies. Applying the inverse Fourier transform to the filtered spectrum results in our filtered signal. Figure 4.9 shows the effect this has on both the experimental data, blue, and the simulated signal for an identity scattering matrix, red. The error bars are considerably smaller than those in Figure 4.5 due to the narrow band pass filter used. When comparing signals filtered in this way, the frequency of the oscillation is guaranteed to agree, therefore the comparison should be made in terms of the phase of the oscillation and the modulation of the amplitudes. The signal simulated from the identity seems to match the phase quite well, for the case when $I_{B2} = 0\text{A}$ in Figure 4.9a, and there is also some resemblance in terms of the amplitude modulation with the differences mostly consistent with the estimated error bars. For the case where $I_{B2} = 0.5\text{A}$ we don't expect a good agreement as the Fourier spectra of this set of experimental data does not have a significant signal at this frequency, see Figure 4.6b. Indeed, this is confirmed when looking at Figure 4.9b as there is very little overlap between the measurements and the simulated signal using an identity scattering matrix.

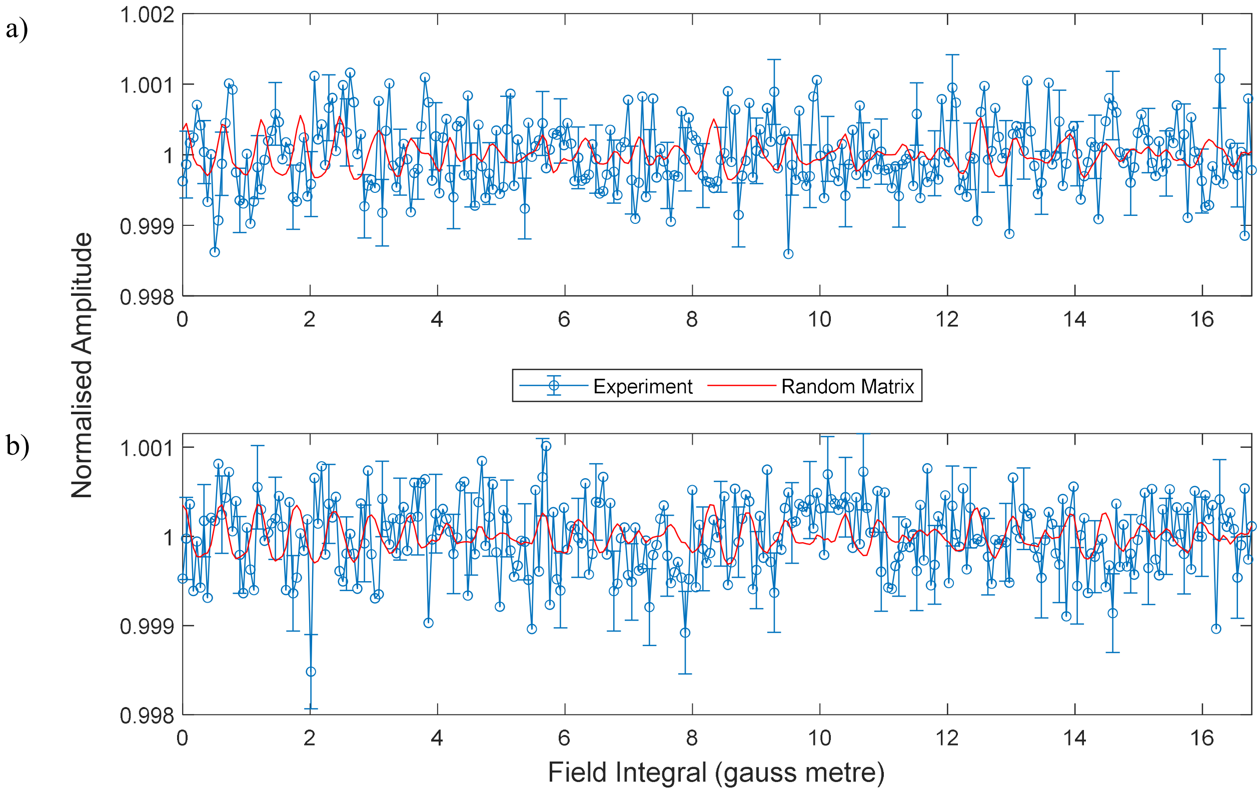

Figure 4.10: Comparison of the experimentally measured signals, in blue, and signals calculated using a random constrained scattering matrix with a mean velocity of 1458ms^{-1} with background added the same as is given by the fitting explored in the following section, in red. Panel a) is a comparison with the second solenoid supplied with a current of 0A. Panel b) is a comparison with the second solenoid supplied with a current of 0.5A

fi	11	10	$1-1$	01	00	$0-1$	-11	-10	$-1-1$
Magnitude, s_{fi}	0.792	0.036	0.679	0.960	0.849	0.960	0.679	0.036	0.792
Phase, k_{fi}	2.46	4.44	0.29	4.12	0.20	0.98	0.29	1.29	2.46

Table 4.1: Matrix elements, magnitudes and phases, in radians, for the random scattering matrix used to the calculate the signals shown in Figure 4.10.

While good agreement can be seen between the signal simulated using an identity matrix and the measured signal, for I_{B2} = 0A, especially when using a narrow band pass filter, there exists the possibility that this agreement exists purely due to the level of noise in our experimental measurements and not because the scattering matrix could actually be an identity matrix. A quick test for this is by comparing the experimental signals to simulated signals generated with a random matrix constrained as defined by equations 2.36-2.43. This comparison can be seen in Figure 4.10, and a comparison of the resulting Fourier spectra can be seen in Figure 4.11. The scattering matrix elements of this random matrix can be seen listed in Table 4.1.

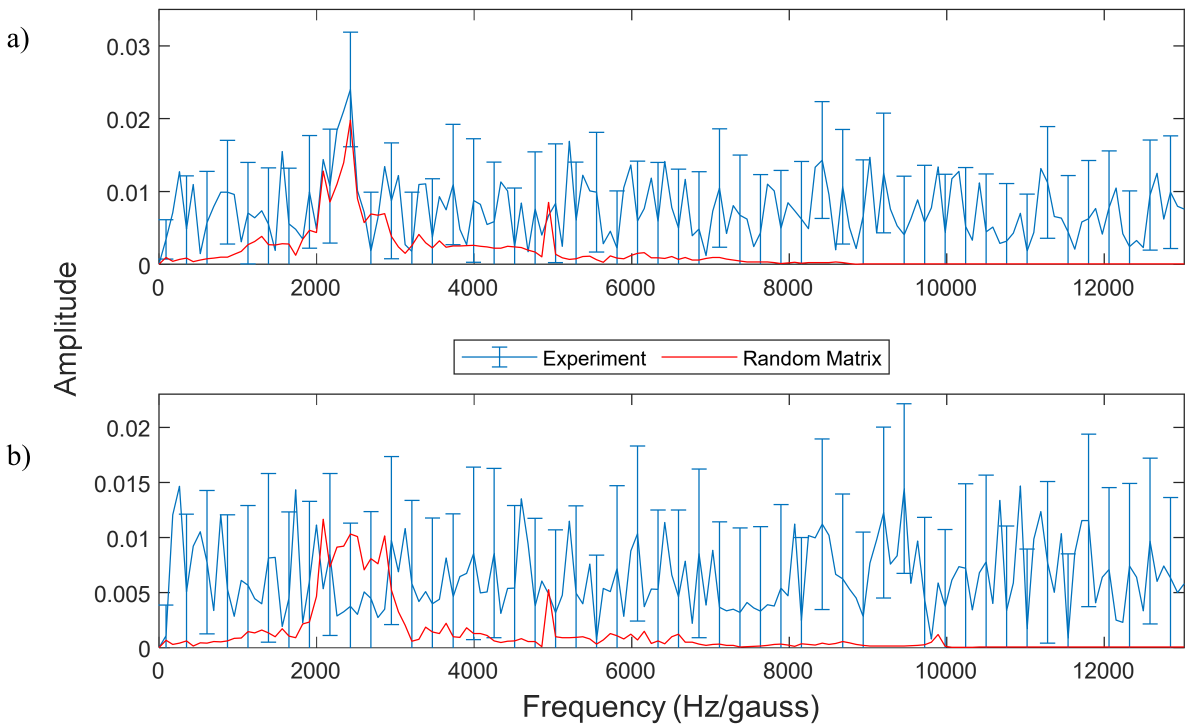

Figure 4.11: Comparison of Fourier spectrum of the experimental measurements, blue, and the simulated signals generated with a random matrix, red, for a) $I_{B2} = 0A$ b) $I_{B2} = 0.5A$

Even though the data is noisy, it seems that the phase of the first few oscillations seen in the measurement at I_{B2} = 0A do not match those of the corresponding simulated signal. Using the same measures as for the identity scattering matrix signals, we find that 58% and 70% of the points lie within the experimental error bars for the measurement at I_{B2} = 0A and I_{B2} = 0.5A respectively – suggesting that the random matrix doesn't fit the I_{B2} = 0A measurement as well as the identity matrix. Furthermore, the errors calculated give 0.537 and 0.421 for the first and second measurements respectively, for a total error of 0.958, which is somewhat larger than those calculated for the signals simulated using an identity scattering matrix.

A comparison which illustrates the misfit between the simulated signal calculated with the random matrix at I_{B2} = 0A and the experimental data at this second solenoid current value quite clearly is obtained when applying the narrow band pass frequency filter as was done for the identity matrix simulated signals. Figure 4.12 shows this comparison, and it is clear the simulated signal has a completely different phase throughout the measurement and is also different in terms of the amplitude modulation. This narrow band pass filter was selected as, when looking at the Fourier spectrum, the statistically significant peaks lay within the selected range of 1520 to 3340Hz/gauss, so the only noise was filtered out. The significance of why this peak still appears with a random matric will be discussed more in section 4.2.3.

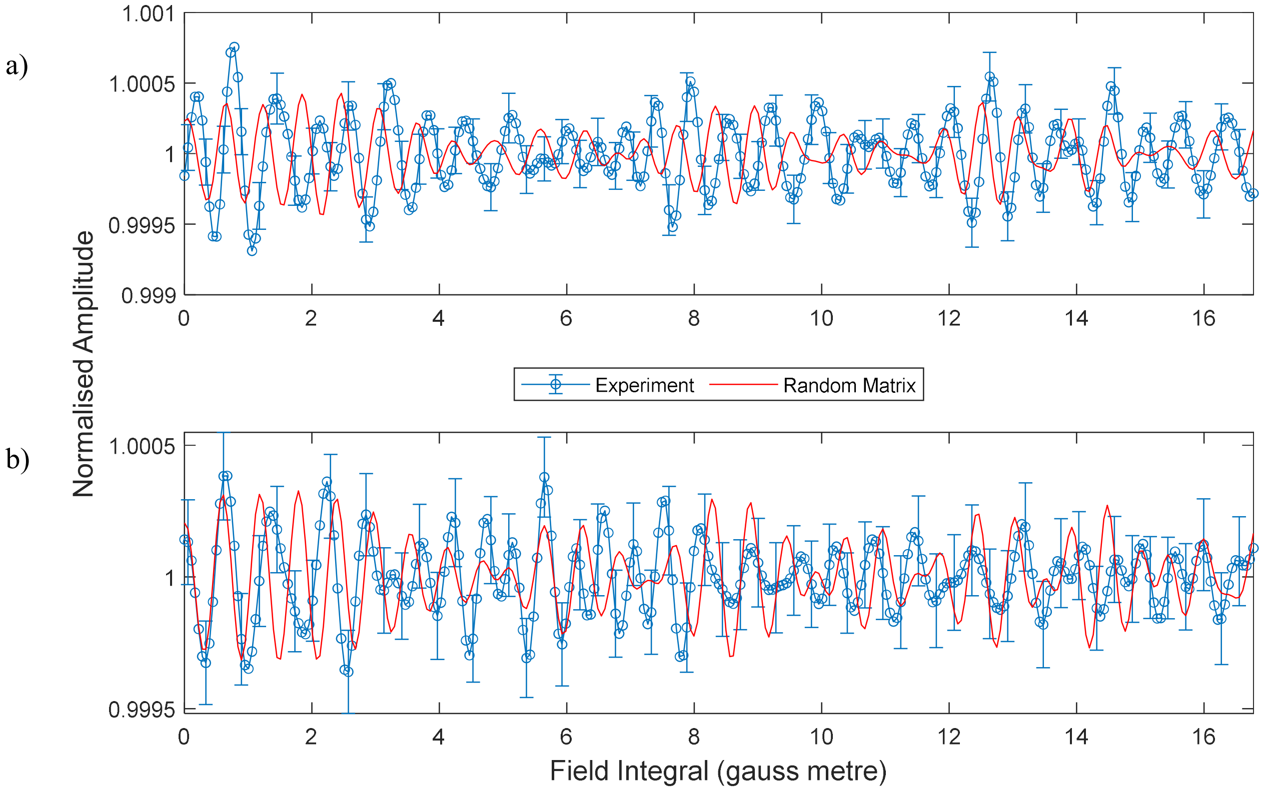

Figure 4.12: Comparison of the experimentally measured signals, in blue, and signals calculated using a random scattering matrix, in red, with a narrow band pass filter centred on 2430 Hz/gauss with a width of 1820 Hz/gauss applied to both the experimental and simulated signals. Panel a) is a comparison with the second solenoid supplied with a current of 0A. Panel b) is a comparison with the second solenoid supplied with a current of 0.5A

The results shown above demonstrates, that even before attempting to determine the scattering matrix through fitting to the signals, the experimental results can still be used to provide a benchmark for theoretical modelling of this system in the future. We can take any given scattering matrix, create a simulated signal for this matrix, test this against our experimental signals and exclude the calculations which significantly misfit the data. Providing this benchmark is quite significant, given that the signal consists of 99.4% background on average, with smaller scattered intensity than specular, as seen in Figure 3.5, and therefore the oscillations are at most 0.3% of the signal peak-to-peak.

4.2.1. Fit Results that Meet the Error Threshold

Although the benchmarking ability demonstrated above is already an important result, and we showed that the identity scattering matrix produces a signal that agrees with the measurement within the experimental noise level, this does not mean that it is the only scattering matrix that can do this, nor the one that most closely matches the measurements. Thus, extracting scattering matrix elements from a fit procedure will offer a more detailed picture, and could potentially provide information on the rotational orientation and alignment preferences of the scattering. Initially, the fitting algorithm, as outlined in section 2.4, was run 100 separate times with randomised initial variables, providing us with 100 different fit results. However, as stated in the preceding section, investigating the Fourier transforms of the simulated signals generated with the scattering matrices provided in the fit results using a mean velocity of 1437ms^{-1} showed there was a mismatch in the peaks of the resulting spectrum, lead to an improved velocity calculation of 1458ms^{-1}.

With this velocity, the signal fitting was then run 200 separate times, once again with randomised initial variables, leading to 200 different fit results consisting of scattering matrices and background values. When simulating the signal using these matrices, some of them, which had a higher fitting error, did not agree with the experimental data within the noise, (i.e., less than 2/3 of the simulated signal points lay within the error bars of the corresponding measurements). This is similar to what we saw for the signal calculated with a random scattering matrix (Figure 4.12). We have used the criteria that the simulated signals lay within two thirds of the error bars for both measurements, to select which fits should be considered as a result for the scattering matrix, 170 out of 200 fit results met this criterion. In this the section this group of 170 fit results that met the error threshold, and thus produce similar simulated signals, will be examined together to try and draw conclusions from any observed trends and similarities. The largest scattering matrix value for the best fit result was s_{11}, so for all fit results presented from here the magnitudes will be normalised to s_{11} and the phases to k_{11}. Histograms showing the values of all the fits that met this error threshold can be seen in Figure 4.13. An important note however is that 5 of the 170 fits that meet the error threshold are not displayed in the figure. They have been treated as outliers due the small number of them, where the parameter we normalise to, s_{11}, is found to be very small and as a result all other values end up being far larger ranging up to 1x10^{8}.

Looking at the magnitude histograms (Figure 4.13a), we see that even though the data is noisy the values seem to converge. The convergence is not to one well defined peak but to more complex structures characterised by two peaks or a peak with a tail. The phase histograms (Figure 4.13b) are more scattered, although a closer inspection shows that for the matrix elements which have significant magnitude, namely the k_{00}, k_{1-1} and k_{-11} values, a well-defined peak is observed. Note that the matrix elements are normalised to the 1,1 elements, s_{11} and k_{11}, making this magnitude element simply equal to one and phase element equal to zero, as well as the s_{-1-1} and k_{-1-1} values by symmetry.

It is interesting to note that one of the fit results was almost exactly an identity matrix, showing this type of solution was also found by the fitting. However, this is only 1 out of 170 results, demonstrating that better fits were provided by different scattering matrix results. Below we will further investigate the different results obtained by the fitting procedure and the stereodynamic properties they correspond to.

We can use the information provided from the fits to examine the state-to-state stereodynamic properties of the beam scattering into the diffraction channel. The probability of finding a hydrogen molecule in $m_J = f$ after scattering given an initial state before scattering of $m_J = i$, where $f, i \in 0, \pm 1$ is simply:

$$probability_{fi} = \left|\langle f|\hat{S}|i\rangle\right|^2 = \left|s_{fi}e^{ik_{fi}}\right|^2 = s_{fi}^2 \tag{4.9}$$

We start by looking at the trends in the data for the magnitude fit results, even though when looking at the histograms in Figure 4.13a exact values are not immediately clear. The first column of the histograms, which is mirrored in the third column due to the symmetry effects explained in section 2.4, represent scattering from the $m_J = 1$ state. Looking at the values for s_{-11} (left column, third panel down, Figure 4.13a) and s_{01} (left column, second panel down, Figure 4.13a), representing the two possibilities for $m_J = 1$ hydrogen to change m_J state on scattering, we can see that almost all fits gave values below 1. As such in almost all cases they are both smaller than s_{11} top left panel, Figure 4.13a). When comparing the sum of s_{-11}^2 and s_{01}^2 against s_{11}^2 for each individual fit, a large majority of the fits give the sum of the two squared magnitudes as smaller than that of the square of s_{11}. This suggests that helicopters overall prefer to remain in their rotational projection state rather than change to another. Moreover, there is a significant peak in the histogram around 0.7 for s_{-11} showing a majority of the fits predicted an appreciable amount of scattering from $m_J = 1$ to $m_J = -1$, and vice versa. In contrast, for s_{01}, almost all of the values are below 0.45 with the majority below 0.3, we can thus conclude that if a helicopter does change its rotational projection state due to scattering, the majority will not become cartwheels but will stay as helicopters, but with a reverse direction of rotation.

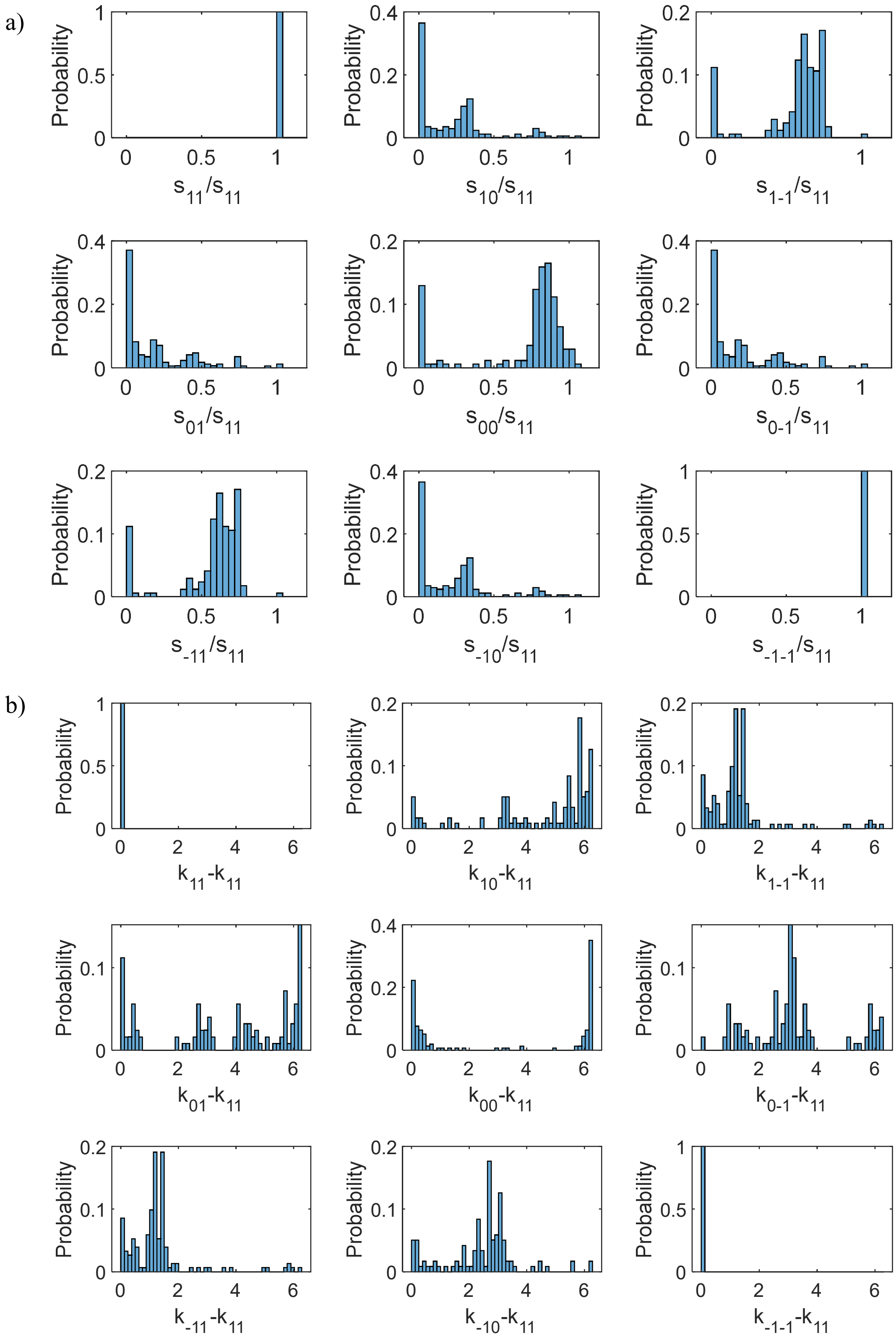

Figure 4.13:a) Histogram plots displaying all fit result values for the nine scattering matrix magnitudes for fit results that meet the error threshold, normalised by dividing by s_{11} magnitude value b) Histogram plot displaying all fit result values for the nine scattering matrix phases, in radians, for fit results that meet the error threshold, normalised by subtracting k_{11} phase value.

The second column represents all the possibilities for a hydrogen molecule approaching the surface rotating as a cartwheel. As seen for hydrogen molecules approaching the surface as helicopters, the majority of fit results predict that the highest probability occurrence for a molecule approaching as a cartwheel is to remain rotating as a cartwheel after scattering (middle column, second panel down, Figure 4.13a). Furthermore, examining the histograms for s_{10} and s_{-10} (middle column, top and bottom panel, Figure 4.13a respectively), almost all of the fit results provided values below 0.45, demonstrating that probability of a cartwheel scattering to a helicopter state is relatively small compared to remaining in the same rotational projection state.

The values provided for the phases, seen in Figure 4.13b, do not provide physical information about the system, as the magnitudes do. However, they are still as important as the magnitudes for benchmarking when simulating the system theoretically, since the signal is an interference of different terms, and both are required to mimic the experiment. An important note here is that the phase values corresponding to a very small magnitude value, below 0.005, have been removed from the histograms as these are essentially a random number as they do not contribute to the signal. This will be done for all results presented through the rest of the thesis. The picture provided by the phase histograms is slightly more muddled than that of the magnitude histograms, however there are still some observations which can be made. The first of these is that the $m_J = 0$ to $m_J = 0$ scattering (middle column, middle panel, Figure 4.13b) is mostly in phase with the $m_J = 1$ to $m_J = 1$ scattering (left column, top panel, Figure 4.13b), and thus also with the $m_J = -1$ to $m_J = -1$ scattering (right column, bottom panel, Figure 4.13b) by symmetry. Secondly the most populated bins for k_{01} and k_{0-1} (middle panels in left and right column, Figure 4.13b, respectively) appear to be in phase and π out of phase with k_{11} (top left panel, Figure 4.13b) respectively.

To try and draw some more concrete conclusions from our data, and further understand the shape of the histograms in Figure 4.13a, we can check whether there are correlations between the magnitude values of different matrix elements from all the fits that meet the error threshold. Figure 4.14 displays a matrix of scatter plots. Each of the x axes and y axes represent one of four magnitude values, s_{10}, s_{1-1}, s_{01} and s_{00}. These are chosen as the rest of the magnitude values are mirrors of these or are the value we normalised to (s_{11}). Each point on the scatter plots represents two of these values for a given fit to investigate if there are correlations between them. The histograms for each of the magnitude values are shown (above and to the right of the scatter plot matrix) to assist the comparison with the histogram data show in Figure 4.13a.

We start by noting that the broad peak at approximately 0.7 in the histogram of s_{1-1} includes two maxima, one at 0.75 and one between 0.5 to 0.65. We can examine how these two cases correlate with the values obtained for s_{10} by looking at the scatter graph for s_{1-1} and s_{10} (upper row of scatter plots, second from left in Figure 4.14). The peak in the histogram of s_{1-1} seen at around 0.75 corresponds mainly to values of s_{10} close to zero, one such point is highlighted green in the plot, and does not correspond to the secondary peak of s_{10} around 0.35. Conversely most of the s_{1-1} values contributing to this peak are between 0.5 and 0.65, seen in the cluster surrounding the red point, with fewer results in this range corresponding to very small values for s_{10}. Examining these two cases separately, we can discuss the two of the most likely possibilities for scattering. In the first case s_{1-1} is centred around 0.75 giving a 56% probability, $({s_{1-1}}^2/{s_{11}}^2)$, for a helicopter reversing its rotation direction after scattering relative to the probability of remaining in the same rotational projection state. In this case the probability of scattering from a cartwheel to a helicopter $({s_{10}}^2/{s_{11}}^2)$ is very low, with almost all values below 0.2. Conversely for lower probabilities of the $m_J = -1$ to $m_J = 1$ transition (s_{1-1} in the range 0.5 to 0.65 or relative probabilities of 25% to 42%), the probability of $m_J = 0$ to $m_J = 1$ scattering is then larger, centred on $s_{10} = 0.35$, i.e. giving an appreciable 12% probability $({s_{10}}^2/{s_{11}}^2)$ for this type of transition.

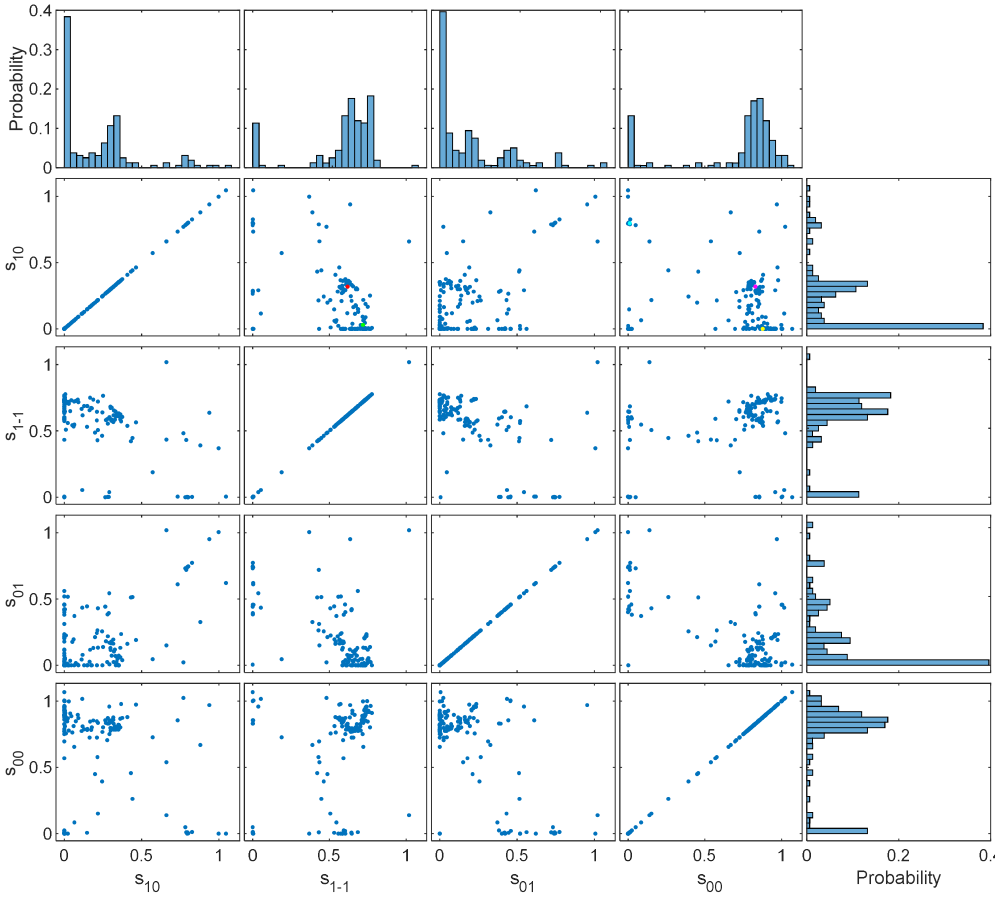

Figure 4.14: Scatter plots representing the grouping of different fit result scattering matrix magnitudes. Each point on the scatter plots represents the value of two scattering matrix magnitudes for a single fit result. On the outside edges histogram distributions are given for the individual scattering matrix magnitudes across all of the fit results that meet the error threshold, as seen in Figure 4.13a. Select points are highlighted.

Another example for correlations between different matrix elements can be seen when looking at the peak of s_{10} at 0.35 in comparison to the values of s_{00} (upper row of scatter plots, forth column from left in Figure 4.14). The histogram of s_{00} has two main peaks, one in the region of 0.8 and one in the lowest bin. Looking at the scatter plot here we can see that none of the results in the lowest bin for s_{00} correspond to values of s_{10} in the 0.35 peak we discussed earlier, instead they correlate with either high values of s_{10} (approx. 0.8, such as the point highlighted in cyan) or very low values close to zero. Examination of the fit results found that when the s_{00} result had a small value all but two of the fit results for s_{01} had values larger than 0.35. In contrast, most of the larger results for s_{00} found smaller values of s_{01} below 0.35, such as the points highlighted in purple and yellow. Therefore, we can conclude that fit results which predict small probabilities for a cartwheel remaining rotating as a cartwheel is decreased, also predict a higher probability of helicopter molecules transitioning to cartwheel molecules after scattering.

It is important to note that the various correlations mentioned above, do not necessarily represent correlations between the stereodynamic properties themselves, instead they represent correlations between all of the fits that have been considered as acceptable fits to the data, meaning the simulated signals fall within 67% of the error bars and are reasonably similar, and explain why we get multiple peaks in the histogram for each of the values.

4.2.1.1. Integration Over Initial and Final States

As we discussed above, the histograms of the scattering matrix elements generate from the various fitting attempts have more than one clear maximum, leading to some ambiguity about what the actual scattering matrix values are. One way to address this is to focus on the fit which produces the smallest error as will be discussed in further detail in the next subsection. Another way is to look at more averaged stereodynamic properties instead of the individual state to state transition probabilities.

Looking at equation 4.9 that relates the scattering matrix elements to the probabilities, we can see the sums of the squares of the magnitudes in the column of our scattering matrix, give us the probability of a particular m_J to scatter into the diffraction channel, regardless of its final state. Similarly summing across the rows of the magnitudes squared gives us the probability of finding a particular m_J' in the diffraction channel after scattering regardless of the state before scattering.

By finding the sums of the magnitudes squared down the columns individually for each of the fit results that meet the error threshold, we can see if and to what extent the different fit result scattering matrices converge on a value for the proportion of each rotational projection state which scatters into the (0,1) diffraction channel. Figure 4.15 displays a histogram of the square of the ratio of $m_J = 0$ initial states to $m_J = 1$ initial states, i.e., the ratio between the population of cartwheels to helicopter states for each fit result that met the error threshold. As can be seen in the histogram almost all the relative populations are below 1, meaning that each of the two helicopter states is more likely to scatter into the (0,1) diffraction channel than the cartwheel state.

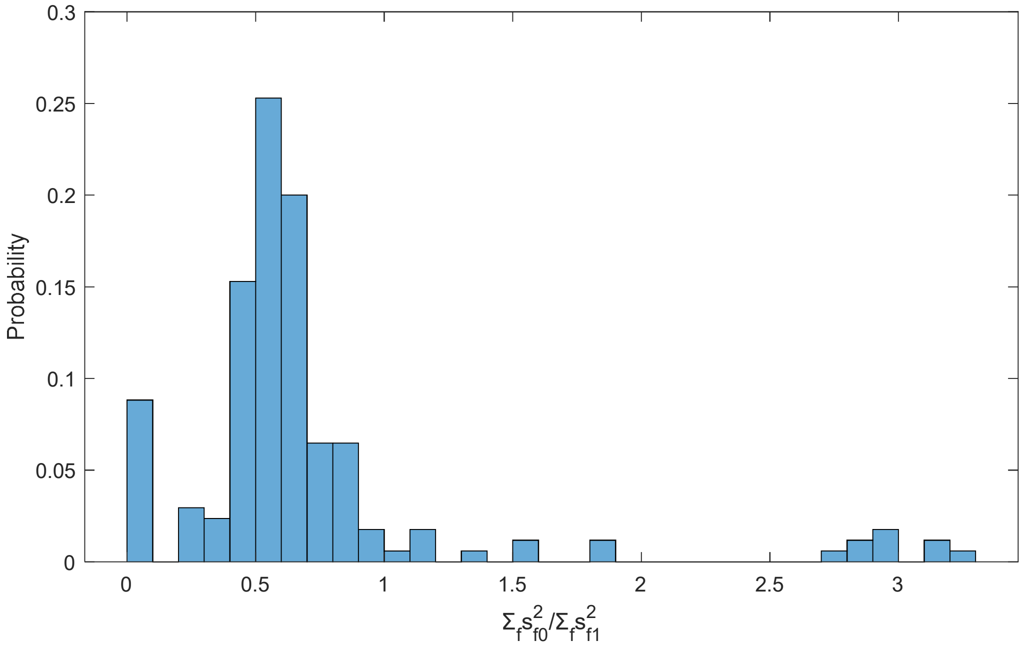

Figure 4.15: Histogram of the sum of the squared magnitudes of the second column over the sum of the squared magnitudes of the first column of the scattering matrix, giving the ratio of $m_J = 0$ *to* $m_J = 1$ *before the collision, for each individual fit result that met the error threshold.*

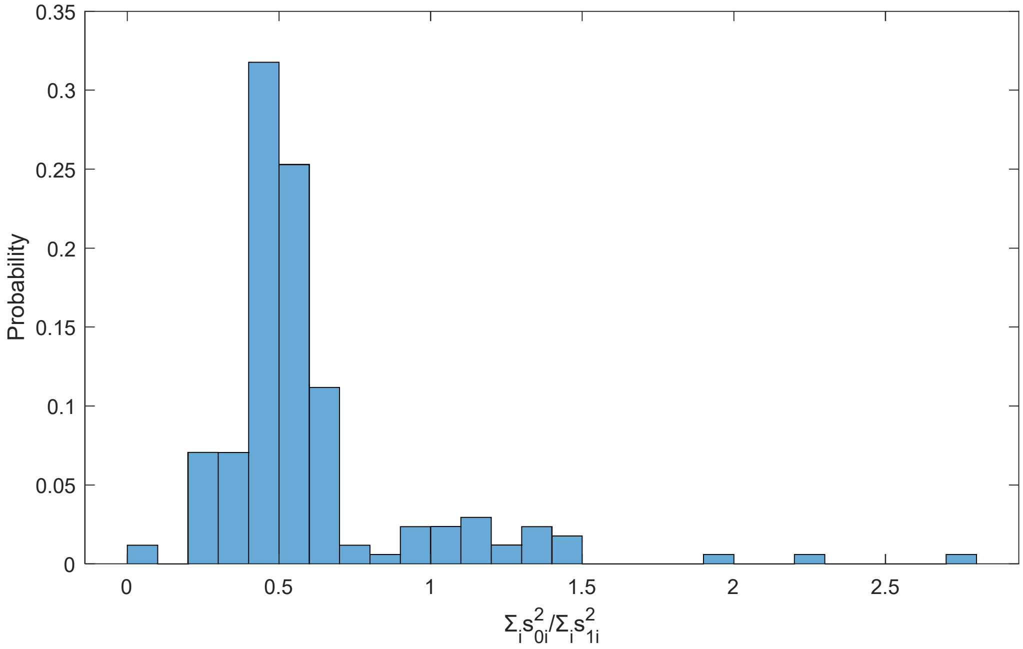

Figure 4.16: Histogram of the sum of the squared magnitudes of the second row over the sum of the squared magnitudes of the first row of the scattering matrix, giving the ration of $m_J = 0$ *to* $m_J = 1$ *after the collision, for each individual fit result that met the error threshold.*

Similar methods can be applied to determine if our surface polarises the incoming beam, i.e., if the proportion of cartwheels or helicopters increases or decreases due to scattering from the surface. Summing across the rows of the scattering matrix gives us the probabilities of a given rotational projection state after the collision, regardless of the initial state. A histogram of the ratio of $m_J = 0$ to $m_J = 1$ probabilities after scattering from the surface can be seen in Figure 4.16. Since almost all of the fits give results where the sum of the square magnitudes of the cartwheel row is less than that for either of the helicopter rows, this suggests that the H-Cr(110) surface polarises a hydrogen beam when scattering from the (1,0) diffraction peak, and an initially unpolarised beam scattering into the diffraction channel will have a larger proportion of helicopters relative to cartwheels after scattering.

4.2.1.2. Best Fit Results

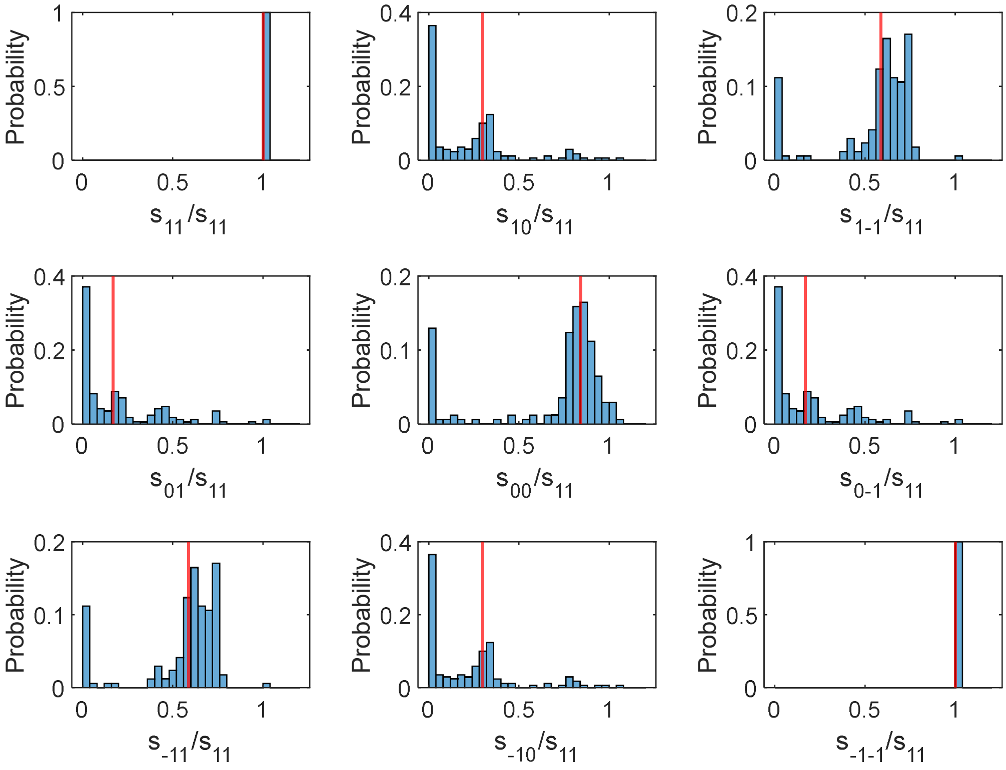

Figure 4.17: Histogram plot displaying all fit result values for the nine scattering matrix magnitudes for fit results that meet the error threshold, with the value of the best fit labelled by a red line.

While the fit procedure returns various values for the state-to-state transitions, we can focus on the particular set of values which produces the best overall fit (smallest error when comparing to both experimental data sets), hoping that it's superior fit makes it more reflective of the actual scattering event. The magnitude values for the best fit can be seen drawn on the histograms as vertical red line in Figure 4.17 and listed numerically in Table 4.2. Figure 4.18 shows the comparison of signal generated by the best fit data results, in red, to the experimental data, in blue, as well as the simulated signals generated using an identity scattering matrix, in green. Looking at the I_{B2}=0A data we can see that the best fit signal produces a signal which is very similar to that produced by the identity scattering matrix. Figure 4.19 performs the same comparison of signals, with the narrow band pass filter as applied in section 4.2. This illustrates that both the best fit result and the identity matrix results fit the data quite well, in contrast to the signal calculated using the random matrix which completely misses out on the phase (Figure 4.10).

	s_{11}/s_{11}	s_{10}/s_{11}	s_{1-1}/s_{11}	s_{01}/s_{11}	s_{00}/s_{11}	s_{0-1}/s_{11}	s_{-11}/s_{11}	s_{-10}/s_{11}	s_{-1-1}/s_{11}
Best fit value	1	0.300	0.589	0.169	0.844	0.169	0.589	0.300	1
s_{fi}^2	1	0.090	0.347	0.028	0.712	0.028	0.347	0.090	1

Table 4.2: Best fit scattering matrix magnitude values and their square values.

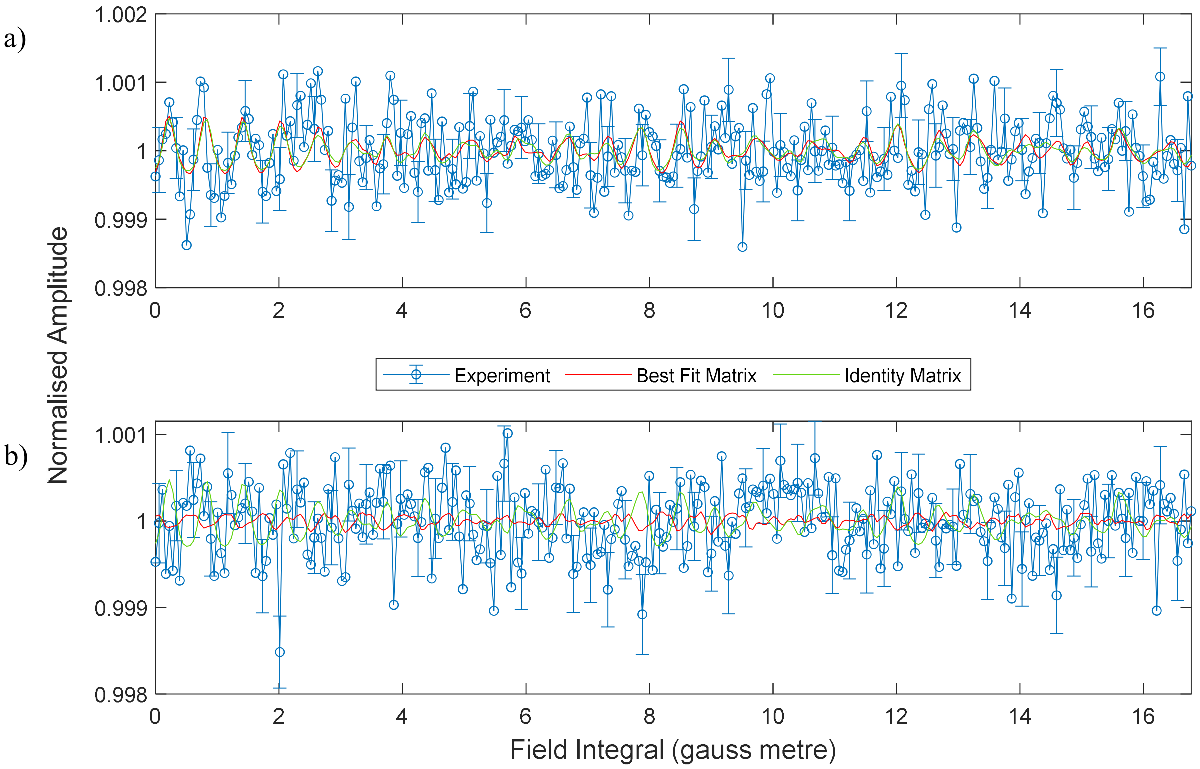

Figure 4.18: Comparison of the experimentally measured diffraction signals, in blue, signals calculated using the best fit to the data, in red, and signals calculated using an identity matrix, in green. Panel a) is a comparison with the second solenoid supplied with a current of 0A. Panel b) is a comparison with the second solenoid supplied with a current of 0.5A

Looking at the narrow band filtered measurements of the I_{B2}=0.5A data, the best fit results and the unity scattering matrix results differ significantly, but neither one of them matches the measurements (which is not that surprising, given the I_{B2}=0.5A measurements do not have a substantial component at the frequency the filter was centred around). What we can see, is that the best fit signal has a smaller oscillation magnitude which reduces the deviation from the measured data in comparison to the identity scattering signal. Using the error function defined above, the best fit result produces errors, calculated using equation 4.8, of 0.458 and 0.409 for the 0 and 0.5A signals respectively, and a total error of 0.867.

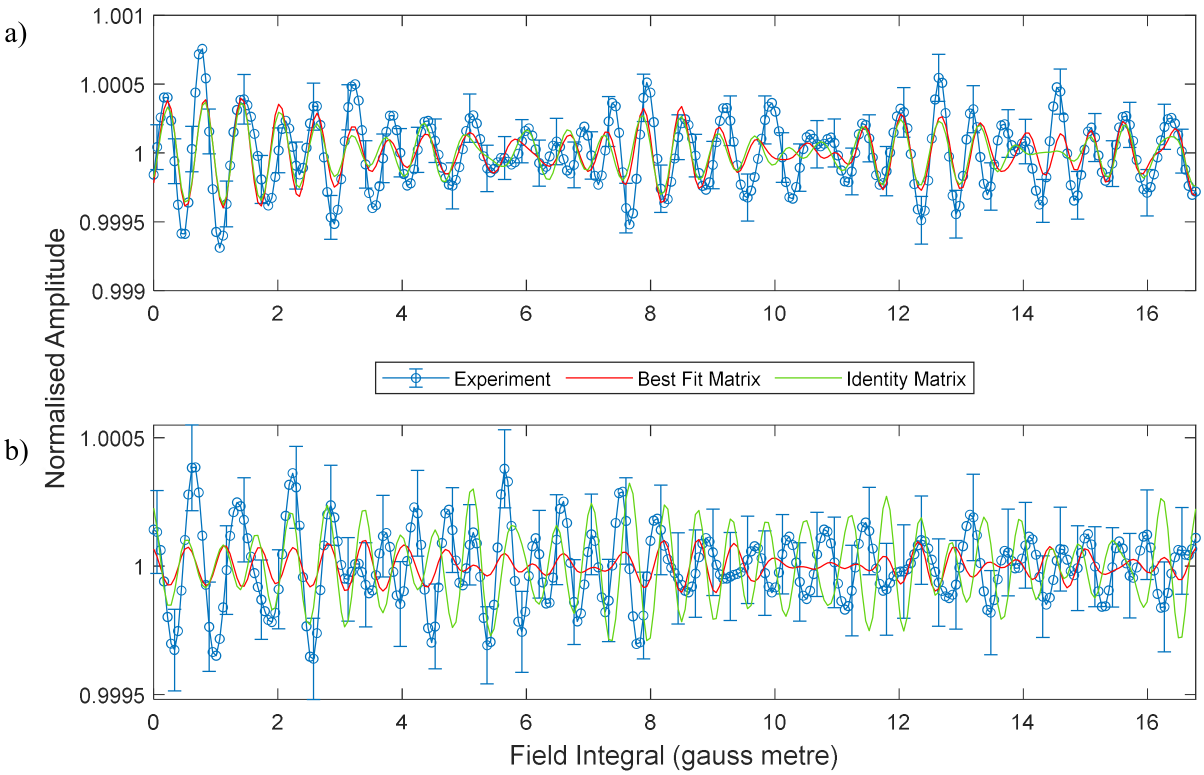

Figure 4.19: Comparison of the experimentally measured signals, in blue, signal calculated with the best fit to the data, in red, and signals calculated using an identity matrix, in green, with a narrow band pass filter centred on 2430 Hz/gauss with a width of 1820 Hz/gauss applied to both the experimental and simulated signals. Panel a) is a comparison with the second solenoid supplied with a current of 0A. Panel b) is a comparison with the second solenoid supplied with a current of 0.5A

We will investigate the reliability of these results in the following section, but first we will draw the conclusions we are able to from them. As explained above, summing over the squared values of the columns provides us with information about the amount of the rotational projection states scattering into the diffraction channel. Agreeing with what we previously found for the entire set of fit results, for the best fit cartwheels are less likely to scatter into the diffraction channel than helicopters, which in this case are over 1.5 times more likely. Similarly summing over the columns show us that a higher proportion of helicopters will be found in the beam after scattering, demonstrating the polarising properties of the surface.

If we divide each of the probabilities by the sum of the column they are found in, it will inform us of the probability of a given rotational projection state scattering to another. For $m_J = 1$ this gives a 72.7% probability of remaining in $m_J = 1$, a 2.1% chance of scattering to $m_J = 0$ and finally a 25.2% probability of being found in the $m_J = -1$ state after scattering. A hydrogen molecule approaching as a cartwheel then has a probability of 79.8% if remaining as a cartwheel, with a 10.1% chance of scattering into either of the helicopter states.

From these probabilities we can see that, a hydrogen molecule approaching the surface rotating as a helicopter is slightly less likely to remain in its rotational projection state than one that approaches as a cartwheel. Moreover, in keeping with the general trends observed above, a hydrogen rotating as a helicopter only has a small chance to scatter from the surface as a cartwheel and is much more likely to just have the reverse direction of rotation if its m_J does change. The best fit value for s_{10} (middle column, top row Figure 4.17) is inside the secondary peak seen around 0.35 and so falls into the second grouping explored in the previous section. Therefore, there is an appreciable amount of scattering involving a hydrogen approaching as a cartwheel and leaving as helicopter, although remaining in $m_J = 0$ is still much more likely.

The best 10 fits to our data also all give very similar fit results to the best fit results. Therefore, although we have observed a variety of fit results that meet the error threshold of 67% of points lying within the experimental error bars, such as the identity scattering matrix explored previously, it is worthwhile to explore the significance of the total error in regard to placing more importance on the best fit results. This is also important in regard to our consideration of the identity scattering matrix result, which had a larger error than these best fit matrices.

4.2.2. Noise Fitting Analysis

The following section will investigate the extent to which we would expect the fitting result to converge on a common result with the amount of noise and background that are in our measurements, and how accurate these results, along with their best fit, would be in comparison with the true value. This will also give an indication if more weight should be placed on the fit results with the smallest error in comparison to the experimental results. This has been done by using different scattering matrices to simulate signals whilst adding similar noise and background as to what was measured in the experiment. The noise was added with the same method as described for the simulated identity matrix in section 4.1.1. To add the background, as described in section 2.4, the fitting code provides us with a parameter for the background. Therefore, this parameter was taken from the best fit and applied to the simulated signals that will be discussed in this and following sections. Then by fitting to these simulated signals, we can test how accurate the fitting results are by comparing them to the original input values. An example of the fit results for a simulated signal with 17.5% noise over the range added can be seen in Figure 4.20. On the histograms there are lines representing the original scattering matrix values (red) and those found by the best fit (blue). The scattering matrix used to produce the simulated signals that were fit to was selected as the one produced by the best fit to the experimental data, which is given in Table 4.2. This was done to also test if we would expect to get the same result if our best fit was close to the actual scattering matrix.

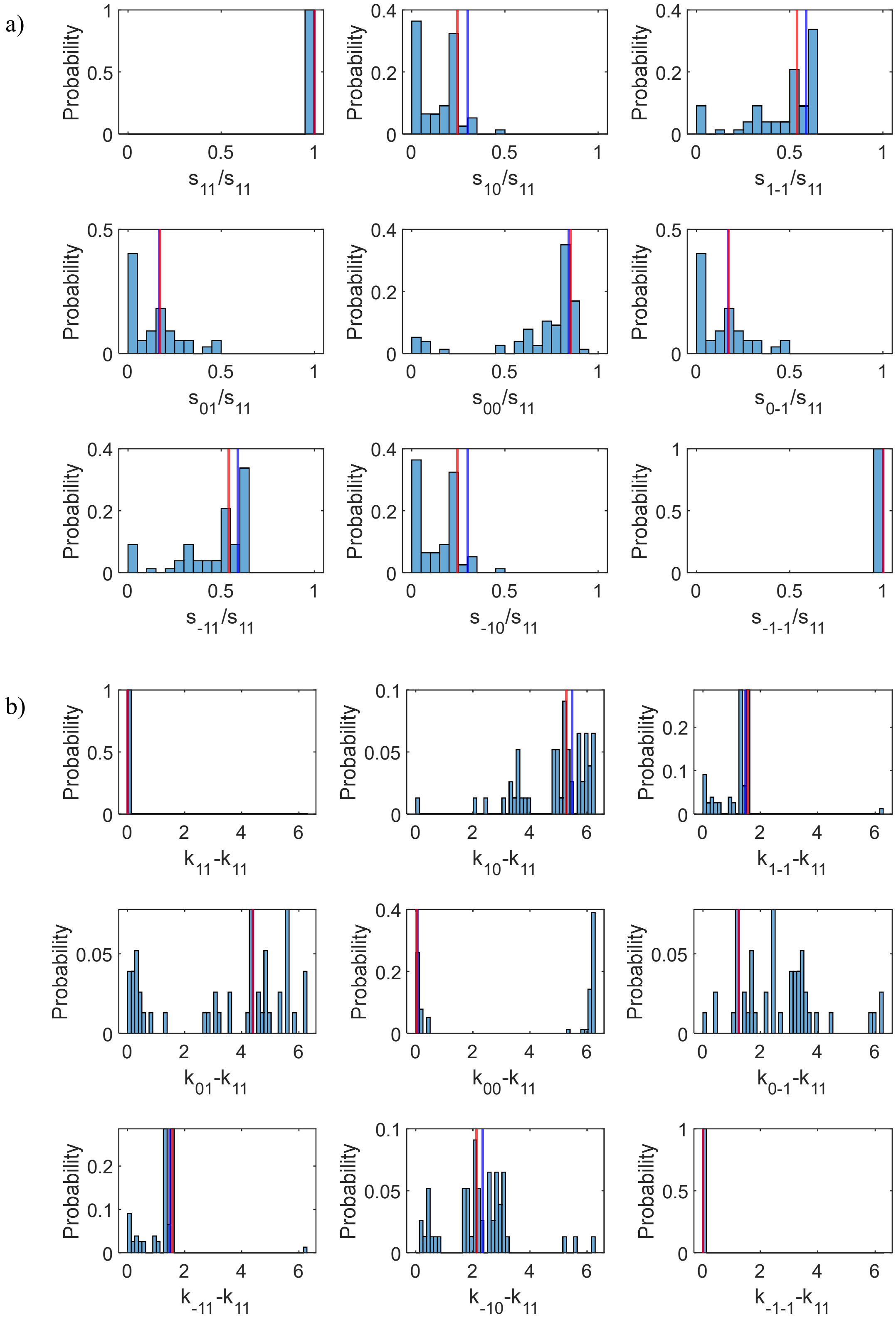

Figure 4.20: Histograms of one of the fit result magnitudes, in panel a), and phases, in panel b), for fitting to two simulated signals with 17.5% noise added. The values of the best fit and original value used to simulate the signals are marked by blue and red lines respectively.

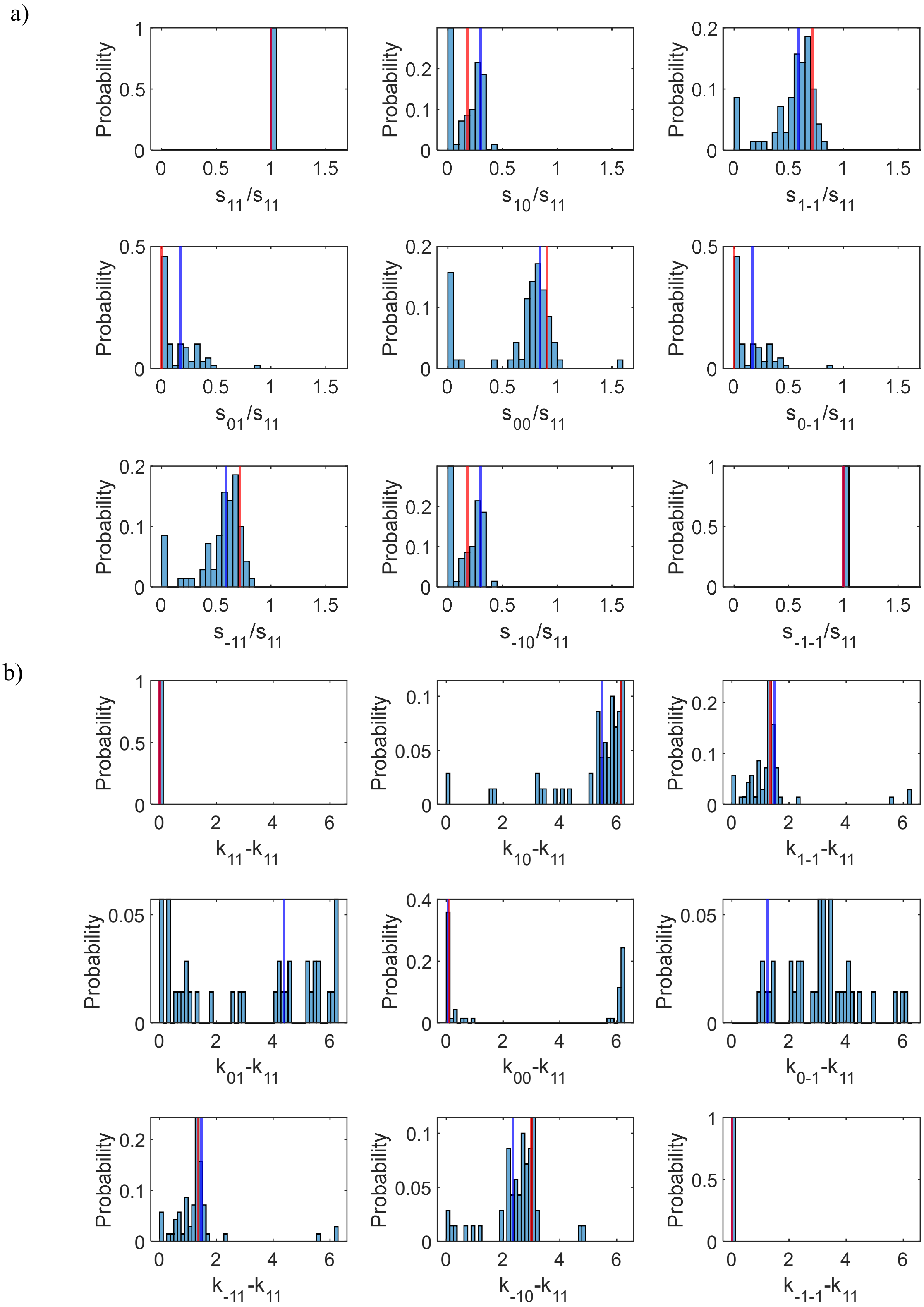

Figure 4.21: Histograms of the fit result magnitudes, in panel a), and phases, in panel b), for fitting to two simulated signals where random 17.5% noise added is added to the signals before each fit. The values of the best fit and original value used to simulate the signals are marked by blue and red lines respectively.

The first method investigated to determine if the results displayed in Figure 4.20 are reproducible was to create two new signals (I_{B2}=0 and I_{B2}=0.5A) based on the same initial simulated signals, but with 100 different random noise patterns, instead of fitting to the same two signals 100 times, as was done above. Using the same scattering matrix as for Figure 4.20, the results of this can be seen in the histograms displayed in Figure 4.21, once again only including those that meet the error threshold. From this figure, we can once again observe a similar spread in fitting result values, with more populated bins around zero despite the actual parameters being larger. Furthermore, it is also encouraging that the best fit results once again do not have a difference larger than 0.2 for the magnitudes compared to the original value.

From the figure it can be seen that the best fit to the simulated signal seems to be quite close to the true values, despite there being a similar spread in the fit results as was seen in our experimental fitting. The largest error in the magnitudes was 0.054 and 0.215 for the phases. However, although this result is encouraging, it could simply be the result of a favourable combination of the scattering matrix and noise, and not be widely reproducible.

Figures 4.19 and 4.20 indicated that the best fit generally seems to agree well with the original scattering matrix component values and seem to be closer to these values than the general fit results which meet the error threshold. Although this is a good test, it is possible that these results are simply due to the specific scattering matrix used. Therefore, to counteract this and more accurately represent what was done experimentally the process of generating two noisy signals was repeated four times for 5 different matrices adding 3 different levels of noise for each and then fitting 100 times to each of the pairs of signals. Displaying the histograms for all of these simulations would not be informative, so here we have taken the standard deviation of the results that meet the error threshold and the number of fits that were within one bin widths either side of the best fit (best fit height).

As we are testing to see how accurate our best fit results are, the above listed variables are plotted against the difference between the best fit and true scattering matrix values (best fit error), to see if there are any relationships on the limits in the best fit error. These plots can be seen in Figures 4.21 and 4.22. Each point in the plots represents a fit result for a single scattering matrix value to a simulated signal with noise added; the different markers represent different scattering matrices used to generate the simulated signal, and the different colours represent the fraction of noise added. One of the scattering matrices used to create the simulated signals contained a magnitude that was essentially zero and as such scatter plot points from the corresponding phase value have not been included as the best fit error varied completely randomly due the nature of the magnitude. First looking at the best fit height against the best fit error, in Figure 4.22 there appears to be an inverse relationship between the two, although a number of points do not follow this trend. The inverse relationship leads to all points seemingly contained within a lower triangle of the plot, and we can see that while results with low best fit height can be obtained for a wide range of best fit errors, these errors are gradually reduced for larger values of best fit height. Therefore, we may be able to use this to estimate the error in our best fit.

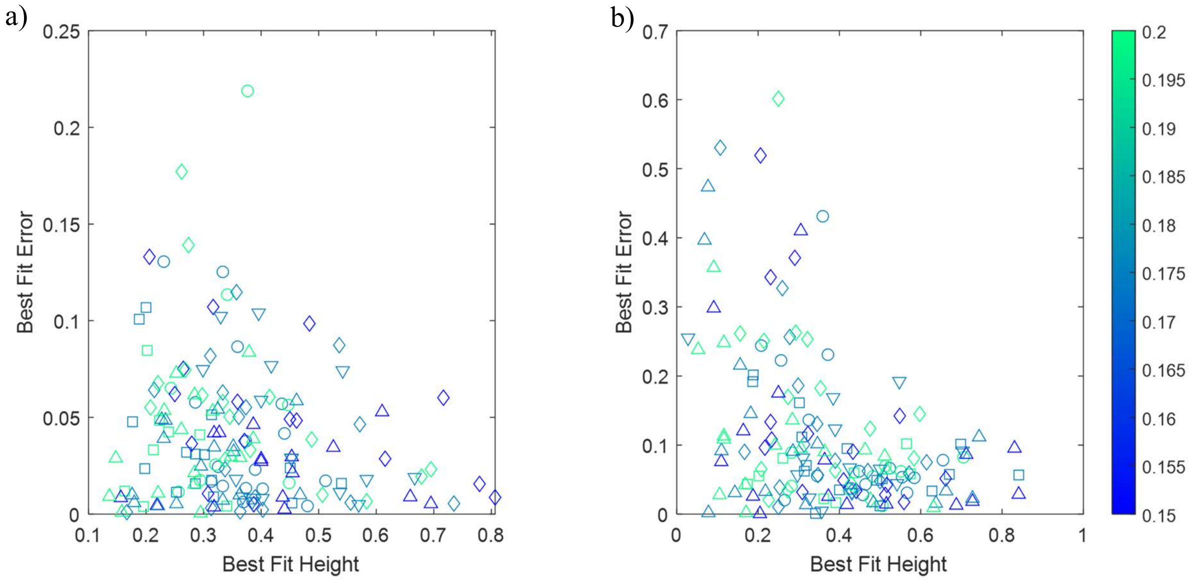

Figure 4.22: Scatter plot of the best fit height against the best fit error for a large number of simulated signals as described in the text. Panel a) displays this for the magnitude values and panel b) the phase values. Here we define the best fit height as the fraction of fits that meet the error threshold which are within 0.04 and $\pi/25$ *of the best fit values. And the best fit error is defined as the abs(best fit value – original value). Each point is for a single scattering matrix parameter,* s_{fi} *and* k_{fi}. *Here the values that are used for normalisation to or are just mirrors or phase shifted values as defined by equations 2.36 to 2.43 are not shown. The different markers indicate different scattering matrices used to generate the simulated signals, and the colour indicates the amount of noise added as a fraction of the range of the signal.*

Now looking at Figure 4.23, plotting the standard deviation of the fit results against the error of the best fit value against the true value. Here we are trying to investigate the relationship between the spread of the data and our best fit error. Although there does seem to be a positive correlation, it is not strong enough to make any predictions about the accuracy of our results. It is interesting to note however, as seen to some extent in Figures 4.21 and 4.22, that the data with more noise added generally appears to be more spread out, suggesting that it could just be a matter of iterating the fitting algorithm more times to converge more on a value.

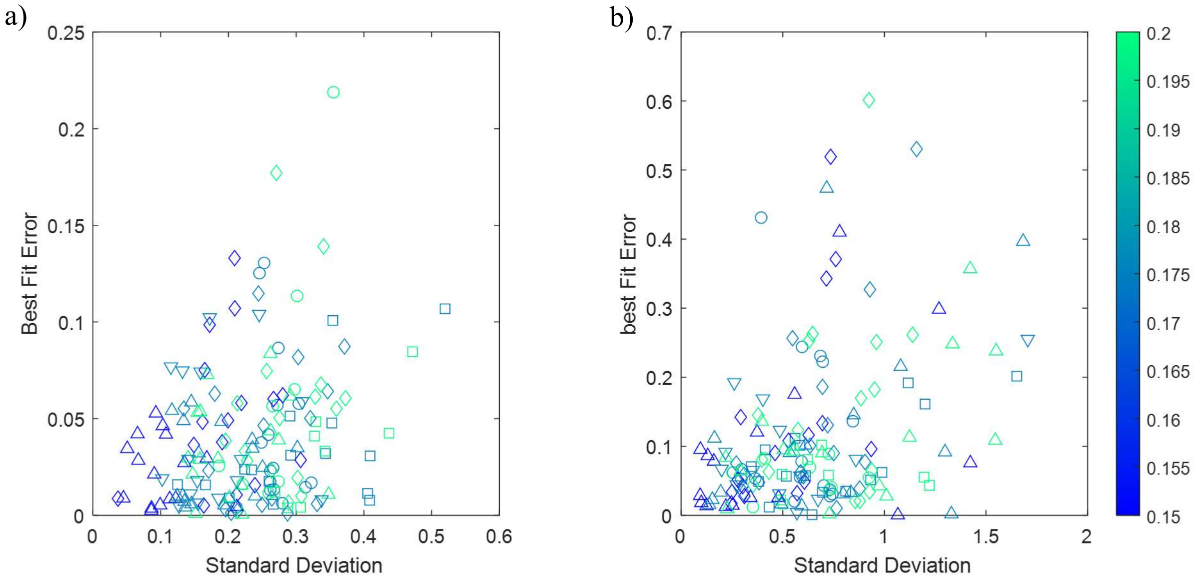

Figure 4.23: Scatter plot plotting the standard deviation against the best fit error for a large number of simulated signals as described in the text. Panel a) displays this for the magnitude values and panel b) the phase values. Here we define the standard deviation as standard deviation of the fits that meet the error threshold which fall within the most populated bin.

	s_{10}/s_{11}	s_{1-1}/s_{11}	s_{01}/s_{11}	s_{00}/s_{11}	$k_{10}-k_{11}$	$k_{1-1}-k_{11}$	$k_{01}-k_{11}$	$k_{00}-k_{11}$
Standard Deviation	0.245	0.231	0.235	0.330	1.456	1.006	1.604	0.797
Best Fit Height	0.100	0.135	0.076	0.159	0.100	0.194	0.047	0.224

Table 4.3: Standard deviations and modal heights of different scattering parameters provided by the experimental fits, here values that are normalised to or are just mirrors or phase shifted values as defined by equations 2.36 to 2.43 are not shown.

Table 4.3 shows the values for the best fit height and standard deviation of the fit results obtained from fitting the experimental data. Examining the results in Figure 4.22 demonstrates that low values of best fit height, below 0.15, do not allow for predicting the best fit error as there are no data points for these values. Moreover, there are a wider range of values for the best fit error at lower values, although it could be possible to provide an estimation of the maximum possible error between the best fit result and the true value. Contrastingly, as shown in Figure 4.23, the standard deviation provides a better estimation of error at lower values, and provides an estimation of the maximum possible error, with the higher values less meaningful. Examining the scatter plots shows that this estimation will give the maximum possible error as the true error could be much lower. Comparing this then with the values listed in Table 4.3, standard deviation seems to offer the most useful prediction of best fit error for all values. Using this we can estimate a maximum best fit error of 0.15-0.2 for the magnitudes, and 0.3-0.6 radians for the different phase values. Where the best fit height value is large enough to be useful, for

s_{1-1}, s_{10} and k_{00} this remains consistent with the standard deviation estimations with estimated maximum errors of 0.1-0.15 for the magnitudes and 0.5 radians for the phase value.

4.2.3. Frequency Filtered Data

With the mixed results we can draw from the simulated data above, the fact is that there is a large spread in possible scattering matrix parameters, that when used to simulate a signal, will be within the experimental error of our measurements, i.e., at least two-thirds of the points in the calculation lie within the error bars. In order to combat this, we have attempted to apply frequency filtering to our experimental data to reduce the contribution the noise makes to the signal as the following section will outline and discuss.

Before filtering the data, we must determine the frequencies that we would not expect to arise in the signal. This has been achieved by simulating signals for numerous different random scattering matrices, before applying a Fourier transform as outlined in section 4.1. Figure 4.24a displays the average Fourier spectrum for 10000 such random matrices, whilst 4.23b shows 10 individual spectrums overlayed. As can be seen in these figures there can be peaks at ~1000Hz/gauss, ~2500Hz/gauss and ~5000Hz/gauss, with some smaller peaks past this, where the significance of these frequencies will be discussed below. The picture becomes clearer when comparing the average Fourier spectrum of our random matrices to the Fourier spectrum of our measurement along with the spectrum for our best fit signal, as seen in Figure 4.25. From this we can see that we expect frequencies after 5000Hz/gauss to fall below the noise, so most of the contributions to the spectrum would be expected to be noise rather than from scattered signal. The frequencies between the two peaks also appear to fall below our experimental noise level, however they are much closer, and an individual frequency could rise above this. Following this, two frequency filters have been applied to the measurement and will be investigated, the first is a low pass frequency filter, allowing frequencies below 5500Hz/gauss and the second combines this low pass filter with the removal of the frequencies between 3000 and 4000Hz/gauss, from here on referred to as "window" filtering.

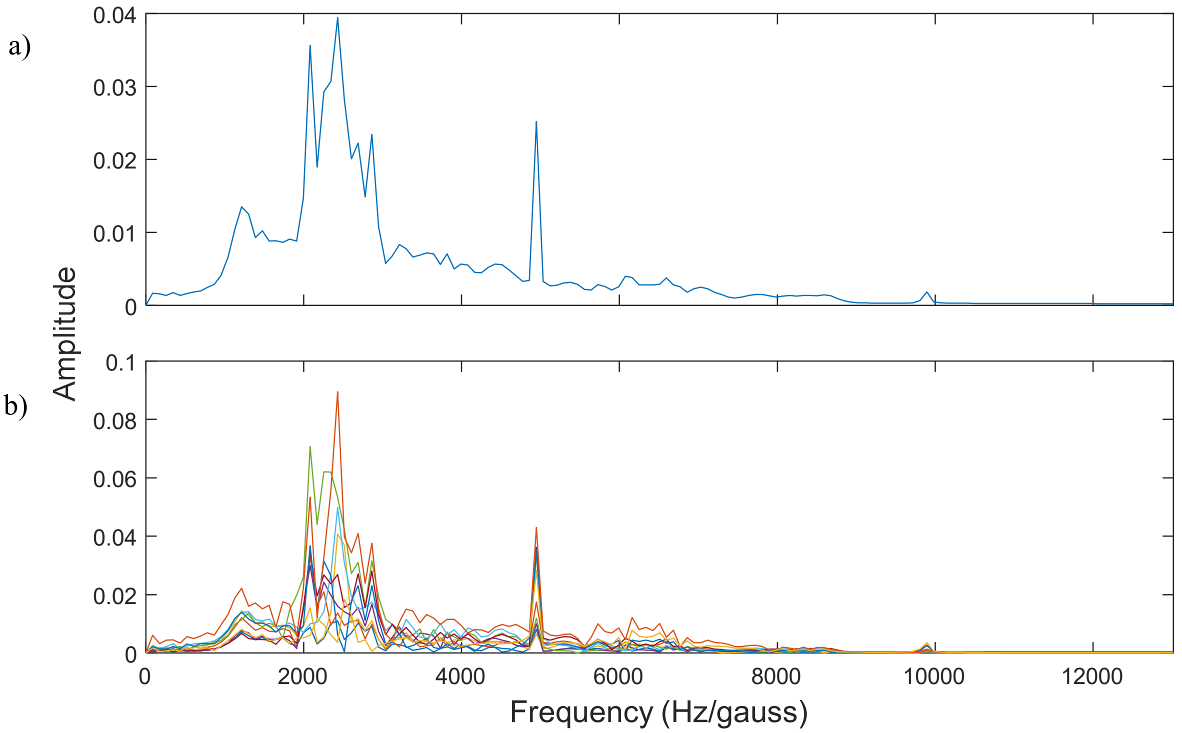

Figure 4.24: a) mean Fourier spectrum of 10000 simulated signals generated with random scattering matrices b) 10 random individual Fourier spectrums picked from those used to generate the mean spectrum.

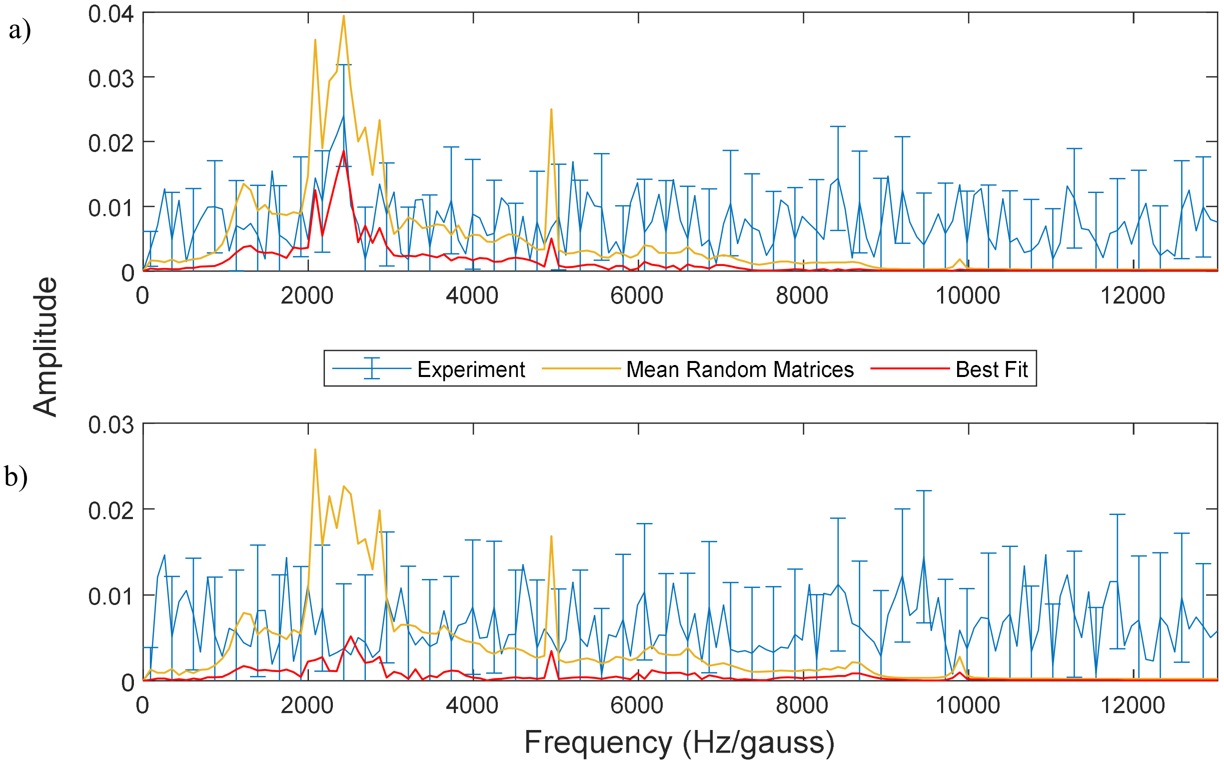

Figure 4.25: Comparison of mean Fourier spectrum of 10000 simulated signals generated with random scattering matrices, yellow, and the Fourier spectrums of the experimental measurements, blue, and the best fit to measurements, red, for a) $I_{B2} = 0A$ *b)* $I_{B2} = 0.5A$

Looking at Figure 4.25b, we observe much more clearly a significant result here that was observed when looking at the B1 scans in previous figures: that there are no significant frequencies observed above the noise level, and as such the best fitting results will give ones that oscillate with I_{B2}=0A but far less with I_{B2}=0.5A.

An interesting point to note here, when referring to Figure 4.2, is that the peak at 5000Hz/gauss exists in the simulated signals for all of our signals calculated using an identity matrix on specular and for all of the signals calculated using random matrices in the diffraction channel to varying degrees. However, these peaks are not seen in the experimental measurements on specular or the diffraction channel. In the latter case this could be due to noise in the frequencies surrounding the peak, however this is less likely in the case of the specular measurement, and current on-going work suggests this is due to the hexapole probabilities used in the simulation. The significance of this value becomes apparent when looking at the values for the terms in the Ramsey Hamiltonian displayed in Table 2.1, as the value of $a + b$ =4930Hz/gauss, compares well to the peaks in the Fourier transforms of the simulated signals of 4935 and 4947Hz/gauss for specular and the diffraction channel respectively. This value therefore corresponds to a transition involving a change in m_I and m_J, which occurs when the hydrogen molecules propagate through the solenoid. The difference in value between the simulated signals arises due to the different mean velocities and the discrete nature of the Fourier transform.

The implementation of these different frequency filters was achieved by first applying the Fourier transform previously described, before removing the contribution of the frequencies to the spectrum as specified by the desired filtering. Then an inverse Fourier transform was applied to the resulting spectrum to give our smoothed signal. Both smoothed signals and Fourier spectrums for the I_{B2} = 0A measurement can be seen in Figure 4.26. As can be seen in the right-hand column, the frequency filtering has not drastically altered the measurement signals. To fit to the smoothed signals and find fits that meet the error threshold, this also requires an adjustment of the errors as calculated previously. To calculate the new errors, the filtering was applied to each individual scan, then the error was calculated as in equation 4.1 as was done for the unfiltered data.

The fit results that met the error threshold for both filtering methods, as well as the unfiltered data for comparison can be seen in Figure 4.27. The first encouraging signs from these figures are the overlap of all three sets histograms. Although, the peaks in the data are slightly different they are located in similar positions, especially for the magnitudes. This is useful in two ways, first it suggests that either of the frequency filtering methods have not removed any important information from the experimental signal, and the second is that it supports the previous results from the unfiltered data and the conclusions we drew from them. Another thing of note, when looking at the comparison of the histograms for s_{10} (middle column, top row) and s_{1-1} (right column, top row) for both filtering methods, the size of bar for the lowest value bin decreased, which could suggest that these fitting values arise due to quicker oscillating noise terms. However, the bars of the smallest value bins for s_{00} (middle column, middle row) and s_{01} (left column, middle row) increase slightly in comparison.

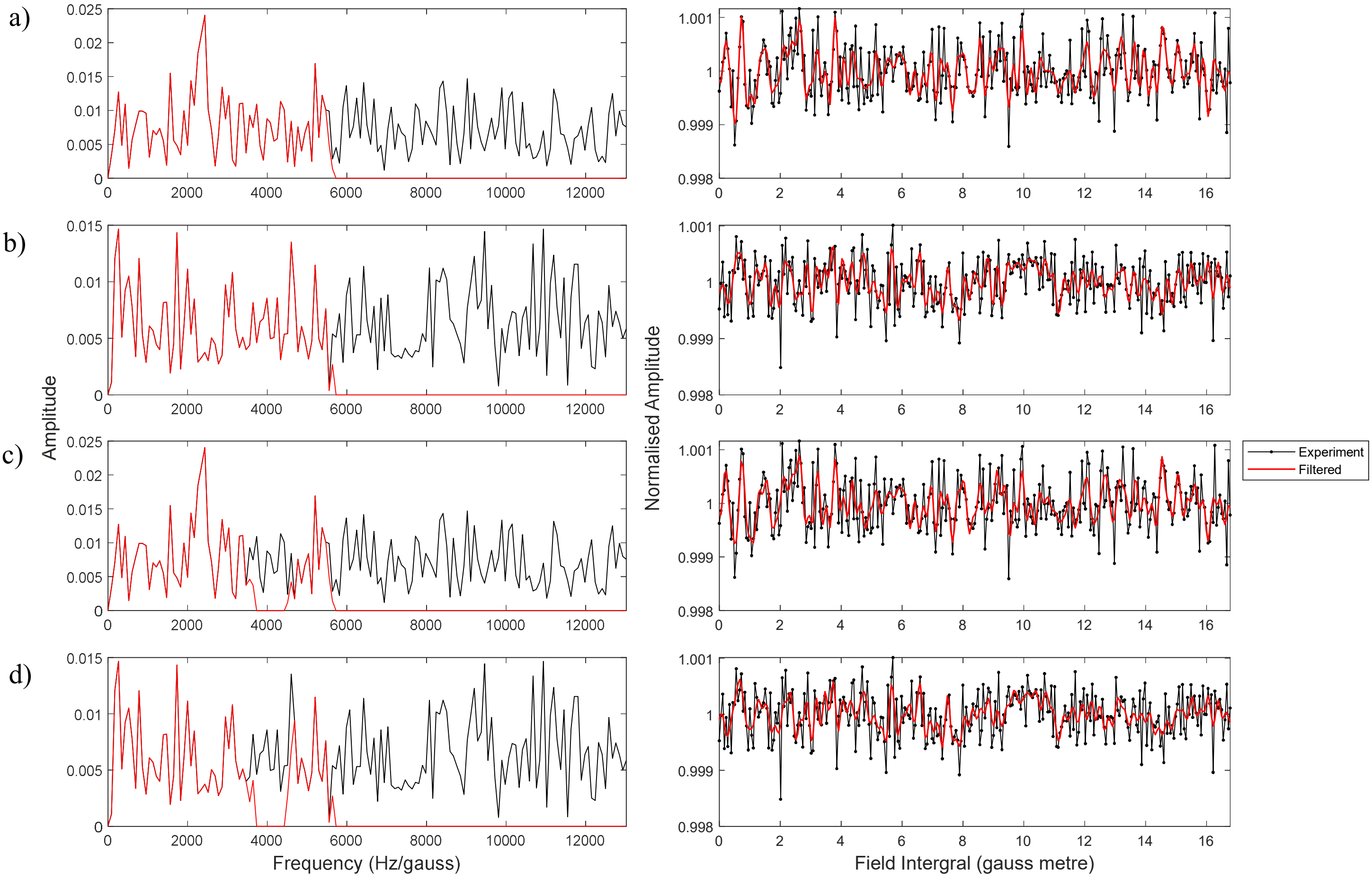

Figure 4.26: Comparison of the Fourier spectrums and signals for the different filtering methods described, in red, to the experimental spectrums and signals, in black. Each panel contains a left plot showing the comparison the Fourier spectrums, and a right plot, comparing the current scan signal. Panel a) shows the low pass 5500Hz/gauss filtering for the $I_{B2} = 0A$ *measurement, panel b) shows the low pass 5500Hz/gauss filtering for the* $I_{B2} = 0.5A$ *measurement, panel c) shows the window filtering for the* $I_{B2} = 0A$ *measurement, panel d) shows the window filtering for the* $I_{B2} = 0.5A$ *measurement*

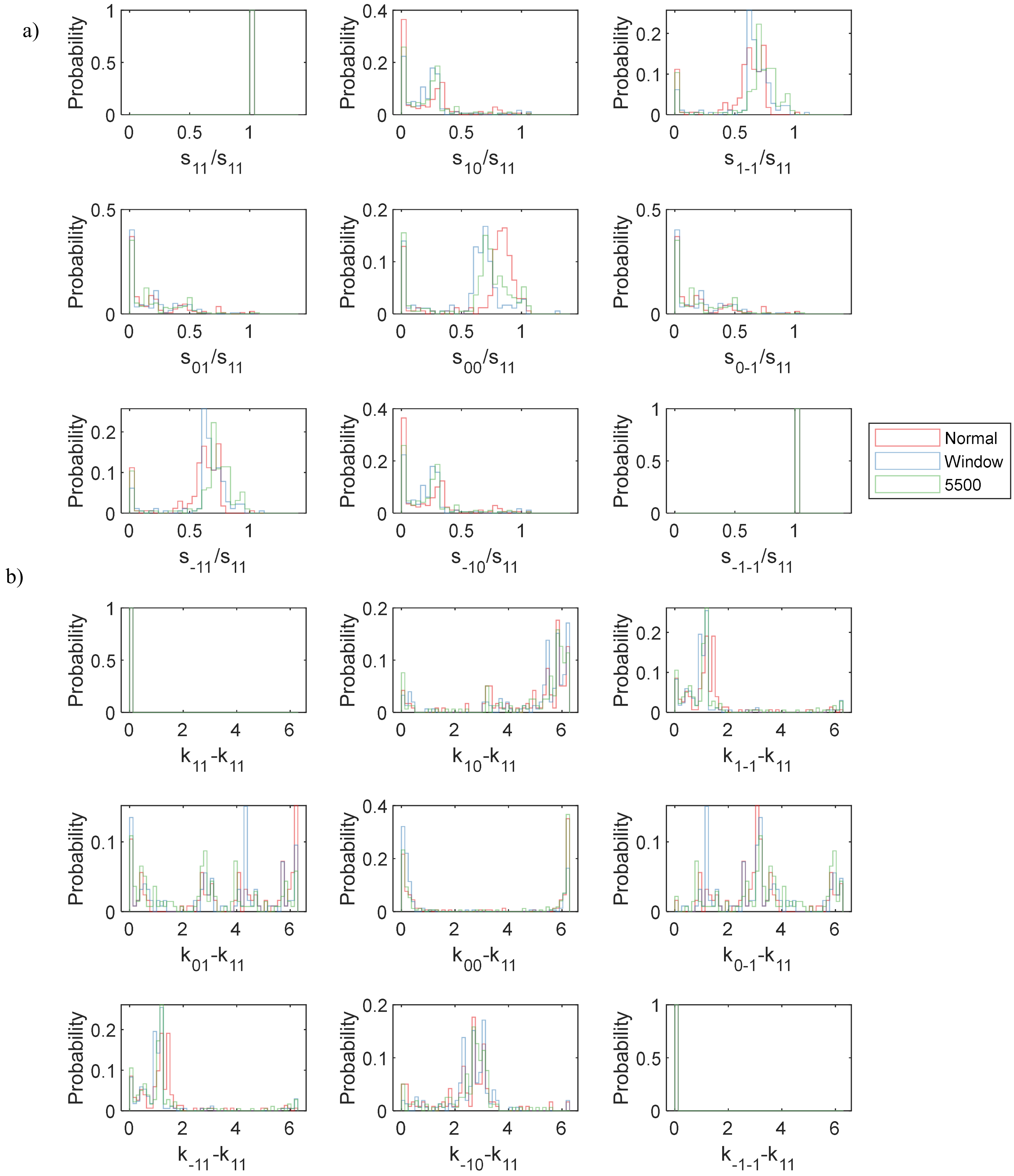

Figure 4.27: Histograms for the different scattering matrix parameters for the fit results that meet the error threshold for the three different filtering schemes, unfiltered, red, window, blue, and low pass 5500Hz/gauss, green. Panel a) contains the histogram for the magnitude values, and Panel b) those for the phases.

The similarity of the histograms is also encouraging in that it suggests the conclusions we made about the relative probabilities of a given rotational projection state scattering into the (0,1) channel and the polarising properties of the surface should hold regardless of our data treatment in terms of filtering. We can investigate if these hold between our different data treatments when looking at Figure 4.28. Here the relative probabilities of cartwheel to helicopter states before (top row) and after (bottom row) scattering for each fit result are plotted against the total error of the fit for the different filtering methods used. Examining the top row of scatter plots, representing the probabilities before scattering, it can be seen that almost all agree that fewer cartwheels scatter into the diffraction channels than helicopters, especially for the lower error results. Similarly for the bottom row, most show that the surface increases the proportion of helicopters in the beam leaving the surface.

Table 4.4 compares the different best fit result values for the different data treatment methods, focussing on the four unique values of each magnitude and phase we can obtain. As in the comparison of the histograms and the ratios of cartwheels and helicopters, encouragingly the results are quite similar again. They definitely lie within the error we have previously estimated for the unfiltered data best fits. Moreover, they also both support the general conclusions we previously made about scattering in that both helicopters and cartwheels prefer to remain in their original m_J states, and if helicopters do change state, they are much more likely to remain a helicopter state – just with a reversed direction of rotation – although it is difficult to provide a simple physical picture of why this is the case. Interestingly, the best fit phases also came out very similarly regardless of the filtering performed. Although the histograms shown do not offer significant improvement on the unfiltered data and so may not offer improved benchmarking, it is very encouraging that they support our previous conclusions we have made using the unfiltered data.

	s_{10}/s_{11}	s_{1-1}/s_{11}	s_{01}/s_{11}	s_{00}/s_{11}	$k_{10}-k_{11}$	$k_{1-1}-k_{11}$	$k_{01}-k_{11}$	$k_{00}-k_{11}$
Unfiltered	0.300	0.589	0.169	0.844	5.482	1.481	4.384	0.058
Low Pass	0.267	0.690	0.152	0.753	5.622	1.237	3.902	0.071
Window	0.253	0.626	0.202	0.716	5.423	1.209	4.339	0.211

Table 4.4: Best fit scattering matrix values, magnitudes and phases, when fitting to the unfiltered and the two different filtered experimental measurements. Here values that are normalised to or are just mirrors or phase shifted values as defined by equations 2.36-2.43 are not shown.

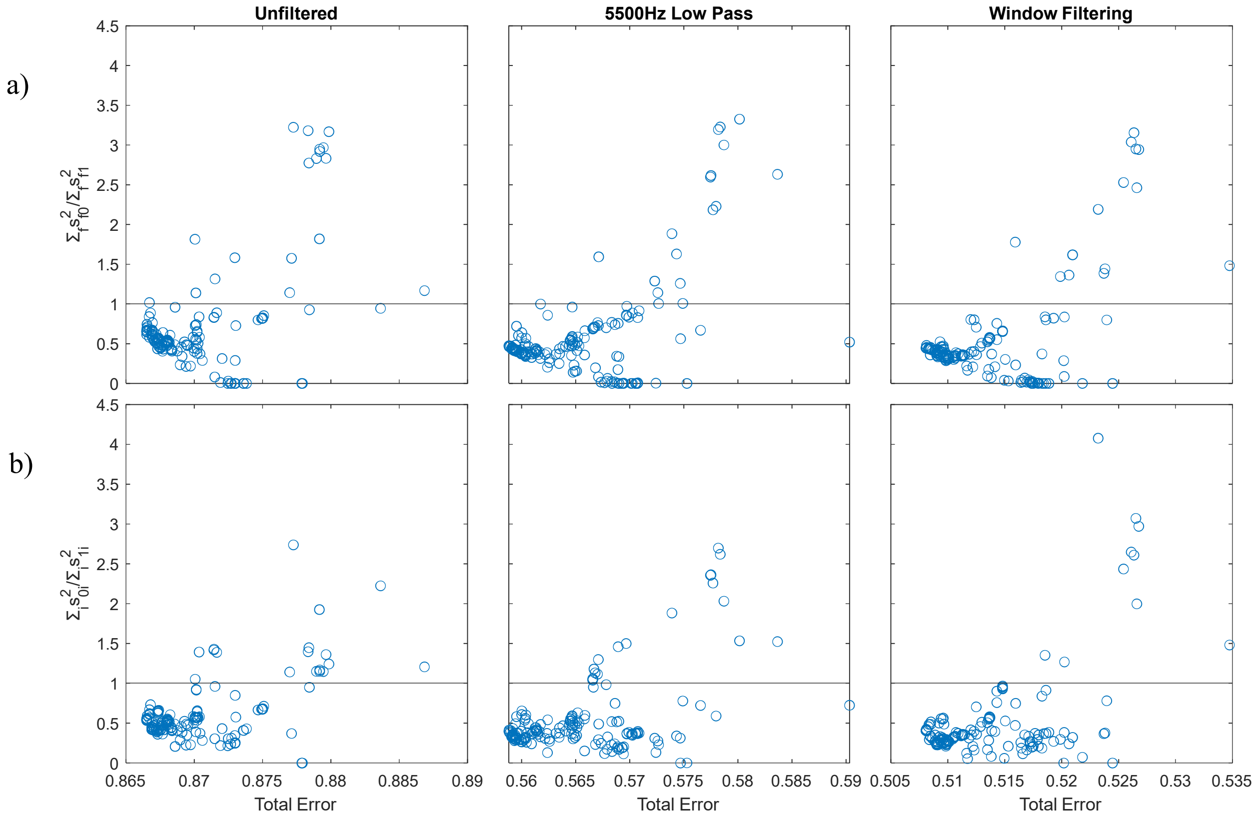

Figure 4.28: Scatter plots comparing the ratio of the populations of $m_J = 0$ vs $m_J = 1$ given by the fit results when fitting to the experimental measurements after applying the no filter (left column), a 5500Hz/gauss low pass filter (middle column) and window filtering (right column). The top row gives the ratio of the different states before the collision, whilst the bottom row of scatter plots is the ration after the collision.

4.2.4. Significance of Zero Magnitude Results

Looking at Figures 4.19 and 4.20, we can see that when fitting with the level of noise we have seen experimentally, often the fit results for the scattering matrix magnitudes will give very small values some portion of the time even when the actual value is quite large. We can also test if the reverse is true, when fitting to signals generated using scattering matrices containing a zero magnitude, would we observe a small peak in the histogram of the fit results for that magnitude value away from zero. In order to test this, one of the fit results to our experimental data with a s_{01} value very close to zero was used to simulate two experimental signals before adding noise, using the same process as described in section 4.1.1. Finally, these signals were fit 100 times, with this process repeated four separate times to ensure any results were not simple outliers. The histograms for the scattering matrix magnitudes for the fits to one of these simulated signals can be seen in Figure 4.29. When looking at the histogram of s_{01} we can see that there is a small secondary peak away from zero despite the true value being essentially zero, on the order of 10^{-7}, a fact that was seen in the other repeats of this test. However encouragingly the best fit is till close to the original magnitude, and the values of the secondary peak were never observed to be above 0.4, suggesting perhaps that the peaks at zero are less significant when the main peak is further from zero.

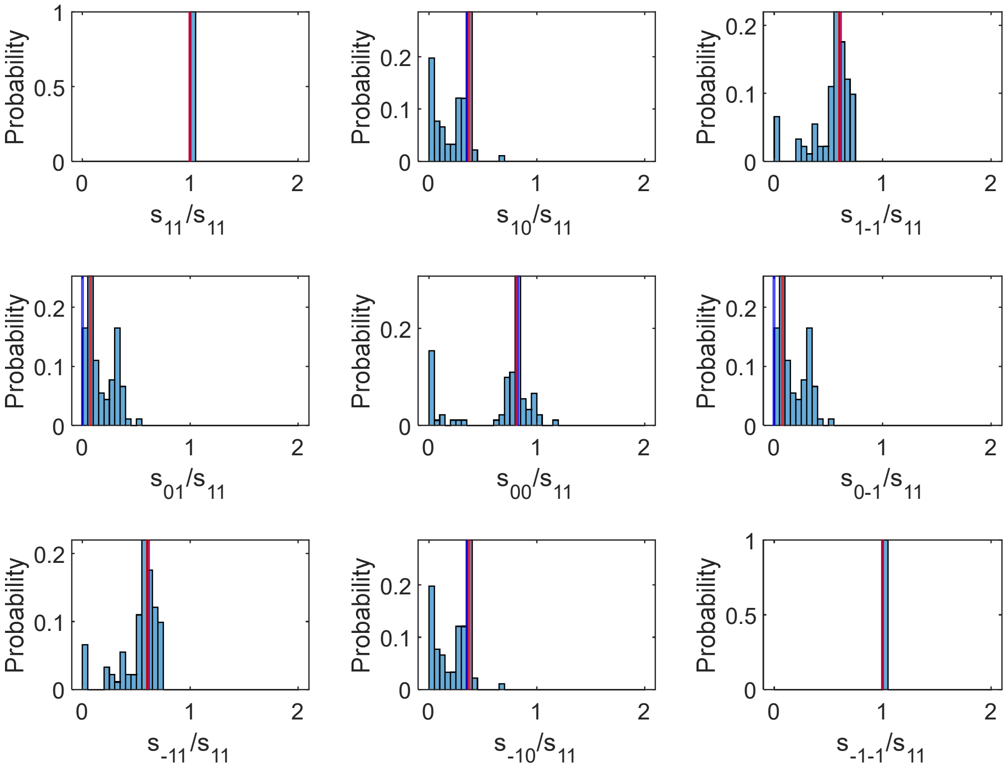

Figure 4.29: Histograms of one of the magnitudes for fitting two simulated signals using a scattering matrix with a value of s_{01} close to zero and with 17.5% noise added. The values of the best fit and original value used to simulate the signals are marked by blue and red lines respectively.

The reason why the fitting algorithm is zeroing magnitudes on different fits can be explored by looking at Figure 4.30. Displayed in these plots are five simulated B1 scans using five different scattering matrix results from the fits to the experimental data, one uses the best fit to the data and each of the remaining four were selected as they contain a different scattering matrix magnitude which is almost zero, with the element with the small magnitude given in the legend in the plot between panels a and b. When examining the scan for I_{B2}=0A, the differences are very small and well with our experimental error, and as such a very high signal to noise ratio would be needed to differentiate between them. In comparison, while the oscillation amplitude is much smaller for the scan for I_{B2}=0.5A, the differences between the various signals are relatively more pronounced. While the differences are larger these still fall within the experimental error in our measurements and as such demonstrates how the fitting code would be able to give any of these results. This also demonstrates the importance of a second measurement for fitting purposes. While the first simulated signals are very similar despite their different scattering matrices, the second signals show larger differences and the signal-to-noise ratio required to differentiate between the signals produced by the different scattering matrices is less than for the first due to the difference in phase observed.

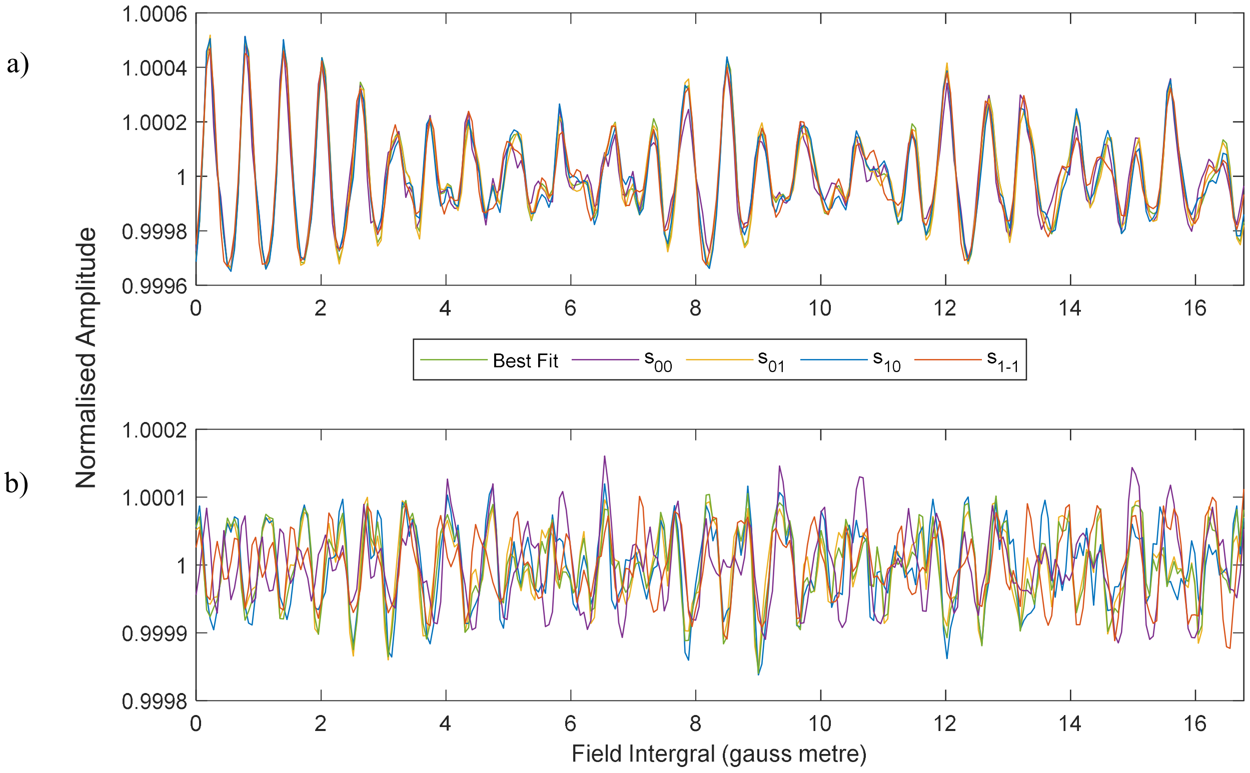

Figure 4.30: Comparison of simulated signals generated using four different fit results where the magnitudes are ~0 for different matrix elements as well as simulated signals using the best fir result. Panel a) gives the simulated signals with 0A in the second solenoid and panel b) is for 0.5A in the second solenoid.

5. Summary and Outlook

5.1. Specular Measurement

The first measurement produced and analysed was the scattering of hydrogen at specular from our hydrogen passivated chromium (110) surface whilst the nuclear spin projection state, m_I, and rotational projection state, m_J, were coherently controlled as outlined in section 2.2.3. Our measurement while scanning current through the first solenoid was compared with a simulated scan for the same measurement with an identity scattering matrix. The comparison showed that the identity matrix simulation fits well with our measurement within experimental error. This allowed us to conclude that at specular the scattering matrix closely resembles an identity matrix and there is no significant preference for scattering in terms of helicopters or cartwheels, which is non-trivial as there is not simple physical picture for such a system. Moreover this means that no changes in nuclear spin projection state were observed, despite the antiferromagnetic properties of chromium[57], or in other words, the nuclear spin projection state of hydrogen acts as a spectator when scattering from our surface, and so we can reduce our 9-by-9 scattering matrix in the $|m_I, m_J\rangle$ space to a 3-by-3 scattering matrix in the $|m_J\rangle$ subspace. Since we have only performed measurements for one value of B2 we couldn't try to extract a scattering matrix from fitting the data. However, to check if this is possible in future measurements we simulated a second signal at a different second solenoid field strength, using an identity scattering matrix. Adding noise to this signal comparable to the experimental noise and combining this with our measurement at I_{B2} = 0A, we are able to fit both signals and the result gives an identity scattering matrix. This demonstrates such fits are possible despite the quicker decay in oscillation of the signal at specular.

5.2. Diffraction Channel Measurements

Solenoid 1 current scans were performed at two different solenoid 2 current values when scattering hydrogen into the (0,1) diffraction channel. Using both of these measurements we are able to provide a benchmark for theoretical scattering matrices by simulating both signals using those predicted matrices and seeing how well it agrees with the measured data within our experimental error. We showed that an identity scattering matrix fit the at I_{B2} = 0A scan quite well but not the noisier at I_{B2} = 0.5A scan, whereas there was no correlation with either measurement when comparing to signals calculated using a randomly selected scattering matrix. We then applied a fitting algorithm to these experimental signals to try and determine our scattering matrix magnitudes and phases directly from our experimental data. The results did not all converge on a single value, often producing more than one peak, including magnitude peaks close to zero. Most of the fit results agree with our measured data within experimental error and so could be considered a possible result for the scattering matrix, including an identity matrix result. However, some have a smaller error in comparison to the measurements than others.

Taking our results as a whole, i.e., examining the histograms of the matrix element values from the various fits, we were still able to make observations about the scattering. In particular, comparing the ratio of m_J=0 to $m_J = 1$ before the collision, indicates to us that more $m_J = \pm 1$ state hydrogen molecules scattered into the diffraction channel than those in $m_J = 0$. Moreover, comparing this ratio after the collision shows that more $m_J = \pm 1$ states are scattered from the surface than $m_J = 0$ states – demonstrating the polarising capabilities of our surface when scattering from the (0,1) diffraction channel. When looking at all the fits we can also see that molecules in any m_J states before the collision are more likely to remain in their m_J state after the collision than change, with molecules approaching in $m_J = \pm 1$ more likely to reverse their rotation direction than change to $m_J = 0$, after scattering from the surface. However, the rotational projection state changing off-diagonal elements do make a significant contribution to the measured signal.

The particular set of matrix elements which produced the best fit to our data agrees with the general trends mentioned above. As it is a single set of numbers, it could potentially provide a useful benchmark for theoreticians when calculating the scattering matrix, however for this we would need to assess its significance. To see how reliably we are able to retrieve an accurate scattering matrix with our best fit result, and thus assess its importance, multiple noisy signals were generated by simulating a signal from the matrix obtained by the best fit, adding noise to pairs of signals four different times and then applying the fitting algorithm. The results observed showed similarities to what has been seen experimentally with a spread of fit values and a number of magnitude fit values in "zero" value bins. However, despite this, the best fit matrix elements were close to the original values used to generate the signal.

To further quantify the relation between the best fit results and the actual scattering matrix values in a way which is not unique to the particular scattering matrix which best fits the experimental data, this process of simulating two signals, adding noise, and fitting to them was repeated for five different scattering matrices at different levels of noise, four times for each noise. This analysis allowed us to relate statistical properties of the distribution of the results (best fit height and standard deviation of the fit results) to the error between the best fit and the actual matrix elements. Applying these relations to the results obtained from fitting the data (Table 4.3) suggests that for the different magnitudes we expect a maximum error between the best fit value and scattering matrix value between 0.1-0.2 depending on the standard deviation of the value obtained from the fits, and the best fit height if this is large enough to reliably estimate an error. For the phases we then expect maximum best fit errors of 0.3-0.6 radians.

In an attempt to make our results more reliable different frequencies were filtered out of the experimental signals. This was performed using two schemes, the first a low pass filter below 5500Hz/gauss, as frequencies above this were not expected to contribute to the signal and fall below the noise level. The second scheme used the same low pass filter, but contained a second band that was filtered out between 3500 to 4500Hz/gauss, as the contribution these frequencies make were also expected to fall below the noise level. Under both filtering schemes our earlier conclusions about the preferential scattering of helicopter states into the diffraction channel and the polarisation of the hydrogen beam after scattering held. Moreover, the trends in the final state after scattering for both cartwheels and helicopters appeared to stay the same.

Finally, with the reduction in the number of zero bin fit for s_{1-1} when filtering, the distance between the zero bin and the best fit value in combination with the estimated error for s_{00} and s_{1-1}, and the fact that we observe these results when providing a non-zero scattering matrix value when fitting simulated data suggests that these could just be an artefact of the fitting algorithm and could be ignored. However, when removing the fits with very small s_{1-1} and s_{00} values the distributions of the other variables do not change significantly. Moreover, when comparing signals with the different scattering matrix parameters set to zero, we can see how similar they are for the I_{B2} = 0A case. Whilst they are more significantly different for signals calculated at I_{B2} = 0.5A, due to the noise of the measured data the calculated signals all lie within the experimental error and therefore it is difficult to exclude any such results as they are still valid solutions for the scattering matrix.

Overall, our diffraction measurements are able to provide us with a benchmarking ability for theoreticians to use, information about the stereodynamic properties of the scattering event, information on the preference of different rotational projection states in scattering and likely preferences of different rotational states scattering into other states. We also have a set of scattering matrix values from the best fit to the data and have some indication to our confidence in this result, however there are a range of scattering matrices that would meet the experimental error, so providing values for benchmarking is not possible with our current results.

5.3. Outlook

With regards to the specular measurements and conclusions drawn from these, future experiments could explore other magnetic surfaces with different magnetic ordering that could be of interest. Part of this could be testing if the conclusions found in this thesis regarding there being no change in nuclear spin projection state of the hydrogen upon scattering are the same for other surfaces. Materials such as ferromagnetic nickel or ferrimagnetic yttrium iron garnet could be utilised.

As explained in the chapters preceding this, the results obtained in our diffraction channel measurements can be used as a test for any models of the scattering of molecular hydrogen from hydrogen covered chromium. Therefore, a future avenue would be to test current models and approximations and investigate how the results of calculations compare to what is found here experimentally. Moreover, if using a density functional theory calculated potential energy surface, different functionals could be utilised and the performance of various functionals could be compared, as has been performed using hydrogen diffraction measurements for various surfaces[30].

Expanding on the work in this thesis using the same system could also provide useful information. A second solenoid 1 current scan could be performed for specular scattering at a different second solenoid current. The use of this would be two-fold, firstly to test if the expectation of being able to fit a scattering matrix to an identity specular scattering matrix is possible and thus secondly to test if the simulation used in this work was a reliable model. Further measurements on hydrogen scattering from H-Cr(110) could also involve a different diffraction channel, for example in the $(0, -1)$ channel. In [8] when comparing the scattering matrices found for the (1,0) and $(-1,0)$ diffraction channels when scattering from LiF(100), the preferences in scattering into one of the channels when approaching the surface as a helicopter or a cartwheel were opposite for the two channels. Finally, the hydrogen could be scattered with higher incident energies by adjusting the nozzle temperature, to provide a more complete image of the interaction which will help theoreticians benchmark their calculations, similar to hydrogen diffraction studies performed using different surfaces[24].

References

1. Zheng, F., et al., *Research Progress on Heterogeneous Reactions of Pollutant Gases on the Surface of Atmospheric Mineral Particulate Matter in China.* Atmosphere, 2022. 13(8).
2. Somorjai, G.A. and Y. Li, *Impact of surface chemistry.* Proceedings of the National Academy of Sciences, 2011. 108(3): p. 917-924.
3. Kroes, G.-J. and C. Díaz, *Quantum and classical dynamics of reactive scattering of H2 from metal surfaces.* Chemical Society Reviews, 2016. 45(13): p. 3658-3700.
4. Jiang, B., et al., *Quantum dynamics of polyatomic dissociative chemisorption on transition metal surfaces: mode specificity and bond selectivity.* Chemical Society Reviews, 2016. 45(13): p. 3621-3640.
5. Guo, H., A. Farjamnia, and B. Jackson, *Effects of Lattice Motion on Dissociative Chemisorption: Toward a Rigorous Comparison of Theory with Molecular Beam Experiments.* The Journal of Physical Chemistry Letters, 2016. 7(22): p. 4576-4584.
6. Papoian, G., J.K. Nørskov, and R. Hoffmann, *A Comparative Theoretical Study of the Hydrogen, Methyl, and Ethyl Chemisorption on the Pt(111) Surface.* Journal of the American Chemical Society, 2000. 122(17): p. 4129-4144.
7. Park, G.B., et al., *Fundamental mechanisms for molecular energy conversion and chemical reactions at surfaces.* Reports on Progress in Physics, 2019. 82(9): p. 096401.
8. Alkoby, Y., et al., *Setting benchmarks for modelling gas–surface interactions using coherent control of rotational orientation states.* Nature Communications, 2020. 11(1): p. 3110.
9. Greg, O.S., *Gas surface interactions studied with state-prepared molecules.* Reports on Progress in Physics, 2002. 65(8): p. 1165.
10. Yoder, B.L., R. Bisson, and R.D. Beck, *Steric Effects in the Chemisorption of Vibrationally Excited Methane on Ni(100).* Science, 2010. 329(5991): p. 553-556.
11. Schäfer, T., et al., *Orienting polar molecules without hexapoles: Optical state selection with adiabatic orientation.* Chemical Physics Letters, 2012. 535: p. 1-11.
12. Bartels, N., et al., *Observation of orientation-dependent electron transfer in molecule–surface collisions.* Proceedings of the National Academy of Sciences, 2013. 110(44): p. 17738-17743.
13. Kurahashi, M. and Y. Yamauchi, *Spin Correlation in O2 Chemisorption on Ni(111).* Physical Review Letters, 2015. 114(1): p. 016101.
14. Kurahashi, M., *Oxygen adsorption on surfaces studied by a spin- and alignment-controlled O2 beam.* Progress in Surface Science, 2016. 91(1): p. 29-55.
15. Kurahashi, M. and T. Kondo, *Alignment-resolved*

O2 scattering from highly oriented pyrolytic graphite and LiF(001) surfaces. Physical Review B, 2019. 99(4): p. 045439.

16. Chadwick, H. and R.D. Beck, *Quantum State–Resolved Studies of Chemisorption Reactions.* Annual Review of Physical Chemistry, 2017. **68**(1): p. 39-61.
17. Hou, H., et al., *The Stereodynamics of a Gas-Surface Reaction.* Science, 1997. **277**(5322): p. 80-82.
18. Rutkowski, M., D. Wetzig, and H. Zacharias, *Mechanism of the Poisoning Action Of Sulfur on Catalytically Active Pd(100).* Physical Review Letters, 2001. **87**(24): p. 246101.
19. Wetzig, D., et al., *Rotational Alignment in Associative Desorption of D2 (v''=0 and 1) from Pd(100).* Physical Review Letters, 1996. **76**(3): p. 463-466.
20. Hodgson, A., *State resolved desorption measurements as a probe of surface reactions.* Progress in Surface Science, 2000. **63**(1): p. 1-61.
21. Chadwick, H., et al., *Molecular spin echoes; multiple magnetic coherences in molecule surface scattering experiments.* Physical Chemistry Chemical Physics, 2021. **23**(13): p. 7673-7681.
22. Chadwick, H., et al., *Stopping molecular rotation using coherent ultra-low-energy magnetic manipulations.* Nature Communications, 2022. **13**(1): p. 2287.
23. Bertino, M.F. and D. Farías, *Probing gas-surface potential energy surfaces with diffraction of hydrogen molecules.* Journal of Physics: Condensed Matter, 2002. **14**(24): p. 6037.
24. Farías, D. and R. Miranda, *Diffraction of molecular hydrogen from metal surfaces.* Progress in Surface Science, 2011. **86**(9): p. 222-254.
25. Gross, A. and M. Scheffler, *Scattering of hydrogen molecules from a reactive surface: Strong off-specular and rotationally inelastic diffraction.* Chemical Physics Letters, 1996. **263**(3): p. 567-573.
26. Pijper, E., et al., *Dissociative and diffractive scattering of H2 from Pt(111): A four-dimensional quantum dynamics study.* The Journal of Chemical Physics, 2002. **116**(21): p. 9435-9448.
27. Pijper, E., et al., *Reactive and diffractive scattering of H2 from Pt(111) studied using a six-dimensional wave packet method.* The Journal of Chemical Physics, 2002. **117**(12): p. 5885-5898.
28. Farías, D., et al., *In-plane and out-of-plane diffraction of H(2) from metal surfaces.* Phys Rev Lett, 2004. **93**(24): p. 246104.
29. Farías, D., H.F. Busnengo, and F. Martín, *Probing reaction dynamics at metal surfaces with H2 diffraction.* Journal of Physics: Condensed Matter, 2007. **19**(30): p. 305003.
30. Nieto, P., et al., *Diffractive and reactive scattering of H2 from Ru(0001): experimental and theoretical study.* Phys Chem Chem Phys, 2011. **13**(18): p. 8583-97.
31. Ubaid, S., et al., *Effect of para–ortho conversion on hydrogen storage system performance.* International Journal of Hydrogen Energy, 2014. **39**(22): p. 11651-11660.

32. Larsen, A.H., F.E. Simon, and C.A. Swenson, *The Rate of Evaporation of Liquid Hydrogen Due to the Ortho-Para Hydrogen Conversion.* Review of Scientific Instruments, 1948. **19**(4): p. 266-269.
33. Fukutani, K. and T. Sugimoto, *Physisorption and ortho–para conversion of molecular hydrogen on solid surfaces.* Progress in Surface Science, 2013. **88**(4): p. 279-348.
34. Andersson, S. and J. Harris, *Observation of Rotational Transitions for H2, D2, and HD Adsorbed on Cu(100).* Physical Review Letters, 1982. **48**(8): p. 545-548.
35. Svensson, K. and S. Andersson, *Fast Ortho-Para Conversion of ${\mathrm{H}}_{2}$ Adsorbed at Copper Surface Step Atoms.* Physical Review Letters, 2007. **98**(9): p. 096105.
36. Avouris, P., D. Schmeisser, and J.E. Demuth, *Observation of rotational excitations of H2 adsorbed on Ag surfaces.* Physical Review Letters, 1982. **48**(3): p. 199-202.
37. Fukutani, K., et al., *Photostimulated desorption and ortho-para conversion of H2 on Ag surfaces.* Physical Review Letters, 2003. **90**(9): p. 096103/1-096103/4.
38. Fukutani, K., et al. *Photodesorption of hydrogen molecules physisorbed on Ag: Isotope dependence of translational-energy distribution*. in *Surface Science*. 2005.
39. Niki, K., et al., *Mechanism of the ortho-para conversion of hydrogen on Ag surfaces.* Physical Review B, 2008. **77**(20): p. 201404.
40. Kasai, H., W.A. Diño, and R. Muhida, *Surface science-based reaction design: increasing the ortho–para hydrogen conversion yield via molecular orientation, a case study.* Progress in Surface Science, 2003. **72**(1): p. 53-86.
41. Rutkowski, M. and H. Zacharias, *Depolarisation of the spatial alignment of the rotational angular momentum vector by hyperfine interaction.* Chemical Physics, 2004. **301**(2): p. 189-196.
42. Bartlett, N.C.M., et al., *Time-dependent depolarization of aligned HD molecules.* Physical Chemistry Chemical Physics, 2009. **11**(1): p. 142-147.
43. Godsi, O., et al., *A general method for controlling and resolving rotational orientation of molecules in molecule-surface collisions.* Nature Communications, 2017. **8**(1): p. 15357.
44. Jardine, A.P., et al., *Ultrahigh-Resolution Spin-Echo Measurement of Surface Potential Energy Landscapes.* Science, 2004. **304**(5678): p. 1790-1793.
45. Bergin, M., et al., *Low-energy electron ionization mass spectrometer for efficient detection of low mass species.* Review of Scientific Instruments, 2021. **92**(7): p. 073305.
46. Alkoby, Y., *Studying molecule-surface interactions using magnetically manipulated molecular beams*, in *Chemistry*. 2022, Swansea University.
47. Jardine, A.P., et al., *Hexapole magnet system for thermal energy 3He atom manipulation.* Review of Scientific Instruments, 2001. **72**(10): p. 3834-3841.
48. Ramsey, N.F., *Theory of Molecular Hydrogen and Deuterium in Magnetic Fields.* Physical Review, 1952. **85**(1): p. 60-65.

49. Krüger, C., et al., *A magnetically focused molecular beam source for deposition of spin-polarised molecular surface layers.* The Journal of Chemical Physics, 2018. **149**(16): p. 164201.
50. Cheng, Y.-C.N. and E.M. Haacke, *Magnetic Moment of a Spin, Its Equation of Motion, and Precession.* Current Protocols in Magnetic Resonance Imaging, 2007. **14**(1): p. B1.1.1-B1.1.10.
51. Cantin, J.T., G. Alexandrowicz, and R.V. Krems, *Transfer-matrix theory of surface spin-echo experiments with molecules.* Physical Review A, 2020. **101**(6): p. 062703.
52. Mowrey, R.C. and G.J. Kroes, *Application of an efficient asymptotic analysis method to molecule–surface scattering.* The Journal of Chemical Physics, 1995. **103**(3): p. 1216-1225.
53. Nelder, J.A. and R. Mead, *A Simplex Method for Function Minimization.* The Computer Journal, 1965. **7**(4): p. 308-313.
54. Ashcroft, N.W. and N.D. Mermin, *Solid state physics*. 1977, New York ;: Holt, Rinehart and Winston.
55. Lucas, C.A., *Surface Structure Determination by Interference Techniques*, in *Surface Analysis – The Principal Techniques*. 2009. p. 391-478.
56. Woodruff, D.P. and T.A. Delchar, *Modern Techniques of Surface Science*. 2 ed. Cambridge Solid State Science Series. 1994, Cambridge: Cambridge University Press.
57. Fawcett, E., *Spin-density-wave antiferromagnetism in chromium.* Reviews of Modern Physics, 1988. **60**(1): p. 209-283.
58. Hartmut, Z., *Magnetism of chromium at surfaces, at interfaces and in thin films.* Journal of Physics: Condensed Matter, 1999. **11**(48): p. 9303.
59. Svanidze, E., et al., *An itinerant antiferromagnetic metal without magnetic constituents.* Nature Communications, 2015. **6**(1): p. 7701.
60. Braun, K., et al., *Observation of charge-density wave domains on the Cr(110) surface by low-temperature scanning tunneling microscopy.* Phys Rev Lett, 2000. **85**(16): p. 3500-3.
61. Rotenberg, E., O. Krupin, and S.D. Kevan, *Surface states and spin density wave periodicity in Cr(110) films.* New Journal of Physics, 2008. **10**(2): p. 023003.
62. Krupin, O., E. Rotenberg, and S.D. Kevan, *Controlling the magnetic ground state in Cr1-x Vx films.* Phys Rev Lett, 2007. **99**(14): p. 147208.
63. Foord, J.S. and R.M. Lambert, *A structural and kinetic study of chlorine chemisorption and surface chloride formation on Cr(100).* Surface Science, 1982. **115**(1): p. 141-160.
64. Schmid, M., et al., *Segregation of impurities on Cr(100) studied by AES and STM.* Surface Science, 1997. **377-379**: p. 1023-1027.
65. Lagoute, J., et al., *Spin-polarized scanning tunneling microscopy and spectroscopy study of chromium on a Cr(001) surface.* Journal of Physics: Condensed Matter, 2011. **23**(4): p. 045007.

66. McCash, E.M., *Surface chemistry*. Repr. ed. 2001: Oxford : Oxford university press.
67. Alexandrowicz, G., *Helium Spin Echo Spectroscopy: Measuring the Dynamics of Atoms, Molecules and Surfaces*. 2005, University of Cambridge.
68. Chadwick, H. and G. Alexandrowicz, *Measuring surface phonons using molecular spin-echo.* Physical Chemistry Chemical Physics, 2022. **24**(23): p. 14198-14208.